

Towards a data assimilation system for morphodynamic modeling

Proefschrift

ter verkrijging van de graad van doctor
aan de Technische Universiteit Delft,
op gezag van de Rector Magnificus prof. ir. K.C.A.M. Luyben,
voorzitter van het College voor Promoties,
in het openbaar te verdedigen op Maandag, 12 Mai 2014 om 10.00 uur

door

Iván David Tomás Fernando GARCÍA TRIANA

Master of Sciences in Hydrosystems
Pontificia Universidad Javeriana
geboren te Bogotá, Colombia.

Dit proefschrift is goedgekeurd door de promotor:
Prof. dr. ir. A. W. Heemink

Copromotor:
Dr. ir. H. M. Schuttelaars

Samenstelling promotiecomissie:

Rector Magnificus	voorzitter
Prof. dr. ir. A. W. Heemink,	Technische Universiteit Delft, promotor
Prof. dr. ir. H. X. Lin,	Technische Universiteit Delft
Prof. dr. ir. D. Roelvink,	Technische Universiteit Delft
Prof. dr. G. Ruessink,	Universiteit Utrecht
Prof. dr. ir. M. Stive,	Technische Universiteit Delft
Dr. H. M. Schuttelaars,	Technische Universiteit Delft, copromotor
Dr. ir. G. Y. El Serafy,	Deltares

Dit onderzoek kwam tot stand met steun van Deltares



Dr. ir. Ghada Y. El Serafy heeft als begeleider in belangrijke mate aan de totstandkoming van het proefschrift bijgedragen

Cover: Picture by Esmé van Bokhoven. Published in Water en Spelen. Edited by *Duo/Duo*, Rotterdam, Netherlands. ISBN: 90-72971-60-4.

ISBN/EAN 978-94-6108-669-3

Copyright ©2014 by Iván D. García

All rights reserved. No part of the material protected by this copyright notice may be reproduced or utilized in any form or by any means, electronic or mechanical, including photocopying, recording or by any information storage and retrieval system, without the prior permission of the author.

Typeset by the author with the L^AT_EX Documentation System.
Printed by Gildeprint Drukkerijen - The Netherlands.

To my parents, of course.

Contents

Contents	i
Acknowledgments	iii
Summary	v
Samenvatting	viii
1 Introduction	1
1.1 Problem description	3
1.2 Models, model errors and data assimilation.	4
1.3 Morphodynamic modeling	6
1.4 Data assimilation scheme: Model reduced 4DVar	7
1.5 Implementations	7
1.6 Reading guide	8
2 A review of data assimilation	11
2.1 Optimal interpolation and Kalman filter	12
2.2 Variational methods	14
2.3 Particle filters	16
3 Model reduced 4D-Var: Insight and updates	21
3.1 Model order reduction	22
3.2 Ensemble Model Order Reduction: An alternative method	23
3.3 Model Reduced 4D-Var	28
4 Wave-Flow-Morphodynamic modeling	31
4.1 Swan and Delft3D-MOR Description	32
4.1.1 Waves Module	32
4.1.2 Hydrodynamic Module	32
4.1.3 Morphodynamic Module	34

4.2	Delft3D Parameters	36
4.3	Model Characterization	38
4.3.1	Time Steps and Temporal Evolution of the Model	38
4.3.2	Effects of re-starting Delft3D	41
4.3.3	Sediment and water volumetric changes	44
4.3.4	Linearization: Finite Differences	45
5	Estimation of wave parameters	51
5.1	Study case and numerical model	52
5.2	Observations and Weighing Matrices	53
5.3	Implementation of Model Reduced 4DVar	55
5.4	Single outer iteration experiments	59
5.5	Noisy Observations.	62
5.6	Discussion	64
6	Laboratory data assimilation: 19 parameters problem	67
6.1	Observations: laboratory set-up	68
6.2	Morphodynamic model	69
6.3	Implementation and results	72
6.3.1	Performance of the parameter estimation	73
6.3.2	Parameter sets	82
6.3.3	Model sensitivity to parameters	85
6.4	Discussion	87
7	Estimation with time exposure (Argus) images	89
7.1	Study area	90
7.2	Numerical model	90
7.3	Observations and Observation Operator	91
7.4	Roller energy dissipation in Delft3D	92
7.5	Implementation and Results	93
7.6	Discussion	102
8	Conclusions	105
8.1	Insights into future work	108
	Bibliography	109

Acknowledgments

This thesis is the outcome of the joint effort of many people that contributed either directly or indirectly in its development. First and foremost I would like to thank Prof. Dr. Ir. Arnold W. Heemink, for giving me the opportunity to work as a PhD candidate in his department. I am very grateful for his patience while I slowly built up the necessary knowledge to address the problem I was appointed to solve. This research would have not been possible without the commitment and help of Dr. Ghada El Serafy. Not only she procured all the necessary tools for the work to be carried out, but her concern for my personal well being is something I will always appreciate. Not often you find yourself in progress meetings that begin with a short discussion on personal matters, and find out that the technical content will have to wait until the next meeting. This approach to supervision was a constant reminder that without the researcher there is no research, and researchers don't only feed on books and papers (and coffee) to produce. I am in great debt with Dr. Henk Schuttelaars for his interest on the subject and unconditional support in the development of the work. His eagerness not only to teach me about wave dynamics and morphodynamic modeling matches his interest in learning about data assimilation. Very few times I have had the privilege to go from pupil to lecturer and back to pupil in the same meeting. To Dr. Martin Verlaan I am very thankful for courageously accepting, once and again, to answer my yes-no questions. It takes a great deal of serenity to willingly answer a "short" question, knowing that an endless discussion will follow on the possible (and impossible, depending on my level of confusion) implications of his assertion. To this day I wonder how he booked those hours.

To Pablo, Friedi, Layla and Barbara thank you for becoming my family. I don't think I would have been able to pick a better one myself. Dr. Remus Hanea and Dr. Joanna Pelc your help was certainly very important for this research and your friendship during these 5 years means a great deal to me. Remus, thank you for encouraging me to aim higher than my own reasoning suggested. Joanna you helped me more than you know to get through this PhD. I owe to all my friends for the great time that I have had in the Netherlands.

Finally, I will always be grateful to my family, Leonor, Orlando and Carolina. With-

out their devotion and support none of this would have been possible. Everything I am, I owe to them. This PhD is in fact theirs.

Ivan Garcia,
Delft, May 2013.

Summary

Currently, available models are not able to accurately predict the temporal evolution of coastal morphodynamic processes. The main reason for this, is that essential components governing this evolution are neither fully identified nor understood. Additionally, there is high uncertainty in some of the parameterizations and their input parameters. A proper management of coastal systems depends on a thorough understanding of their present and future state. Regarding the present state of the system, detailed analyses that take into account the inference of human activities and interactions with other natural process may provide the required information to the decision makers. The evaluation of future states, on the other hand, is not possible without the use of data assimilation, i.e. integration of measurements and predictions in the context of formal uncertainty analysis. Despite the need to implement data assimilation, only recently the necessary coastal observations became available. Since then, the integration of data assimilation methods and coastal morphodynamic models have become the focus of ongoing research. Unfortunately, the implementation of these methods is not straightforward. Sequential data assimilation methods, such as ensemble Kalman filter, are practical to implement but their update usually breaks conservation laws and may easily result in model instabilities. Variational (adjoint based) schemes, on the other hand, preserve the physical integrity but require the implementation of an adjoint model which commonly matches in complexity the forward model.

This thesis is concerned with the implementation of a variational data assimilation method to improve the predictive skills of a commercial model by estimating its input parameters. Model reduced 4DVar was used to address the problem. This method is an adjoint-free variational method that uses a truncated first order Taylor approximation of the morphodynamic model to implement the data assimilation process. The construction of the Taylor approximation is considerably simpler than the development of a full adjoint model. Additionally, the method provides the sensitivity of the morphodynamic model with respect to the state and/or input parameter vector. Regarding the commercial morphodynamic model, on the other hand, the Delft3D suite was selected. Delft3D is a module based simulator that merges a wave module and a flow and morphodynamic module to produce a fully coupled wave, flow and

morphodynamic model.

To gain a better understanding of the method and the potential challenges of its implementation on a real application, the technique is first applied to a small study case with synthetic observations (twin experiment). In this *proof of concept*, three wave properties were estimated by assimilating observations of bathymetry. Different reduction strategies were implemented to characterize the method's performance and to assess the effects of uncertain observations on the results. The data assimilation method is able to improve the performance of the morphodynamic model and shows to be robust in the presence of noisy observations. Nevertheless, some difficulties are identified regarding the size and direction (sign) of the perturbations required for the finite difference estimations. In light of this finding, the implementation shows that it is necessary to increase the number of model executions to make the method more robust. Also, the test show problems in connection with the restarting capability of Delft3D. These problems have a significant impact on the accuracy of the finite difference estimations.

To address the issues found in the proof of concept, an alternative novel model reduction method is proposed: *ensemble model order reduction* (enMOR). The method computes the low rank linear approximation of the full model based on an ensemble similar to those used in Monte Carlo approaches (e.g. ensemble Kalman filter). This offers a number of advantages over the more common finite difference approach. For instance, the model executions necessary for this type of ensembles are not prone to numerical instabilities; making the implementation significantly more robust. The implementation time is considerably lower and the availability of such ensemble allows computing the model error covariance matrix, which was not available when the finite differences are used. Finally, the method does not requires the model to be restarted, solving altogether the problems identified during the implementation of this first experiment.

The enMOR method was partially implemented in a more realistic study case based on a set of laboratory measurements. The measurements were taken as part of an experiment aimed at studying rip current circulations in a morphodynamic system. A set of 12 bathymetric observations were assimilated into the morphodynamic model to estimate a set of 19 flow, wave and morphodynamic parameters. One data assimilation problem for each state transition (LBT, RBB, TBR, and LTT) is implemented in order to characterize the parameter changes in each case independently. The enMOR technique is only applied to the dynamic components of the linear approximation, the model sensitivities to input parameters are estimated with finite differences. This serves two purposes, (1) it allows to assess possible shortcomings in the implementation of the method, and (2) reliable model sensitivities are estimated to analyze the influence of each parameter in the dynamic evolution of the system. The results show that the evolution of the morphodynamic system cannot be easily captured by a constant set of parameters; it is necessary to consider some of the parameters as time dependent.

The results also show that the 2D model used is not able to reconstruct shallow and deep morphodynamic processes simultaneously. Nevertheless, the data assimilation is able to improve the overall performance of the model. The implementation of the enMOR shows no significant practical difficulty other than potential long estimation times for reduced order models of considerable size.

A full implementation of the enMOR method with a 3D model of the Egmond aan Zee system in The Netherlands is finally presented. A set of time exposure images are used to estimate roller energy dissipation maps that are assimilated into the model to estimate a set of 13 input parameters that include the time-dependent wave height and peak period. The results show that the data assimilation method is able to find a parameter set that considerably improves the model performance. The results also suggest that the predicted morphodynamic evolution of the model has been improved, enhancing the forecasting capacity of the system. The implementation of the method proved significantly more practical than the common finite difference approach. The complete data assimilation implementation only required a set of 40 forward model runs (commonly known as ensemble). The model is not restarted at any point to produce the piece wise linear approximation necessary in model reduced 4DVar and no finite difference was implemented in the process. Consequently, the implementation difficulties observed in the proof of concept are not an issue in this implementation. In conclusion, enMOR is a practical model order reduction method that can be used for data assimilation without any loss of performance.

Further developments are necessary to take advantage of the available information about the adjoint of the model. Its use in applications for observation network optimization and process characterization should be considered. Also, state estimation is probably the best manner for bathymetry estimation. On this regard, further research is necessary to assess the best manner to implement state estimation using model reduced 4DVar. Finally, an estimation of the expected errors of the reduced order models can be achieved by means of Monte Carlo methods. This information could be valuable to identify weaknesses in the reduced order model and therefore in the assimilation process.

Samenvatting

Op dit moment zijn morfodynamische modellen nog niet in staat de ontwikkeling van complexe bodempatronen in de kustgebieden nauwkeurig te voorspellen. De belangrijkste reden hiervoor is dat essentiële bijdragen aan deze bodemontwikkeling niet volledig gedentificeerd en begrepen zijn. Daarbij komt ook nog de grote onzekerheid in gebruikte parametrisaties en input variabelen. Voor een goed beheer is het juist essentieel dat zowel de hedendaagse als de toekomstige toestand goed wordt begrepen. Wat betreft de huidige toestand zou eventueel voldoende kennis kunnen worden verkregen door gedetailleerde analyses waarin zowel de invloed van menselijke activiteiten als natuurlijke ontwikkelingen worden beschouwd. Een goed inzicht in de toekomstige toestand kan in het algemeen alleen verkregen worden met behulp van data assimilatie, het integreren van metingen en voorspellingen in de context van een formele onzekerheidsanalyse. De noodzakelijke data zijn pas recentelijk beschikbaar, wat geresulteerd heeft in een sterke toename van onderzoek naar data assimilatie methoden voor kust-morfodynamische modellen in de afgelopen jaren. De implementatie van deze methoden is echter niet eenvoudig. Sequentiele data assimilatie methoden, zoals ensemble Kalman filters, zijn relatief eenvoudig te implementeren, maar meestal voldoen de updates niet aan de behoudswetten en kan het morfodynamische model numeriek instabiel worden. Met variationele (gebaseerd op de geadjungeerde) schema's worden de fysische behoudswetten niet geschonden, maar deze methode vereist de implementatie van een geadjungeerd model, wat niet eenvoudig te ontwikkelen is.

In dit proefschrift wordt een variationele data assimilatie methode gecomplementeerd om de voorspellende kwaliteiten van een commercieel model te verbeteren door schatting van de benodigde invoerparameters. De gebruikte data assimilatie methode is de model-gereduceerde 4DVar methode, een variationele methode waarbij de geadjungeerde niet wordt gebruikt. In plaats daarvan wordt een eerste orde Taylor benadering van het morfodynamische model gebruikt. Het construeren van de Taylor benadering is veel eenvoudiger dan het ontwikkelen van een volledig geadjungeerd model. De methode geeft de gevoeligheid van het morfodynamische model voor de toestands- en/of input-parameter vector. Als commercieel morfodynamisch model is het Delft3D pakket gebruikt, een modulaire simulator die een golfmodule, stromingsmodule en

morfodynamische module combineert tot een volledig gekoppeld model.

Om de methode beter te begrijpen en inzicht te verkrijgen in eventuele onvoorziene problemen in de implementatie, is deze techniek eerst toegepast op een klein probleem met synthetische data (een 'twin experiment'). In dit experiment worden drie golfeigenschappen geschat door observaties van bodemdieptes te assimileren in het morfodynamische model. Verschillende strategieën zijn gecomplementeerd om de effectiviteit van de methode te karakteriseren en de invloed van onzekerheden in observaties te schatten. Het blijkt dat de data assimilatie methode in staat is de morfodynamische modelresultaten te verbeteren. Verder is de methode robuust voor observaties met ruis. Tijdens dit experiment is geconstateerd dat de keuze van de grootte en richting van de verstoringen, nodig om eindige differenties te schatten, problemen kan geven. Om de methode robuust te maken, is het daarom nodig het aantal modelruns te verhogen. Verder laat dit testprobleem zien dat het herstarten van het morfodynamische model Delft3D problemen geeft. Deze problemen hebben een significante invloed op de nauwkeurigheid van de eindige differentie schattingen.

Om bovengenoemde problemen aan te pakken, is er een alternatieve, nieuwe modelgereduceerde methode ontwikkeld: *ensemble model order reduction* (enMOR). Deze methode berekent een lineaire benadering met lage rang van het volledige model, gebaseerd op een ensemble zoals gebruikt in Monte-Carlo methoden (e.g. ensemble Kalman filter). Dit resulteert in een aantal voordelen ten opzichte van de gebruikelijke eindige differentie aanpak. Zo zijn de modelruns niet gevoelig voor numerieke instabiliteiten, resulterend in een veel robuustere implementatie. Verder is de implementatietijd veel kleiner, kan het ensemble gebruikt worden om de covariantie matrix voor de modelfouten te berekenen, en hoeft het morfodynamische model niet herstart te worden.

De enMOR methode is eerst gedeeltelijk gecomplementeerd in een meer realistisch experiment, gebaseerd op laboratorium metingen van muistromingen. Twaalf bodemobservaties zijn in het morfodynamische model geassimileerd, waarmee 19 stromings-, golf-, en morfodynamische parameters zijn geschat. Om de parameter veranderingen per toestandsovergang (LBT, RBB, TBR en LTT) te kunnen karakteriseren, is de data assimilatie methode per overgang toegepast. De nieuwe enMOR-methode is alleen toegepast op de dynamische componenten van de lineaire benadering, de parametergevoeligheden zijn nog geschat met eindige differenties. De resultaten laten zien dat de morfodynamische ontwikkeling niet eenvoudig kan worden gereproduceerd met vaste parameterwaarden, het is nodig een aantal parameters tijdsafhankelijk te maken. Verder blijkt dat het 2D model niet in staat is de morfodynamische processen in zowel de ondiepe als diepe gebieden gelijktijdig te reproduceren. Desondanks is de enMOR methode in staat de modelresultaten te verbeteren. De implementatie van de enMOR methode heeft niet geresulteerd in essentiële problemen, de methode kan echter wel resulteren in lange schattingstijden voor relatief grote gereduceerde modellen.

In de laatste toepassing is de enMOR methode gecomplementeerd voor een 3D model

van de kust bij Egmond aan Zee in Nederland. Hierbij zijn tijdsgemiddelde beelden gebruikt om de dissipatiepatronen van de roller energie te schatten. Deze dissipatiepatronen zijn in het model geassimileerd om 13 invoerparameters, zoals de tijdsafhankelijke golf hoogte en piek periode, te schatten. Met behulp van het data assimilatie proces zijn parameters gevonden die de modelresultaten flink hebben verbeterd. De resultaten suggereren ook dat de voorspelde morfodynamische evolutie is verbeterd, wat betekent dat de voorspellende kwaliteit van het systeem is toegenomen. De implementatie van de enMOR methode is veel praktischer dan die van de gebruikelijke eindige differentie methode. Voor de gehele implementatie waren slechts 40 model runs (ensemble) nodig. Het model is niet herstart om lineaire benaderingen te maken zoals in de model-gereduceerde 4DVar methode. De nieuwe enMOR methode is dus een praktische model-reductie methode, die gebruikt kan worden in data assimilatie zonder verlies aan performance.

Meer onderzoek is nodig om optimaal gebruik te kunnen maken van de aanwezige informatie over de geadjungeerde van het model voor bijvoorbeeld optimalisatie van waarnemingsnetwerken en karakterisering van processen. Also, state estimation is probably the best manner for bathymetry estimation. On this regard, further research is necessary to assess the best manner to implement state estimation using model reduced 4dVar. Verder kunnen de verwachte fouten van het gereduceerde model geschat worden met behulp van Monte Carlo methodes. Deze informatie kan worden gebruikt om zwakke punten in het gereduceerde model te identificeren, wat direct consequenties heeft voor het assimilatie proces.

Chapter 1

Introduction

Decision support systems (DSS) use predictions and their uncertainties to produce risk assessments (e.g. early alarm systems or actuarial science) or prospective scenarios for characterization and control activities (as in environmental impact analyses). Reducing the uncertainty in the predictions is fundamental to both risk assessment and prospective characterization. To this end, data assimilation combines information coming from observations and models to produce estimations of minimal uncertainty. Complex mathematical models are used to predict the behavior of the variables of interest in time. As measurements of these variables become available, the performance of the mathematical model can be tested by comparing its results with the observations. This comparison produces information that is used for improving the model estimations. This process is commonly called *data assimilation* and comprises the joint analysis of the prediction error distribution, observation error distribution and the distribution of the deviations between the model and the observations.

This thesis studies the potential use of data assimilation in the field of morphodynamic modeling for uncertainty minimization. In contrast with the state of hydrodynamic models, morphodynamic modeling displays considerably higher uncertainties limiting the reliability of DSSs built upon them. Regarding forecasting skills, the prediction horizon depends on the processes of interest. [Walstra et al. \(2012\)](#), for example, was able to predict the temporal evolution of sandbar positions for up to 3 years using a morphodynamic profile model. In the presence of extreme weather conditions, nevertheless, [Ruessink and Kuriyama \(2008\)](#) showed that severe storms can have a significant effect on the performance of these types of models. Still, nowadays profile models are able to predict accurately the location of the bar. Alongshore variability, on the other hand, is the outcome of highly dynamic processes and is therefore less predictable. Also, alongshore features tend to exist for relatively short periods of time (~weeks). Consequently, forecasts from state-of-the-art 2D-areal and 3D morphodynamic models are still limited to few days; especially so, when considering complex

bathymetries due to evolving rip channels and other similar features (van Dongeren et al., 2008). For these type of models the uncertainties are so high, that morphodynamic analyses are usually focusing on general morphodynamic pattern evolution rather than detailed local depth changes.

There are a number of reasons for the low predictive skills of 2D-areal and 3D morphodynamic models. A significant number of the modeled processes are based on relationships approximated from experimental results (van Rijn, 2007a,b,c). Thus, the mathematical description of these processes is a mixture of physical concepts and mathematical approximations that may not be applicable to conditions outside the laboratory. Also, the substantial differences in spatial and temporal scales at which several processes take place make the modeling process difficult. Spatially, for example, circulation currents that may cover kilometers are as important in the model outcome as horizontal eddies of sizes in the order of magnitude of meters and turbulence processes that involve microscopic processes. To model accurately horizontal eddies of sizes in the order of magnitude of tens of meters, the size of the mathematical model (due to its resolution) becomes a limiting factor; let alone turbulence. Furthermore, despite the recent increase in computer power it is still common practice to implement depth averaged models due to the intensive computational requirements of three dimensional modeling. Finally, the implementation of morphodynamic models is information intensive and a considerable amount of input data is prone to high uncertainties (e.g. satellite information).

Using data assimilation for morphodynamic modeling may contribute significantly to lowering the predictions' uncertainty. Data assimilation makes use of two strategies to improve the modeling estimations: *state estimation* and *parameter estimation*. The model errors are usually addressed with state estimation, and these include incompleteness of the mathematical model and numerical errors (resolution and numerical solution). Input uncertainties, on the other hand, are addressed by estimating the parameters. As a result, data assimilation is expected to produce an improvement of the model capacity to reconstruct the system's behavior and prediction skills.

Here a variational data assimilation technique, model reduced 4DVar (Vermeulen and Heemink, 2006), is implemented on a well established open-source integrated wave-current-sediment numerical model, Delft3D. In model reduced 4DVar, the parameter estimation process is implemented via a minimization process that assumes uncertain model parameters and observations. Model reduced 4DVar is an adjoint-free variational data assimilation technique that uses a reduced order model to approximate the adjoint model of Delft3D. In essence, model reduced 4DVar extends *incremental 4DVar* (Courtier et al., 1994) by projecting the tangent linear model to a reduced space estimated via principal component analysis (PCA). The Delft3D suite is a process-based set of simulators capable of modeling wave dynamics, flow evolution and sediment transport. It is the result of over 20 years of code development, aimed at reconstructing hydrodynamic and morphodynamic evolution of water systems under

various forcing conditions. The suite consists of two coupled models: a wave simulator (SWAN) and a hydrodynamic, sediment transport and bed update simulator (FLOW). Since one of the major objectives of this research is to contribute to the minimization of uncertainties on practical morphodynamic modeling applications, the Delft3D suite constitutes a good candidate to assess the limitations of data assimilation. It has been used intensively for research and commercial applications in a large number studies. Also, it includes all the relevant physical processes and offers the possibility to build 3D morphodynamic models. Finally, at the time in which this research was initiated other now available choices, such as X-Beach (Roelvink et al., 2009), were not available.

1.1 Problem description

Recent developments in coastal measuring techniques have provided a wealth of observations (information) that was not available before. Time exposure images (Holman et al., 2013; van Dongeren et al., 2008), in coastal areas, and radar-based methods, also used in open seas, are now able to provide *on-line* information about the current state of the observed system. Despite high uncertainties in the measurements (Uunk et al., 2010), the amount of information is such that they have cleared the way to implement data assimilation for morphodynamic modeling. It is the author's opinion that the use of these sources of information in combination with appropriate data assimilation methods are fundamental to the implementation of an operational morphodynamic prediction system.

The high uncertainties typical of coastal morphodynamic models justify the use of data assimilation; but their complexity poses challenges for its implementation (see de Vriend et al., 1993, for a detailed review). Sequential methods such as ensemble Kalman filter are practical to implement but their update usually breaks the conservation laws and may easily result in model instabilities. Variational schemes (or adjoint based schemes) preserve the physical integrity of the process but require the implementation of an adjoint model which commonly matches in complexity the forward model. The adjoint model is a tool capable of estimating the sensitivity of model output with respect to the inputs at each point in time (if the forward simulator works with time). The availability of the adjoint model offers several advantages for system analysis. In particular, it provides the necessary information for detailed sensitivity analysis which can be used for observation network optimization and process characterization. Adjoint-free variational methods use an approximation of the adjoint model to produce an estimate of the real sensitivities used in the data assimilation. The approximation is a trade off, its implementation is considerably simpler but the result of the data assimilation is sub-optimal. Nevertheless, the scheme preserves the physical laws, avoids the construction of the adjoint model and offers some advantages in terms of system characterization.

In the author's opinion, variational schemes are the most appropriate data assimi-

lation strategies for coastal morphodynamic models. Not only because they preserve the physical integrity of the process, but also because of the potential use of the model sensitivities for further optimizing the system's performance. In this study an adjoint-free *model reduced 4DVar* scheme (Vermeulen and Heemink, 2006) has been used to assess the potential of data assimilation for morphodynamic modeling. The method is in line with the approach discussed by Vos et al. (2000), where he suggests that the temporal evolution of the studied system could be taken into account via the adjoint model. The research project have been designed and implemented to address the following **research questions**:

- Can model reduced 4DVar be used to estimate parameters of coastal morphodynamic models implemented in the Delft3D suite?
- In terms of modeling abilities of Delft3D, what improvements should be expected from the implementation of model reduced 4DVar?
- Is it feasible to use model reduced 4DVar in an operational forecasting morphodynamic system?

1.2 Models, model errors and data assimilation.

The development and implementation of models for the simulation of natural processes is a challenge in many ways. Its success depends upon a good understanding of the underlying physical processes, a good mathematical representation of these processes and advanced numerical solution strategies. Even when all the previous conditions have been met, success still depends on the appropriate estimation of many uncertain model parameters. Even though it is unquestionable that the modeling process is subject to errors, very few disciplines have devoted serious efforts to include data assimilation in their estimations. In the case of meteorology, however, model errors grow so fast that data assimilation is at the heart of meteorological forecasting. In other fields of science where modeling errors do not render the forecasts useless, uncertainty analysis is not commonly used.

Model uncertainty arises from different sources. Errors associated to a *deficient conceptualization* of the relevant physical processes are structural and can only be fixed by improving the physical understanding of the system and updating the model. A second important source of errors is a deficient numerical implementation of the model. There are a lot of causes for numerical errors and, in general, they are pervasive and unavoidable. It is not a matter of whether numerical errors exist, it is a matter of how big they are and how they propagate in time and space. The spatial discretization of the system, for instance, limits the model's capacity to deal with processes of smaller scale than the discretization. The numerical implementation of the mathematical model also plays a determining role in error generation. Take for example the logistic map (see equations 1.1 and 1.2), this is an extreme but clear

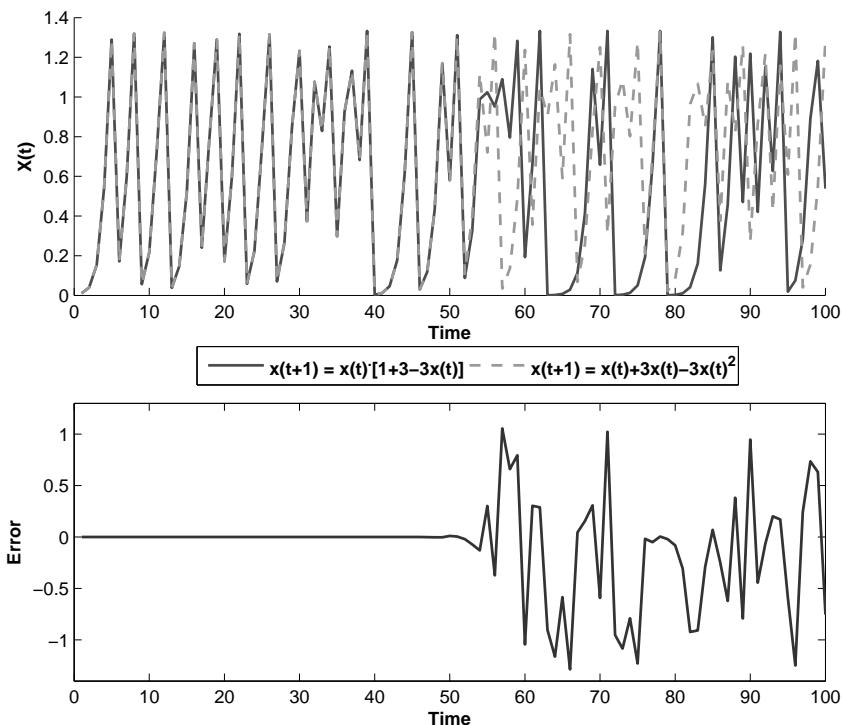


Figure 1.1: Consequences of different numerical implementations of the same dynamic model.

example of the consequences of slightly different implementations of the same mathematical relation. Here the same dynamical model is solved by using the following two mathematically equivalent forms,

$$x_{t+1} = x_t + 3x_t - 3x_t^2, \quad (1.1)$$

$$x_{t+1} = (1 + 3 - 3x_t)x_t, \quad (1.2)$$

where x_t is a scalar and t indexes time. Notice that these two relations are in fact the same function. They define the exact same dynamic model and yet the differences between the two solutions are of the same order of magnitude as the range of the function, see figure 1.1 ($X_0 = 0.01$ in both cases). Furthermore, which of the two solutions is the correct one?

Other sources of error in the model results include: uncertain model parameters and boundary conditions, empirical relations (common in morphodynamic modeling), re-parameterization of processes (e.g. in turbulence) and uncertain forcings. The rate of growth of these errors depends on the mathematical characteristics of the model and on its numerical implementation. In the case of the logistic model (presented

previously) even the smallest error will eventually render the estimations obsolete.

Aside from improving the understanding of relevant physical processes and enhancing the implementation of the mathematical model, errors can only be minimized by means of parameter- and state-estimation framed in the context of uncertainty analysis: i.e. data assimilation.

1.3 Morphodynamic modeling

The remarkable progress observed in hydrodynamic modeling along with nowadays available computational power is providing an appropriate setting for morphodynamic modeling. In the case of coastal morphodynamic modeling, intense work is currently underway to improve model capabilities and the result's quality. Assessments of models' skills to reconstruct observed bathymetric evolution are common in the literature. Some examples are, [Ranasinghe et al. \(2004\)](#) who uses a 2DH (2 dimensional depth averaged) finite difference coastal area model to simulate the morphodynamic processes and compares its results with data derived from video based observations. [Carniel et al. \(2011\)](#) examines the qualitative performance of a high resolution wave-current-sediment numerical model with respect to observations coming from an ARGUS video station. [Davidson et al. \(2013\)](#) tests the performance of a simple morphodynamic model to predict shoreline changes attained from ARGUS derived information.

Parallel to the improvement of morphodynamic simulators, the use of data assimilation for coastal morphodynamic modeling has increased during the last decade. Remotely sensed data is providing the necessary information and is having a significant effect on the way coastal- and (more generally) ocean models are being implemented and used. Satellite imagery for the case of ocean models, and radar and Argus images for the case of coastal models are providing enough information to exploit the advantages of data assimilation. An increasing number of works that combine data assimilation techniques and hydrodynamic and morphodynamic models are found in the literature. In the case of data assimilation for the Delft3D suite the author is only aware of the works by [van Dongeren et al. \(2008\)](#) and [Briere et al. \(2011\)](#). In the former, a sequential scheme based on the Kalman filter is used to reconstruct coastal bathymetries from ARGUS images. In the latter, a cost function that measures model mismatches is minimized using the DUD algorithm [citepralston1977](#). More general applications of data assimilation for nearshore modeling include [Scott and Mason \(2007\)](#) who assimilated satellite observations of waterlines into a 2D horizontal (2DH) decoupled morphodynamic model to optimize the bathymetric estimations of the intertidal area for the Moracambe Bay. [Smith et al. \(2012\)](#) and [Thornhill et al. \(2012\)](#) implemented a 3D variational data assimilation scheme for the Morecambe Bay to incorporate bathymetry observations derived from various sources into morphodynamic models. [Wilson et al. \(2010\)](#) used the ensemble Kalman filter for estimating bathymetries, by using bathymetric observations and a two dimensional horizontal model of

nearshore hydrodynamics. Birrien et al. (2011) used a laboratory dataset to implement an analysis-step based on the Kalman filter. More recently, Holman et al. (2013) uses time series observations of surface wave motions to estimate bathymetry maps by implementing a Kalman filter to solve coverage gaps and make map estimates.

1.4 Data assimilation scheme: Model reduced 4DVar

Model reduced 4DVar (mr4Dvar) is an adjoint-free variational method that approximates the adjoint model by using a truncated first order Taylor approximation of the forward simulator. This approximation is considerably simpler to implement than the full adjoint model. The method provides the sensitivity of the morphodynamic model with respect to the state and/or input *parameter** vector. This information can be used to identify parameters that have a significant influence on the behavior of the model; and for appropriate approximations, this adjoint model could be useful for observation networks optimization (Daescu and Carmichael, 2010). Previous applications of model reduced 4DVar have been done by Altaf et al. (2009) who used it for shallow-water flow modeling, and Pelc et al. (2012) who used it in ecosystem modeling.

Here, the original scheme proposed by Vermeulen and Heemink (2006) has been modified to avoid the use of finite differences. The implementation of the Gateaux derivative is not straightforward in the case of morphodynamic models because it is prone to generate model instabilities. To avoid their computation an alternative model reduction method was proposed and tested: *ensemble model order reduction*. The method computes a linear approximation of the full model based on an ensemble similar to those used in Monte Carlo approaches (e.g. ensemble Kalman filter). This offers a number of advantages over the traditional finite difference approach. For instance, the model simulations necessary for this type of ensembles is not prone to instabilities; which makes the implementation more efficient and reliable. The implementation time is considerably lower and the availability of such ensemble allows computing the model error covariance matrix, which was not available when the finite differences are used.

1.5 Implementations

Three sets of observations were used throughout the research project presented here. The first implementation aims to be a proof of concept, and is mainly concerned with identifying unforeseeable difficulties in the use of data assimilation with Delft3D. It consists of a small implementation of mr4dvar with 3 wave parameters and synthetic observations of bathymetries (twin experiment). The implementation shows important challenges in the implementation process. In particular the propensity of the model to

*Here a parameter is understood as any forcing, input parameter or boundary condition of interest. It refers to any model-input in a mathematical sense.

crash during the estimation of the finite differences and the significant errors generated by re-starting the model. In the second implementation of the method a set of detailed laboratory measurements of water depths is used. The main aim of the laboratory experiment is to study the evolution of coastal systems from high energy to low energy states (Michallet et al., 2013, 2010; Castelle et al., 2010). In this implementation a set of 19 parameters that includes wave, flow and morphodynamic components is estimated. The data assimilation is done by combining the finite difference based model order reduction and the ensemble reduced order model method. Finally, a set of time exposure images of Egmond aan Zee are used to estimate a set of 13 parameters two of which are vectors (effectively 20 parameters). In this test the ensemble based reduced order model is used to construct a reduced linear approximation that include flow components, time varying wave forcings and morphodynamic components. In general, the use of data assimilation not only contributes to the improvement of the modeling skills but also serves to diagnose and characterize the modeling process. The proposed method proved to be 3 times faster than the more common finite difference method. Also the two methods for model reduction seem to perform satisfactorily.

1.6 Reading guide

This thesis consists of 8 chapters and is organized as follows:

- Chapter 2 presents a historical review of the field of data assimilation along with the theoretical background is explained.
- Chapter 3 shows the mathematical background of model reduced 4DVar and a detailed description of a new alternative method for estimation of reduced order models.
- In chapter 4, the modeling suite Delft3D is described. In it, the reader will also find a discussion on some relevant numerical issues that came across during the development of the research.
- Chapter 5 presents the results of the proof-of-concept implementation. The experiment aims to estimate three wave parameters by using a set of synthetic observations. An interesting characterization of some of the model reduced 4DVar properties is presented there.
- Chapter 6 presents the results of a modified model reduced 4DVar implementation for a laboratory experiment. Here the proposed alternative method for model order reduction is partially implemented.
- Chapter 7 shows the results of the implementation of the data assimilation scheme using the alternative proposed method for model order reduction. The experiment is implemented for a set of real time exposure images taken on

Egmond aan Zee, The Netherlands. A discussion on some of the advantages and disadvantages of the proposed method is included in this chapter.

- Finally, a summary of the most relevant results from each implementation is presented in chapter 8. This chapter also provides information about open challenges and unresolved problems.

Chapter 2

A review of data assimilation

"The absence of evidence was taken as evidence of absence. The great difficulty of observing the ocean meant that when a phenomenon was not observed, it was assumed it was not present. The more one is able to observe the ocean, the more the complexity and subtlety that appears."
Wunsch (2002)

Data assimilation addresses the problem of estimating the true state of the system based on both the model information and the observations. To this end, the mathematical model is required to be written in state space representation. In general, the *state space representation* consists of two equations, the state equation (eq. 2.1) and the observation equation (eq. 2.2). In most applications the dynamic system is assumed to be discrete in time. Consider a discrete dynamic system,

$$\mathbf{x}_{k+1}^t = f_k(\mathbf{x}_k^t, \boldsymbol{\alpha}_k) + \boldsymbol{\omega}_{k+1}, \quad (2.1)$$

where $\mathbf{x}_k^t \in \mathbb{R}^n$ is the true state vector at time $t_k (k \in \mathbb{N})$. This state vector consists of the dynamic variables of the system. The input vector, $\boldsymbol{\alpha}_k \in \mathbb{R}^m$, consists of the model parameters and forcings at time t_k . The process noise $\boldsymbol{\omega}_{k+1} \in \mathbb{R}^n$ represents the model error and $f_k(\cdot, \cdot)$, the dynamic model, is usually a nonlinear equation that defines the state's transition from time t_k to time t_{k+1} . In the context of morphodynamic modeling of coastal systems the function $f_k(\cdot, \cdot)$ in equation 2.1 encompasses the system of nonlinear equations that simulates the wave and water motion, sediment transport and bed evolution (as described in chapter 4).

The observation equation relates the state vector to some measured quantity, $\mathbf{y}_k \in \mathbb{R}^o$, at time t_k . In general the observation equation can be written as:

$$\mathbf{y}_k = h_k(\mathbf{x}_k^t, \boldsymbol{\alpha}_k) + \boldsymbol{\nu}_k, \quad (2.2)$$

where $\boldsymbol{\nu}_k \in \mathbb{R}^o$ is the observation noise representing measurement errors, \mathbf{x}_k is the model forecast, and the nonlinear function $h_k(\cdot, \cdot)$ is usually known as observation operator and maps the model results to the measurements.

The result of the data assimilation process at time t_k , $\mathbf{x}_k^a \in \mathbb{R}^n$, is commonly known as the *analysis*. From a statistical point of view the estimation of the state is equivalent to finding the minimum variance unbiased estimator of the real state of a system. The solution to the problem is not straightforward and various methods have been used to find it.

2.1 Optimal interpolation and Kalman filter

In the early days of data assimilation in weather prediction (probably the first field of data assimilation development) the predictions were *hand-optimized* based on the modeler's experience and judgment. This process is called subjective analysis. The first mathematically formal method to become popular is optimal interpolation initially presented by Eliassen (1954), for the univariate case, and then used by Gandin (1963), for the multivariate case. The method is still used in many fields and amounts to an objective analysis step (the concept is presented further down). Simultaneous to Gandin's publication, Bucy (1959) and Kalman (1960) developed the ideas that led to the Kalman-Bucy filter (Kalman and Bucy, 1961), which is a significant extension to optimal interpolation as it includes uncertainty propagation in time.

In both optimal interpolation and Kalman filtering, an objective analysis step takes place at each time an observation is made available. The difference is that while optimal interpolation is a method that implements an *analysis step* alone, the Kalman-Bucy filter is a method that implements both uncertainty propagation in time and an analysis step. Since the methods discussed in this section are restricted to linear forward models and observation operators, the remainder of this section will address state spaces representations given by (consistent with equations 2.1 and 2.2),

$$\mathbf{x}_k^t = F_k \mathbf{x}_{k-1}^t + G_k \boldsymbol{\alpha}_{k-1} + \boldsymbol{\omega}_k, \quad (2.3)$$

$$\mathbf{y}_k = H_k \mathbf{x}_k^t + \boldsymbol{\nu}_k. \quad (2.4)$$

Here $H_k \in \mathbb{R}^{o \times n}$ is the observation operator at time t_k , $F_k \in \mathbb{R}^{n \times n}$ and $G_k \in \mathbb{R}^{n \times m}$ are transition matrices that map the state vector and the input vector at time t_{k-1} to a prediction/estimation of the state at time t_k . The term $\boldsymbol{\nu}_k$ represents the observation error. The term $\boldsymbol{\omega}_k$ represents the model error at time t_k .

An objective analysis consists of an optimal least squares estimation that can be written as follows:

$$\mathbf{x}_k^a = \mathbf{x}_k + K_k (\mathbf{y}_k - H_k \mathbf{x}_k), \quad (2.5)$$

where $K_k \in \mathbb{R}^{n \times o}$ is a weighing matrix commonly known as *gain matrix* that is computed based on the model error and the observation error covariance matrices. The observation error and the model error are assumed to be normally distributed

with covariance matrices $R_k \in R^{o \times o}$ and $P_k \in \mathbb{R}^{n \times n}$, respectively. The assumption of normality is fundamental for the KF because it enables the propagation of the model uncertainty in time. The difference ($\mathbf{y}_k - H_k \mathbf{x}_k$) is usually referred to as *innovation*. In optimal interpolation the model error covariance matrix is usually constructed in an ad-hoc manner. In the KF this error covariance matrix is computed based on the model dynamics (further discussion will follow).

The gain matrix that minimizes the analysis' uncertainty is given by*:

$$K_k = P_k H_k' (H_k P_k H_k' + R_k)^{-1}. \quad (2.6)$$

where H_k' is the transpose matrix of the observation operator H_k . In KF the fact that the dynamic model is linear enables the model error covariance matrix, P_k , to be computed at each time step as part of the method. Bear in mind that a linear combination of normal distributions is normally distributed. The propagation of the model uncertainty can be easily computed at each time step by solving:

$$P_k = F_k P_{k-1} F_k' + C_{k-1}, \quad (2.7)$$

where F_k' is the transpose of the model dynamics matrix. Information about the input parameters error covariance matrix is usually obtained from expert knowledge. The result of equation 2.7 is used to compute the Kalman gain (eq. 2.6).

The capacity to propagate the model uncertainties in time (provided by equation 2.7) is a significant improvement over optimal interpolation. The most restrictive assumption is that the model dynamics and the observation operator must be linear. This assumption is unacceptable in most fields of study. Aside from this, if the forward model consists of 100 by 100 gridcells in the horizontal and 10 layers in the vertical direction, the state vector has 10^5 elements. The covariance matrix of such a state vector has 10^{10} elements that if defined as single-precision floating-point format will take over 30 GB of space. Uploading to memory this amount of information is challenging; let alone, producing it on every forward step of the forecasting system. For this reason the KF is not used in applications of considerably size.

The use of both optimal interpolation and the Kalman-Bucy filter became widespread in the 70's and 80's. Optimal interpolation was the data assimilation method of choice in weather prediction. The Kalman-Bucy filter quickly became common use in fields such as control systems, navigation systems and avionics; and was implemented in projects of such magnitude as the Apollo program. As a matter of fact, its implementation for the Apollo program resulted in the formulation of the Extended Kalman Filter (EKF) (McElhoe, 1966; McGee et al., 1962). In the EKF the non-linear dynamic model is linearized by means of a truncated Taylor expansion (see McGee et al., 1962). This adaptation of the method makes the result sub-optimal, but it is a significant improvement in terms of flexibility. Unfortunately for models of considerable size the linearization process of the model is usually unfeasible.

*The derivation of the gain matrix can be found in:
www.asp.ucar.edu/colloquium/1992/notes/part1/node121.html

2.2 Variational methods

At the same time as optimal interpolation and the KF were being implemented and used in different fields, the adjoint method to estimate model sensitivities started to get considerable attention. One of the first publications to mention the use of adjoint functions for sensitivity analysis was done by Wigner (1945) as a report for the Manhattan project. In the beginning of the 80's, Dan Cacuci (Cacuci et al., 1980; Cacuci, 1981a,b) picked up the subject and formally introduced the concepts of sensitivity analysis by using concepts of nonlinear functional analysis. Shortly after this, a series of works that assessed the potential of the adjoint method as a data assimilation tool were developed (Le Dimet, 1982a,b; Lewis and Derber, 1985; Courtier, 1985); which ultimately led to the pivotal work by Le Dimet and Talagrand (1986).

In adjoint based data assimilation methods, the estimation problem is defined as a minimization of an objective function that measures the distance between the output vector and the observations. Consider the following objective function,

$$J(\boldsymbol{\alpha}_1, \boldsymbol{\alpha}_2, \dots, \boldsymbol{\alpha}_{l-1}) = \sum_{k=1}^l \left[\frac{1}{2} (\boldsymbol{\alpha}_{k-1} - \boldsymbol{\alpha}_{k-1}^0)' B_{k-1}^{-1} (\boldsymbol{\alpha}_{k-1} - \boldsymbol{\alpha}_{k-1}^0) \right] \\ + \sum_{k=1}^l \left[\frac{1}{2} (h_k(\mathbf{x}_k, \boldsymbol{\alpha}_k) - \mathbf{y}_k)' R_k^{-1} (h_k(\mathbf{x}_k, \boldsymbol{\alpha}_k) - \mathbf{y}_k) \right].$$

subject to $\mathbf{x}_k = f_k(\mathbf{x}_{k-1}, \boldsymbol{\alpha}_{k-1})$, the state estimate at time t_k , the estimation vector at time t_{k-1} is given by $\boldsymbol{\alpha}_{k-1}$, and $\boldsymbol{\alpha}_{k-1}^0$ the initial choice of the input vector (commonly known as *prior*) at time t_{k-1} . Matrices B_{k-1} and R_k are the error covariance matrices of the prior at time t_{k-1} and of the observations at time t_k , respectively. Notice that the dynamic model, $f_k(\cdot, \cdot)$, and the observation operator, $h_k(\cdot, \cdot)$, are not necessarily linear. Nevertheless, for convenience, in the rest of the section the observation operator will be assumed to be a linear map, $h_k(\cdot, \cdot) = H_k$. The forward model, $f_k(\cdot, \cdot)$, on the other hand, will remain nonlinear, in which case the cost function can be rewritten as,

$$J(\boldsymbol{\alpha}_1, \boldsymbol{\alpha}_2, \dots, \boldsymbol{\alpha}_{l-1}) = \sum_{k=1}^l \left[\frac{1}{2} (\boldsymbol{\alpha}_{k-1} - \boldsymbol{\alpha}_{k-1}^0)' B_{k-1}^{-1} (\boldsymbol{\alpha}_{k-1} - \boldsymbol{\alpha}_{k-1}^0) \right] \\ + \sum_{k=1}^l \left[\frac{1}{2} (H_k \mathbf{x}_k - \mathbf{y}_k)' R_k^{-1} (H_k \mathbf{x}_k - \mathbf{y}_k) \right]. \quad (2.8)$$

The adjoint method is in fact an efficient way to estimate function derivatives and Cacuci's work showed how it works for non-linear functions. It works by defining the estimation of the function derivative in terms of differentials provided by the chain rule,

$$\nabla_{\boldsymbol{\alpha}_{k-1}} J = B_{k-1}^{-1} (\boldsymbol{\alpha}_{k-1} - \boldsymbol{\alpha}_{k-1}^0) + \{\nabla_{\boldsymbol{\alpha}_{k-1}} f_k\}^* H_k' R_k^{-1} (H_k \mathbf{x}_k - \mathbf{y}_k), \quad (2.9)$$

where $\nabla_{\alpha_{k-1}} f_k$ stands for the Jacobian of $f_k(\mathbf{x}_{k-1}, \alpha_{k-1})$ with respect to α_{k-1} , and is in fact the sensitivities of the model to input parameters. The term $\{\nabla_{\alpha_{k-1}} f_k\}^*$ denotes the adjoint of the model Jacobian (see, Giering and Kaminski, 1998; Errico, 1997). For most of the forward dynamic models, the adjoint operator is equivalent to the transposition operator (from now on it will be assumed that this is the case).

For models defined in state space form, the adjoint method becomes powerful by enabling the estimation of the model gradient with respect to the initial parameters in a recursive manner,

$$\begin{aligned} \nabla_{\alpha_0} f_k(\mathbf{x}_{k-1}, \alpha_{k-1}) &= \nabla_{\mathbf{x}_{k-1}} f_k(\mathbf{x}_{k-1}, \alpha_{k-1}) \nabla_{\mathbf{x}_{k-2}} f_{k-1}(\mathbf{x}_{k-2}, \alpha_{k-2}) \\ &\dots \nabla_{\mathbf{x}_1} f_2(\mathbf{x}_1, \alpha_1) \nabla_{\alpha_0} f_1(\mathbf{x}_0, \alpha_0). \end{aligned}$$

The model gradient at each time step can be implemented with the help of code differentiation (Griewank, 1989; Baur and Strassen, 1983; Giering and Kaminski, 1998) to produce the *adjoint model*. Unfortunately, the construction and maintenance of adjoint codes is very demanding. For complex systems subject to constant updating, considerable efforts must be devoted to keep an operational adjoint model. Only for linear models, the adjoint model comes at no expense.

From an implementation point of view, the data can be assimilated sequentially as observations come (sequential estimator), or within an assimilation window were measurements at different times are used to estimate the initial state and/or input parameters (smoother). The sequential estimator is commonly known as 3DVar and it is equivalent to computing an objective analysis (Courtier, 1997). The smoother, on the other side, is commonly known as 4DVar and it uses the adjoint model to propagate the uncertainties within the assimilation window. The use of the adjoint model is advantageous when compared to the forward estimation scheme of the EKF where drastic approximations are necessary to keep the implementation practical. Furthermore, the model gradient may be used in a number of analyzes such as optimization of observation networks (see the work of Daescu and Carmichael, 2010; Frazier et al., 2009; Wu et al., 2007). For cases in which the model error is not only due to input uncertainties, the *weak constrained 4DVar* should be used (e.g. Fisher et al., 2005). In 4D-Var, the covariance matrix of the analysis is given by the Hessian of the final cost function (Courtier et al., 1994).

Despite the convenience of the adjoint method in data assimilation, the computational costs of its implementation in weather prediction was too high. As Courtier pointed out (Courtier et al., 1994), the computational cost of assimilating data for 24 hours was equivalent to the cost of four days of model integration; making the method too onerous for operational weather prediction. Courtier et al. (1994) would also provide the solution to the problem by advising to implement the data assimilation process using an incremental minimization strategy commonly known as *incremental 4DVar*. This method consist of two minimization processes referred to as outer loops. In the first outer loop, a low resolution model with simplified physics is used to produce

a preliminary analysis in low resolution. After the preliminary estimation is available, the second outer loop is used to further improve the quality of the analysis. In the second outer loop the physics are taken into account by using a linear approximation of a coarse physical model. The linearization is in fact a first order truncated Taylor expansion and it is commonly known as the *tangent linear model*. The tangent linear model provides the first order derivative of the full nonlinear model and it is used for the minimization of the cost function. The incremental 4DVar made the adjoint method practically feasible for implementation in models of considerable sizes. The incremental 4DVar is equivalent to an extended Kalman filter in which the time propagation of the forecast errors is done with the tangent linear model.

2.3 Particle filters

With the increase of computational power during the 80's, a new set of filtering techniques started to emerge during the beginning of the 1990s. These techniques exploited the flexibility and ease of implementation of Markov chain Monte Carlo (MCMC) methods. To the author's knowledge, the first to suggest its use was [Gordon et al. \(1993\)](#). The general idea behind the technique is to use a Markov Chain to propagate in time the probability distributions which are defined in terms of samples (ensemble members). For the estimation step, Bayes theorem is used to combine the information coming from the observations and the model. One of the main advantages of using the Bayesian approach is that it provides a rigorous general framework for state estimation problems. Particle filters (as they were named) are particularly appealing because they made no assumptions on the characteristics of the model, nor do they require a particular form of the probability distribution of the errors. Although the idea of using the MCMC methods in data assimilation had been considered before, a practical method for implementing Bayes theorem at the analysis step was still missing. [Gordon et al. \(1993\)](#) provided the solution to the problem by means of a recursive version of the *importance sampling Monte Carlo method* known as the *sequential importance sampling* (SIS).

Particle filters take advantage of the Monte Carlo method to model the evolution in time of the model error probability distribution. This probability distribution is described in terms of samples/particles. The reconstruction of the function is given by the following rule,

$$p(\mathbf{x}) = \frac{1}{n_s} \delta(\mathbf{x} - \mathbf{x}_k^i) \quad (2.10)$$

where \mathbf{x}_k^i is the value that the sample i takes at time k . The function $\delta(\cdot)$ is the delta Dirac function (delta function from now on) that is zero everywhere except at zero, with an integral of one over the entire real line. The cumulative probability function is therefore a step function. To account for the total number of samples, n_s , the delta function is scaled by $1/n_s$. The information about the evolution of the model error

probability distribution is given by the different trajectories of the ensemble members. These trajectories are governed by a Markov process such that,

$$p(\mathbf{x}_k^i) = p(\mathbf{x}_k^i | \mathbf{x}_{k-1}^i) p(\mathbf{x}_{k-1}^i | \mathbf{x}_{k-2}^i) \dots p(\mathbf{x}_1^i | \mathbf{x}_0^i) p(\mathbf{x}_0^i) \quad (2.11)$$

At the time of the analysis, Bayes' theorem is used to approximate the posterior probability distribution. The main advantage of the method is that it does not require knowledge on the complete form of the prior distribution. Instead, an *importance-weight* is assigned to each of the ensemble member that serves as a proxy for the probability density at its location. The analysis step is then defined as,

$$p(\mathbf{x}_k | \mathbf{y}_k) = \sum_{i=1}^{n_s} w_k^i \delta(\mathbf{x} - \mathbf{x}_k^i) \text{ with,} \quad (2.12)$$

$$w_k^i = \frac{p(\mathbf{y}_k | \mathbf{x}_k^i)}{\sum_{j=1}^{n_s} p(\mathbf{y}_k | \mathbf{x}_k^j)} \quad (2.13)$$

The term $p(\mathbf{y}_k | \mathbf{x}_k)$ represents the likelihood of the observation given the model result and in most cases it is assumed to follow a normal distribution,

$$p(\mathbf{y}_k | \mathbf{x}_k) = C \exp \left(-0.5 [h_k(\mathbf{x}_k, \boldsymbol{\alpha}_k) - \mathbf{y}]' \Sigma^{-1} [h_k(\mathbf{x}_k, \boldsymbol{\alpha}_k) - \mathbf{y}_i] \right).$$

The covariance matrix of the observation error is given by Σ . The way in which the importance weights change the probability distribution as data is assimilated is given by:

$$p(\mathbf{x}_k^i | \mathbf{y}_{0:k}) = w_k^i p(\mathbf{x}_k^i | \mathbf{x}_{k-1}^i) w_{k-1}^i p(\mathbf{x}_{k-1}^i | \mathbf{x}_{k-2}^i) \dots \\ \times w_1^i p(\mathbf{x}_1^i | \mathbf{x}_0^i) \left[\frac{1}{n_s} \delta(\mathbf{x} - \mathbf{x}_0^i) \right].$$

This equation shows the manner in which the state vector evolves in time and is updated as observations come. It also shows the main weakness of the particle filter. The problem arises when there is an observation that lies far away from one of the samples. In this case the importance weight will be very close to zero which causes the sample's probability from that point to be negligible. In this situation the sample will provide no information on the form of the probability distribution. Eventually, all but one sample will have negligible probability. The problem is unavoidable and pervasive to all applications. Even if the particles follow the observations in time, the weights will slowly diminish in all but one sample. This process is commonly called filter degeneracy. The problem has been alleviated with the development of resampling techniques. The most common and probably simplest resampling strategy is to make copies of samples that are getting higher weights and remove samples whose weights are below a certain threshold. Nevertheless, for high dimensional problems with several observations, they remain inapplicable.

More generally, the problem is that the number of samples required to infer the probability distribution accurately depends on the size of the state vector (dimensions of the space) and on how nonlinear the model is. In cases of nonlinear model dynamics with a considerable state space dimension, the number of particles necessary to accurately describe the evolution of the probability distribution in time is extremely high. This phenomenon is usually referred to as the *dimensionality curse*. From a practical point of view the implementation of an *assumption-free* particle filter is unattainable in most complex systems. From a theoretical point of view, on the other hand, a particle filter with infinite particles provides a formal mathematical solution to the problem of state estimation.

Shortly after the presentation of the particle filter by Gordon, Evensen (1994) proposed to use the Monte Carlo method in the framework of the Kalman filter. Since the propagation in time of the model error covariance matrix is computationally expensive, the idea is to use an ensemble of model runs to describe the evolution of uncertainties. The rest of the method steps are preserved as initially proposed by Kalman and Bucy.

The ensemble Kalman filter (EnKF) provides a working solution to the problem of filter degeneracy of particle filters, while taking advantage of their flexibility and ease of use. The temporal evolution of the model error probability distribution is given in terms of stochastic samples. The filter uses the same analysis rule of the Kalman filter and therefore requires the same assumptions; specifically, the model error at the time of the analysis is normally distributed with mean zero and known variance. Since the Monte Carlo sampling is only used to analyze the temporal change of the second order moment the required number of samples remains feasible. By using the Kalman equations for the analysis, the method completely avoids the use of the importance sampling technique. The moments are defined by:

$$\bar{\mathbf{x}}_k = \frac{1}{n_s} \sum_{i=1}^{n_s} \mathbf{x}_k^i, \quad (2.14)$$

$$P_k = \frac{1}{n_s - 1} \sum_{i=1}^{n_s} (\mathbf{x}_k^i - \bar{\mathbf{x}}_k)(\mathbf{x}_k^i - \bar{\mathbf{x}}_k)', \quad (2.15)$$

where $\bar{\mathbf{x}}_k$ is the ensemble mean and P_k is the model error covariance matrix at time k . With this information the Kalman gain is estimated (equation 2.6) and ultimately each ensemble member is updated following the Kalman analysis rule, equation 2.5.

After the seminal paper of Evensen (1994), a series of papers (Burgers et al., 1998; Houtekamer and Mitchell, 1998; Whitaker and Hamill, 2002) further developed the method and partially solved the problem of analysis covariance underestimation. The problem was related with the derivation of the analysis of the covariance matrix. Burgers et al. (1998) shows that the observations must be treated as random variables as well, and therefore random perturbations with the correct statistics should be added to them. Nevertheless, the correction to the algorithm is only asymptotically valid and

its implementation with few ensemble members generates problems related to sampling error, as [Whitaker and Hamill \(2002\)](#) remarks. To alleviate the problem, [Whitaker and Hamill \(2002\)](#) proposed a stochastic square root filter or advised to use the scheme proposed by [Pham \(2001\)](#). The stochastic square root filters are in fact an adaption of the square root filter implemented on the Kalman filter. The latter dates back to 1977 ([Maybeck, 1977](#)) and was design to avoid numerical issues with the implementation of the KF.

There are several variations of each of the data assimilation techniques that have been discussed here. Hybrid methods that try to exploit the strengths of two filtering techniques have been implemented for different applications. A non-exhaustive list of different techniques is given by [Ngodock et al. \(2006\)](#) in the introduction of their paper.

Chapter 3

Model reduced 4D-Var: Insight and updates

"The ability to simplify means to eliminate the unnecessary so that the necessary may speak." - Hans Hoffman (1880-1966, German painter)

One of the main limitations of adjoint based methods, such as variational schemes, is that the construction of the adjoint code is not straightforward for complex non-linear models. For a linear model, on the other hand, the adjoint model construction consists of a matrix transposition. From this perspective, the use of the tangent linear model has great potential. Unfortunately, for high dimensional dynamic models the implementation of the tangent linear model becomes unfeasible. Model order reduction makes a practical approximation of the tangent linear model by bringing together concepts of model linearization and principal components analysis. The outcome is a reduced rank tangent linear model that preserves the most important dynamic components of the non-linear model. The approximation of the model dynamics using a reduced order model (ROM) is convenient because it does not require to estimate the full model gradient (see section 3.3). In fact, the number of model executions required is proportional to the number of principal components of the dynamic system (which is chosen by the user) and the size of the input vector. This makes the expense of building a reduced order model affordable with current computational standards, even for highly dimensional problems.

The theory behind mr4DVar is presented here in three different sections. The theory behind model order reduction is shown in section 3.1. An alternative reduction procedure: *ensemble model order reduction*, is proposed in section 3.2. Finally, the way in which model order reduction and 4DVar are brought together in mr4DVar is shown in 3.3.

3.1 Model order reduction

The ROM presented here, consists of a linear approximation of a nonlinear model projected onto a reduced rank space. The linearization is done via a truncated Taylor expansion of the nonlinear model. The linearized approximation of the model is given by,

$$\delta \mathbf{x}_k = \frac{\partial \mathbf{x}_k}{\partial \mathbf{x}_{k-1}} \delta \mathbf{x}_{k-1} + \frac{\partial \mathbf{x}_k}{\partial \boldsymbol{\alpha}_{k-1}} \delta \boldsymbol{\alpha}_{k-1} \quad (3.1)$$

with $\delta \mathbf{x}_{k-1}$ and $\delta \boldsymbol{\alpha}_{k-1}$ being changes in the state and parameters, respectively, at time t_{k-1} ($k \in \mathbb{N}$). The term $\mathbf{x}_k \in \mathbb{R}^n$ is the state vector and $\boldsymbol{\alpha}_k \in \mathbb{R}^m$, is the input vector at time t_k . The truncated Taylor expansion gives an approximation of the changes in the model results (\mathbf{x}_k) due to changes in the model inputs, i.e. previous state (\mathbf{x}_{k-1}) and model parameters ($\boldsymbol{\alpha}_{k-1}$). As it turns out, this linear approximation (Eq. 3.1) is useful for fairly small problems (small sizes of \mathbf{x}_k). That is because the model derivative with respect to the previous state (first term of the right hand side) is in $\mathbb{R}^{n \times n}$ and its estimation is too expensive. To make the linearization useful for large models a projection into a low dimensional space is necessary,

$$P' \delta \mathbf{x}_k = P' \frac{\partial \mathbf{x}_k}{\partial \mathbf{x}_{k-1}} P P' \delta \mathbf{x}_{k-1} + P' \frac{\partial \mathbf{x}_k}{\partial \boldsymbol{\alpha}_{k-1}} \delta \boldsymbol{\alpha}_{k-1}, \quad (3.2)$$

where it is assumed that the projection matrix $P \in \mathbb{R}^{n \times n_p}$ has rank significantly smaller than n ($n_p \ll n$). By defining $\mathbf{r}_k = P' \delta \mathbf{x}_k$, equation 3.2 can be rewritten as a first order autoregressive model:

$$\mathbf{r}_k = P' \left\{ \left(\frac{\partial \mathbf{x}_k}{\partial \mathbf{x}_{k-1}} P \right) \mathbf{r}_{k-1} + \frac{\partial \mathbf{x}_k}{\partial \boldsymbol{\alpha}_{k-1}} \delta \boldsymbol{\alpha}_{k-1} \right\} \quad (3.3)$$

The first term in the right hand side of equation 3.3 is a Gateaux derivative (directional derivative) and each column i of this matrix is given by

$$\left\{ \frac{\partial \mathbf{x}_k}{\partial \mathbf{x}_{k-1}} P \right\}_i = \lim_{\epsilon \rightarrow 0} \frac{f_k(\mathbf{x}_{k-1} + \epsilon \hat{\mathbf{p}}_i, \boldsymbol{\alpha}_{k-1}) - f_k(\mathbf{x}_{k-1}, \boldsymbol{\alpha}_{k-1})}{\epsilon}$$

with vector $\hat{\mathbf{p}}_i$ being the i th column of matrix P and $x_k = f_k(\mathbf{x}_{k-1}, \boldsymbol{\alpha}_{k-1})$. Notice that the numerical approximation of the complete directional derivative only requires $2n_p + 1$ model simulations ($n_p \ll n$). This is a key component within the reduction process because it avoids estimating the full Jacobian, $\nabla_{\mathbf{x}_{k-1}} f_k(\mathbf{x}_{k-1}, \boldsymbol{\alpha}_{k-1}) \in \mathbb{R}^{n \times n}$. Since the number of parameters, n_α , is usually small, ordinary finite differences are used to estimate the second term, $\nabla_{\boldsymbol{\alpha}_{k-1}} f_k(\mathbf{x}_{k-1}, \boldsymbol{\alpha}_{k-1}) \in \mathbb{R}^{n \times n_\alpha}$, on the right hand side of equation 3.3.

The projection matrix, P , is estimated by means of a principal component analysis. The sub-space should preserve the most relevant features of the system making it necessary to study the model behavior with respect to the model parameters of interest.

An ensemble of model simulations with at least $n_\alpha + 1$ members is executed to span the full parameter space. The ensemble consists of a *reference simulation* (also known as *background*) with the initial set of parameters, and a set of perturbed-parameter model simulations. State vectors from each ensemble member are stored at a number of times, n_t , and the difference between the *perturbed* and the *reference simulation* is computed, $f_k(\mathbf{x}_{k-1}, \boldsymbol{\alpha}_{k-1} + \Delta\boldsymbol{\alpha}_{k-1}) - f_k(\mathbf{x}_{k-1}, \boldsymbol{\alpha}_{k-1})$. Each of these vectors is commonly known as a snapshot. The $n_\alpha \times n_t$ snapshots of each perturbed model integration are assembled into a *snapshot matrix* of $n_\alpha \times n_t$ columns by n rows. Solving a singular value decomposition (SVD) on this matrix produces a set of orthonormal vectors from which n_p are chosen to span the sub-space of interest. The number of relevant singular vectors is expected to be much smaller than the length of the state vector.

The following steps are necessary for its implementation:

1. Run the model with an initial guess of the parameter values (*background*).
2. Run an ensemble of n_α mutually-independent perturbed-parameter simulations.
3. Subtract the background from each of the ensemble members and build the snapshot matrix.
4. Get the principal components by solving a SVD on the snapshot matrix.
5. Make a first order Taylor expansion of the model and project it on the subspace spanned by the principal modes (eq. 3.3), i.e. compute the directional derivatives for each column in the projection matrix and the finite differences for each input parameter.

Steps 1 and 2 imply $n_\alpha + 1$ simulations of the system and step 5 implies an extra $n_p + n_\alpha$ model simulations, where n_p is the number of principal modes. Nonetheless, the simulations involved in steps 1 and 2 can be carried out in parallel and, subsequently, all the simulations involved in step 5 can also be run in parallel. Hence the cost of the technique is relative to the availability of processors, which nowadays is generally not an issue.

3.2 Ensemble Model Order Reduction: An alternative method

Here a novel model order reduction technique that avoids the use of finite differences is presented. One of the main drawbacks when using the traditional model order reduction method presented in section 3.1, is that sometimes the estimation of derivatives via finite-differences is difficult. The *Ensemble model order reduction* (EnMOR) method presented in this section uses the ensemble of simulations used for estimating the projection matrix to determine the different components of the ROM. The process

only requires enough ensemble members to properly constrain a least squares estimation of the unknown components. EnMOR not only avoids to run perturbed model simulations but also avoids restarting the model.

Although most numerical models have a restarting procedure available, in some cases it has undesirable effects in the state evolution (see, for example, section 4.3). Commonly these effects are caused by loss of information during the restarting process. Consequently, the derivatives at different simulation times cannot be estimated or they are inaccurate. In the case of the Gateaux derivative, on the other hand, the required perturbation may cause numerical problems. For models based on the mass and momentum conservation laws, perturbing the model state frequently leads to model instabilities. This is mainly due to the characteristics of the perturbed run required for estimating the Gateaux derivative,

$$\lim_{\epsilon \rightarrow 0} \frac{f_k(\mathbf{x}_k + \epsilon \hat{p}, \boldsymbol{\alpha}_{k-1}) - f_k(\mathbf{x}_k, \boldsymbol{\alpha}_{k-1})}{\epsilon}.$$

In order to make a successful estimation of the directional derivative required in the method, delicate analysis and processing of the perturbation is necessary. In some cases, the efforts to minimize undesirable effects and maintain the accuracy of the result are considerable. Aside from the numerical issues, the size of each parameter perturbation for the finite-difference estimation demands a detailed analysis. Perturbations should be big enough to limit the effects of numerical errors but small enough not to include system's non-linearities in the calculation. All in all, the finite difference based model order reduction requires in-depth knowledge about the model behavior prior to its implementation.

Before getting into detail, a summary of the relevant dimensions is presented:

- n : state vector size,
- n_α : number of input parameters,
- n_e : number of ensemble members,
- n_t : number of ROM steps (number of piece-wise linearizations),
- n_p : rank of the reduced space (number of principal modes).

Also, let the ROM (eq. 3.3) be re-written in the following manner:

$$\mathbf{r}_k = D_k P' \delta \mathbf{x}_{k-1} + S_k \delta \boldsymbol{\alpha}_{k-1}, \quad (3.4)$$

where,

$$D_k = P' \frac{\partial \mathbf{x}_k}{\partial \mathbf{x}_{k-1}} P,$$

$$S_k = P' \frac{\partial \mathbf{x}_k}{\partial \boldsymbol{\alpha}_{k-1}}.$$

D_k represents the dynamic component of the model and S_k stands for the projected sensitivities of the model to the input parameters. The terms $\delta \mathbf{x}_{k-1}$ and $\delta \alpha_{k-1}$ are changes with respect to the background (linearization of the trajectory), in the state vector and parameters, respectively, at time t_{k-1} .

The objective function used to estimate the ROM's components is the sum of the square differences between the ROM results and the projected ensemble runs for each ensemble member i , \mathbf{x}_k^i , at each reduced order model step, k ,

$$\min_{arg D_k, S_k} J_{\text{ROM}} = \sum_{i=1}^{n_e} \sum_{k=1}^{n_t} \frac{1}{2} [\mathbf{r}_k^i - P' \delta \mathbf{x}_k^i]' [\mathbf{r}_k^i - P' \delta \mathbf{x}_k^i]. \quad (3.5)$$

The required *training information* for the optimization process is coming from the model ensemble. The term \mathbf{r}_k^i is a ROM integration where the same perturbations used to produce the i th ensemble member were used. The arguments of the minimization problem are the ROM components, D_k and S_k . Given the size of the problem, $n_t \times (n_p^2 + n_p \times n_\alpha)$, a gradient based minimization scheme is preferable to minimize the computational expenses. Since the arguments of the problem are matrices, the estimation of the gradient is not straightforward. To show how to calculate it, consider the following product:

$$z = (ABC\mathbf{u} - \mathbf{v})'(ABC\mathbf{u} - \mathbf{v}), \quad (3.6)$$

We are interested in estimating the derivative of z with respect to $vec(B)$, where $vec(\cdot)$ is the vectorization operator. The vectorization operator stacks the columns of the $m \times n$ matrix B on top of one another to produce an $mn \times 1$ vector $vec(B)$. It can be shown that,

$$vec(ABC) = (C' \otimes A)vec(B), \quad (3.7)$$

where the operator \otimes represents the Kronecker product and C' is the transpose of C . If C is a $u \times v$ matrix and A is a $p \times q$ matrix, the Kronecker product is the $up \times vq$ block matrix given by,

$$C' \otimes A = \begin{bmatrix} c_{11}A & \cdots & c_{u1}A \\ \vdots & \ddots & \vdots \\ c_{1v}A & \cdots & c_{vu}A \end{bmatrix},$$

where c_{ij} is the i, j element of matrix C .

Using equation 3.7 and the fact that the vectorization of a column vector is equal to the vector, the calculation of the derivative mentioned before is straightforward and is given by,

$$\begin{aligned} \frac{\partial z}{\partial vec(B)} &= 2 \left[\frac{\partial}{\partial vec(B)} ABC\mathbf{u} \right]' (ABC\mathbf{u} - \mathbf{v}) \\ &= 2 \left[\frac{\partial}{\partial vec(B)} vec(ABC\mathbf{u}) \right]' (ABC\mathbf{u} - \mathbf{v}), \end{aligned}$$

and,

$$\frac{\partial}{\partial \text{vec}(B)} \text{vec}(ABC\mathbf{u}) = [\mathbf{u}'C' \otimes A]. \quad (3.8)$$

Equation 3.7 can be used again to rewrite the result in a more convenient form:

$$\begin{aligned} \frac{\partial z}{\partial \text{vec}(B)} &= 2 [C\mathbf{u} \otimes A'] (ABC\mathbf{u} - \mathbf{v}) \\ &= 2 \text{vec}(A' [ABC\mathbf{u} - \mathbf{v}] \mathbf{u}'C'). \end{aligned} \quad (3.9)$$

The estimation of the Hessian is also straightforward,

$$\begin{aligned} \frac{\partial^2 z}{\partial \text{vec}(B)^2} &= 2 \frac{\partial}{\partial \text{vec}(B)} [C\mathbf{u} \otimes A'] (ABC\mathbf{u} - \mathbf{v}) \\ &= 2 \frac{\partial}{\partial \text{vec}(B)} [C\mathbf{u} \otimes A'] (\mathbf{u}'C' \otimes A) \text{vec}(B) \\ &= 2 [C\mathbf{u} \otimes A'] [\mathbf{u}'C' \otimes A] \\ &= 2 [C\mathbf{u}\mathbf{u}'C' \otimes A'A]. \end{aligned} \quad (3.10)$$

$$(3.11)$$

These results are very useful in the context of the estimation problem of interest. If the recursion defined by the ROM (eq. 3.4) is resolved, the objective function (eq. 3.5) is of the same form as equation 3.6; and the derivative and the Hessian of the cost function are defined by,

$$\frac{\partial J_{ROM}}{\partial \text{vec}(D_j)} = \sum_{i=1}^{n_e} \sum_{k=1}^{n_t} \left[\frac{\partial \mathbf{r}_k^i}{\partial \text{vec}(D_j)} \right]' [\mathbf{r}_k^i - P' \delta \mathbf{x}_k^i], \quad \forall j \leq k; j \in \mathbb{N}, \quad (3.12)$$

and

$$\begin{aligned} \frac{\partial^2 J_{ROM}}{\partial \text{vec}(D_j) \partial \text{vec}(D_l)} &= \sum_{i=1}^{n_e} \sum_{k=1}^{n_t} \left[\frac{\partial^2 \mathbf{r}_k^i}{\partial \text{vec}(D_j) \partial \text{vec}(D_l)} \right]' [\mathbf{r}_k^i - P' \delta \mathbf{x}_k^i] \\ &+ \left[\frac{\partial \mathbf{r}_k^i}{\partial \text{vec}(D_j)} \right]' \left[\frac{\partial \mathbf{r}_k^i}{\partial \text{vec}(D_l)} \right]', \quad \forall j, l \leq k; j, l \in \mathbb{N} \end{aligned} \quad (3.13)$$

respectively. The derivative of the ROM with respect to the dynamic component (D_j) is estimated by using equation 3.8. The estimation of the derivative with respect to the sensitivity components (S_j) is done analogously.

As an example, consider the cost function term corresponding to the following reduced order model estimation,

$$\mathbf{r}_3 = D_3 D_2 D_1 \mathbf{r}_0^i + D_3 D_2 S_1 \delta \alpha_0^i + D_3 S_2 \delta \alpha_1^i + S_3 \delta \alpha_2^i, \quad (3.14)$$

where the parameter perturbation at time t_{k-1} used for the i th ensemble member is given by α_{k-1}^i and the initial state perturbation for the i th ensemble member is given

by $\mathbf{r}_0^i = P' \delta \mathbf{x}_0^i$. We are interested in computing the derivative with respect to D_2 of the cost defined by,

$$J_{ROM} = \frac{1}{2} [\mathbf{r}_3^i - P' \delta \mathbf{x}_3^i]' [\mathbf{r}_3^i - P' \delta \mathbf{x}_3^i]$$

where $\delta \mathbf{x}_3^i$ is the difference between the ensemble member state and the background state at time t_3 . This derivative is given by,

$$\frac{\partial \mathbf{r}_3^i}{\partial \text{vec}(D_2)} = \text{vec}(D_3' [P' \delta \mathbf{x}_3^i - \mathbf{r}_3^i] (D_1 P' \delta \mathbf{x}_0^i)' + D_3' [P' \delta \mathbf{x}_3^i - \mathbf{r}_3^i] (S_1 \delta \alpha_{k-1}^i)').$$

The second order derivative is given by,

$$\begin{aligned} \frac{\partial^2 \mathbf{r}_3^i}{\partial \text{vec}(D_2)^2} &= D_1 P' \delta \mathbf{x}_0^i (D_1 P' \delta \mathbf{x}_0^i)' \otimes D_3' D_3 + S_1 \delta \alpha_{k-1}^i (S_1 \delta \alpha_{k-1}^i)' \otimes D_3' D_3 \\ &= [D_1 P' \delta \mathbf{x}_0^i (D_1 P' \delta \mathbf{x}_0^i)' + S_1 \delta \alpha_{k-1}^i (S_1 \delta \alpha_{k-1}^i)'] \otimes D_3' D_3. \end{aligned}$$

In this form each of the terms of the summations in the cost function (equation 3.5) can be differentiated with respect to each of the ROM's components.

As it is presented, equation 3.5 is weighing all *training observations* equally. This could be changed by inserting a weighing matrix that assigns more importance (weight) to areas of the state vector of particular interest. Such implementation would produce a ROM specialized in reconstructing specific areas of the full nonlinear model. In applications where modeling errors are spatially dependent, the ability to emphasize the importance of certain regions in the construction of the ROM is very useful. In this case the estimation problem (equation 3.5) would be given by,

$$\min_{\arg D_k, S_k} J_{ROM} = \sum_{i=1}^{ne} \sum_{k=1}^{nt} \frac{1}{2} [\mathbf{r}_k^i - P' \delta \mathbf{x}_k^i]' Q^{-1} [\mathbf{r}_k^i - P' \delta \mathbf{x}_k^i], \quad (3.15)$$

where Q is a symmetric positive definite matrix. In data assimilation this matrix is usually the error covariance matrix of the *training information*; thus, the model error covariance matrix.

From a computational point of view, the use of the Hessian might speed up the estimation process. Given the eigenvalue decomposition of the matrices $A'A = Q_A \Lambda_A Q_A'$ and $Cuu'C' = Q_{uC} \Lambda_{uC} Q_{uC}'$ the eigenvalue decomposition of the Hessian matrix (eq. 3.11) is given by,

$$\begin{aligned} \text{EIG}(Cuu'C' \otimes A'A) &= Q_{uC} \Lambda_{uC} Q_{uC}' \otimes Q_A \Lambda_A Q_A', \\ &= (Q_{uC} \otimes Q_A) (\Lambda_{uC} \otimes \Lambda_A) (Q_{uC} \otimes Q_A'). \end{aligned} \quad (3.16)$$

It is not necessary to have the Hessian matrix to estimate its eigenvalue decomposition (see theorem 13.10 in Laub, 2005, page 141). If the principal components of the much smaller matrices $A'A$ and $Cuu'C'$ are available, the principal components of

the Hessian can be calculated exactly and are given by equation 3.16. Significant computational savings can be achieved by using only the leading modes of matrix A in the computation.

From an implementation perspective, the scheme presented here differs considerably from the finite difference based approach of model order reduction. The scheme completely avoids the use of finite differences to estimate the ROM components. Instead it relies on a model ensemble to gather the necessary information to construct the ROM. This is advantageous when working with models that do not have a restarting functionality, or where the state and parameter perturbation is not straightforward. The estimation process replaces the finite differences estimation by the minimization of a quadratic cost function defined by equation 3.5. The size of the problem depends on the number of simulated times, n_t , the size of the input vector, n_α , and the size of the projection subspace, n_p , and is given by $n_t \times (n_p^2 + n_p \times n_\alpha)$. Given the form of the ROM, the gradient and the Hessian of the cost function with respect to the ROM's components are defined by equations 3.9 and 3.11. Using the Hessian of the objective function in the minimization process produces a rate of convergence at least quadratic, and for high dimensional problems this is very useful because it offers significant efficiency improvements. In cases where the Hessian matrix is singular, adding a background term in the definition of the cost function may be advisable. The definition of the singular value decomposition of a Kronecker product (eq. 3.16) offers interesting advantages for the approximation of the cost's Hessian. Finally, the model ensemble provides additional information that is unavailable when the model executions are intended for finite differences estimation. Given appropriate perturbations, the ensemble could be used to estimate the temporal evolution of the model uncertainty.

The implementation of the scheme proposed here involves the following steps:

1. run a model ensemble with the appropriate state and input vector error properties,
2. assume an initial set of ROM components: D_k and S_k , zero matrices for instance,
3. compute the cost function (eq. 3.5), which compares the ROM results with each ensemble member, and
4. start a gradient-based minimization process on the cost function, using the gradient (eq. 3.9) and, if necessary, the Hessian (eq. 3.11).

3.3 Model Reduced 4D-Var

In model reduced 4DVar a ROM is constructed by means of a principal components analysis (PCA) as described previously. Its linearity both in state vector and parame-

ters, facilitates considerably the use of data assimilation. By introducing equation 3.3 in the cost function (equation 2.8), the problem can be written as:

$$J(\delta\alpha_1, \dots, \delta\alpha_{l-1}) = \frac{1}{2} \sum_{k=1}^l \delta\alpha'_{k-1} B_k^{-1} \delta\alpha_{k-1} + \frac{1}{2} \sum_{k=1}^l (H_k P \mathbf{r}_k - \hat{y}_k)' R_k^{-1} (H_k P \mathbf{r}_k - \hat{y}_k) \quad (3.17)$$

and its derivative with respect to $\delta\alpha_{k-2}$, for instance, is given by

$$\begin{aligned} \nabla_{\delta\alpha_{k-2}} J &= B^{-1} \delta\alpha_{k-2} + \left[\frac{\partial \mathbf{r}_k}{\partial \alpha_{k-2}} \right]' P' H'_k R_k^{-1} (H_k \mathbf{x}_k - \hat{y}_k), \\ &= B^{-1} \delta\alpha_{k-2} + [D_k S_{k-1}]' P' H'_k R_k^{-1} (H_k \mathbf{x}_k - \hat{y}_k). \end{aligned}$$

This minimization problem is fast to solve, but the update is sub-optimal. The two main reasons for this are that (1) the ROM is accurate only in the vicinity of the prior parameter set and (2) only a part of the full parameter space is available. If the update is not within the threshold of validity of the ROM, a new ROM that is closer to the true state is required.

Due to the properties of the technique, the modeler has a lot of freedom to implement and run the data assimilation procedure. The main objective is to find the optimal parameter set; the challenge is to do it in a cost efficient manner. To optimize the performance of each iteration, the modeler can rely on increasing the quality of the ROM by fine tuning its construction. For example, by generating more snapshots or by increasing the number of modes in the projection sub-space, more information about the model behavior is captured by the ROM. Or, by using second order estimates (central differences) the approximation of dynamic components and the sensitivities are expected to be more accurate (if using the finite difference approach). Nevertheless, these strategies usually come at the cost of more model simulations.

In *model reduced 4D-Var*, the ROM's main task is to provide the direction of greatest descent to the optimization procedure. It has been developed to avoid the construction of the adjoint model. The concept of "quality" of the ROM is no longer focused on its capacity to reconstruct quantitatively the evolution of the state vector; instead, it should be able to identify the direction in which the state vector should be updated due to changes in model parameters.

The implementation of model reduced 4DVar involves the following steps:

1. Implement a reduced order model of the nonlinear model of interest.
2. Build the adjoint model of the reduced order model.
3. Implement 4DVar assimilation to optimize the parameters of interest by minimizing equation 3.17.

4. Run the full model with the analysis.
5. Assess whether the update satisfies the expected accuracy. If not, take the current model update for a background run and repeat the process.

Chapter 4

Wave-Flow-Morphodynamic modeling

" So long as the volume of matter to be dealt with in science was insignificant, the need for the employment of models was naturally less imperative; ... Yet as the facts of science increased in number, the greatest economy of effort had to be observed in comprehending them and in conveying them to others; and the firm establishment of ocular demonstration was inevitable in view of its enormous superiority over purely abstract symbolism for the rapid and complete exhibition of complicated relations. (Boltzmann, 1974, page 215)

Coastal morphodynamic evolution the result of several natural processes that interact with each other. Generally, the sources of energy that drive morphodynamic changes are climatic (e.g. wave and wind) and astronomic (moon and sun gravitational fields), whereas the geomorphological properties of the system determine to a great extent the way in which the morphodynamic changes happen. Regarding the modeling of coastal systems, the mass continuity and conservation of momentum equations are the keystones of the hydrodynamic model; while for sediment transport the advection-diffusion equation is commonly used (Waeles et al., 2007; van Ledden, 2003, see,). A thorough review of the physical background of sediment transport processes may be found in van Rijn (2007a,b,c); van Rijn et al. (2007). In most cases no closed form solution of these equations is available and a numerical approximation of them is necessary. The numerical method plays a determining role in the approximation of the morphodynamic evolution. There are several numerical methods for solving systems of differential equations; each one with various advantages and disadvantages.

This chapter is part of:

I. Garcia, G. Serafy, A. Heemink, and H. Schuttelaars. Towards a data assimilation system for morphodynamic modeling: bathymetric data assimilation for wave property estimation. *Ocean Dynamics*, pages 1–17, 2013.

Each of these methods requires some level of parameterization, and thus, there are model parameters of physical nature and of numerical nature both playing an equally important role in the simulation outcome.

4.1 Swan and Delft3D-MOR Description

The Delft3D suite is used to implement all the experiments presented here. This model has two different modules that interact with each other during the morphodynamic simulation: (1) a wave module and (2) a flow and morphology module. Delft3D-SWAN, the wave module, is a numerical model for estimating wave parameters for stationary wind, bottom, and current conditions (Deltares, 2009b). Delft3D-FLOW, the flow and morphology module, calculates non-steady flow, sediment transport and the bed evolution resulting from tidal and meteorological forcings (Deltares, 2009a). Here a brief description of the modules is presented. For a detailed description of the model, the reader is referred to Deltares (2009a,b); Lesser et al. (2004).

4.1.1 Waves Module

The wave module, *SWAN*, computes the wave propagation, the breaking and the radiation stresses by solving the two dimensional wave action density spectrum, $N(\sigma, \theta)$, which is governed by the action balance equation,

$$\frac{\partial N}{\partial t} + \frac{\partial c_x N}{\partial x} + \frac{\partial c_y N}{\partial y} + \frac{\partial c_\sigma N}{\partial \sigma} + \frac{\partial c_\theta N}{\partial \theta} = \frac{S}{\sigma}. \quad (4.1)$$

The action density spectrum is related to the energy density spectrum through $N(\sigma, \theta) = E(\sigma, \theta)/\sigma$, where σ is the relative radian frequency and θ is the wave direction. The terms c_σ and c_θ are the propagation velocities in spectral space (σ, θ) , and c_x and c_y stand for the propagation velocities in Cartesian space. S represents the source term expressed as energy density and may take into account generation by wind, dissipation by whitecapping, bottom friction, depth-induced breaking and non-linear wave-wave interactions.

4.1.2 Hydrodynamic Module

The hydrodynamic fluid motion is governed by the conservation of momentum equation and the continuity equation. For systems where the horizontal length scales are considerably larger than the water depth, the momentum and mass conservation equations can be simplified to produce the shallow water equations. In this case, the continuity equation is given by,

$$\frac{\partial u}{\partial x} + \frac{\partial v}{\partial y} + \frac{\partial w}{\partial z} = 0. \quad (4.2)$$

where ζ is the water level with respect to the water depth at still water conditions, h . The velocity components in the x , y and z directions are given by u , v and w , respectively. The term Q is the total addition or subtraction of water per unit area due to precipitation, evaporation, etc. The equations for momentum conservation are:

$$\frac{\partial u}{\partial t} + u \frac{\partial u}{\partial x} + v \frac{\partial u}{\partial y} + w \frac{\partial u}{\partial z} - fv = -\frac{1}{\rho} \frac{\partial P}{\partial x} + F_x + M_x + \frac{\partial}{\partial z} \left(\nu_v \frac{\partial u}{\partial z} \right) \quad (4.3)$$

$$\frac{\partial v}{\partial t} + u \frac{\partial v}{\partial x} + v \frac{\partial v}{\partial y} + w \frac{\partial v}{\partial z} + fu = -\frac{1}{\rho} \frac{\partial P}{\partial y} + F_y + M_y + \frac{\partial}{\partial z} \left(\nu_v \frac{\partial v}{\partial z} \right) \quad (4.4)$$

where F_x and F_y are the horizontal Reynold's stresses and momentum sources and sinks are given by M_x and M_y . The vertical eddy viscosity is given by $\nu_v = \nu + \max(\nu_v^{min}, \nu_{3D})$, where ν is the kinematic viscosity, ν_v^{min} is the minimum vertical eddy viscosity (user defined), and ν_{3D} is the three-dimensional turbulence (coming from the turbulence model). The water density is given by ρ , and f is the Coriolis parameter that depends on the geographic latitude of the earth. For the case of constant water density the pressure term, P , consists of the hydrostatic pressure and the atmospheric pressure, i.e.

$$P = \rho g(\zeta - z) + P_{atm}. \quad (4.5)$$

The horizontal Reynold's stresses are given by,

$$F_x = \frac{\partial \tau_{xx}}{\partial x} + \frac{\partial \tau_{xy}}{\partial y} \quad (4.6)$$

$$F_y = \frac{\partial \tau_{yx}}{\partial x} + \frac{\partial \tau_{yy}}{\partial y} \quad (4.7)$$

with the shear stresses defined as:

$$\tau_{xx} = 2\nu_h \left(\frac{\partial u}{\partial x} + \frac{\partial u}{\partial z} \right), \quad (4.8)$$

$$\tau_{xy} = \tau_{yx} = \nu_h \left[\frac{\partial u}{\partial y} + \frac{\partial u}{\partial z} + \frac{\partial v}{\partial x} + \frac{\partial v}{\partial z} \right], \quad (4.9)$$

$$\tau_{yy} = 2\nu_h \left(\frac{\partial v}{\partial y} + \frac{\partial v}{\partial z} \right). \quad (4.10)$$

Delft3D implements a half implicit half explicit numerical method over a staggered grid for solving the system of differential equations presented here. In the vertical direction, a so called sigma layer (σ -layer) approach is used to minimize the problems associated to significant changes in water depths common in certain natural systems (e.g. coastal systems). The numerical solution of the momentum and continuity equations as implemented in Delft3D is described in detail by Lesser et al. (2004). The computation of the vertical velocities in Delft3D is only required for post-processing purposes and they are computed from the continuity equation Deltares (2009a).

4.1.3 Morphodynamic Module

The morphodynamic module implements a numerical solution to the set of differential equations that govern transport sediment due to hydrodynamic forcing. Because of the significant differences in the physical processes governing suspended sediment transport and bed-load transport, different mathematical descriptions are given for each. The equation that describes the transport of suspended sediment is the conservation of sediment mass equation,

$$\frac{\partial c}{\partial t} + \nabla \cdot \mathbf{f} = Q_s, \text{ with} \quad (4.11)$$

$$\mathbf{f} = \mathbf{f}_a + \mathbf{f}_s + \mathbf{f}_d, \text{ and, } \nabla = \frac{\partial}{\partial x} \mathbf{i} + \frac{\partial}{\partial y} \mathbf{j} + \frac{\partial}{\partial z} \mathbf{k}.$$

where \mathbf{i} , \mathbf{j} , and \mathbf{k} are unitary vectors pointing in the x , y , and z directions, respectively. The sediment concentration is given by c , sources and sinks of sediment are given by Q_s (e.g. river discharges), and \mathbf{f} is the total sediment flux consisting of three components: the advective flux, \mathbf{f}_a ; the settling flux \mathbf{f}_s ; and the diffusive flux, \mathbf{f}_d . The three sediment fluxes are given by:

$$\mathbf{f}_a = c(u\mathbf{i} + v\mathbf{j} + w\mathbf{k}), \quad (4.12)$$

$$\mathbf{f}_s = -cw_s\mathbf{k}, \quad (4.13)$$

$$\mathbf{f}_d = -\kappa_h \left(\frac{\partial c}{\partial x} \mathbf{i} + \frac{\partial c}{\partial y} \mathbf{j} \right) - \kappa_v \frac{\partial c}{\partial z} \mathbf{k}. \quad (4.14)$$

Here the sediment settling velocity is represented by w_s , and the horizontal and vertical eddy diffusion coefficients are given by κ_h and κ_v , respectively. The settling velocity for non-cohesive sediment is a property of the sediment particles and in Delft3D is defined as:

$$w_s = \frac{(\rho_s/\rho - 1)gd_{50}^2}{18\nu}, \quad 65\mu\text{m} < d_{50} \leq 100\mu\text{m},$$

$$w_s = \frac{10\nu}{d_{50}} \left[\left(1 + \frac{0.001(\rho_s/\rho - 1)gd_{50}^3}{\nu^2} \right)^{0.5} - 1 \right], \quad 100\mu\text{m} < d_{50} \leq 1000\mu\text{m},$$

$$w_s = 1.1 [(\rho_s/\rho - 1)gd_{50}]^{0.5}, \quad 1000\mu\text{m} < d_{50},$$

where ρ_s is the density of the sediment, d_{50} is the sediment grain size and ν is the kinematic viscosity of the water. The eddy coefficients, on the other hand, are user defined parameters. For erodible boundaries, e.g. the bed, the boundary condition is given by:

$$-[\mathbf{f}_s + \mathbf{f}_d] \cdot \mathbf{n} = S_*, \quad (4.15)$$

where \mathbf{n} is a unitary vector perpendicular to boundary, and the erosion/deposition flux at the bed, S_* , is given by,

$$S_* = w_s c_a - w_s c_0, \quad (4.16)$$

with c_0 the sediment concentration at the bottom. The reference concentration, c_a , depends on the prevailing flow conditions and is defined as the concentration at the reference height, a . The reference height depends on the bed roughness, and is defined as one half of the bed form height (van Rijn, 1993). There are several formulations for the reference concentration which usually define it as a power law of the relation between the magnitude of the bed shear stress, τ , and magnitude of the bed critical shear stress, τ_c . For the case of non erodible boundaries the boundary condition is given by,

$$-[\mathbf{f}_s + \mathbf{f}_d] \cdot \mathbf{n} = 0. \quad (4.17)$$

In Delft3D the reference concentration is given by van Rijn (2007b),

$$c_a = 0.015\rho_s \frac{dT_a^{1.5}}{aD^{0.3}}, \quad (4.18)$$

where a is the reference level and with

$$T_a = \frac{\tau - \tau_c}{\tau_c}, \quad (4.19)$$

$$D = d_{50} \left[\frac{g(\rho_s/\rho - 1)}{\nu^2} \right]^{1/3}. \quad (4.20)$$

The bed load transport (s_b) formulation is independent of the transport equation 4.11. The governing equation is given by,

$$s_b = 0.006\rho_s w_s d_{50} M^{0.5} M_e^{0.7} \quad (4.21)$$

where

$$M = \frac{V_H^2}{gd_{50}(\rho_s/\rho - 1)}, \quad (4.22)$$

$$M_e = \frac{(V_H - V_c)^2}{gd_{50}(\rho_s/\rho - 1)}, \quad (4.23)$$

Here V_H stands for the magnitude of the horizontal velocity, V_c is the critical flow velocity for initiation of motion and is based on a parameterization of the Shields curve.

The wave related suspended transport is modeled as,

$$s_w = 0.007\rho_s d_{50} M \gamma \left[\frac{U_{on}^4 - U_{off}^4}{U_{on}^3 - U_{off}^3} \right], \quad (4.24)$$

where γ is the wave phase lag coefficient, and U_{on} and U_{off} are the high frequency, near orbital velocities due to short waves (Lesser et al., 2004). As implemented in Delft3D, the wave related suspended transport is included in the total bed load

Parameter Name	Delft3D Acronym
Chezy coefficient in U-direction	Ccofu
Chezy coefficient in V-direction	Ccofv
Horizontal eddy viscosity	Vicouv
Minimum depth for drying and flooding	Dryflc
Vertical eddy viscosity	Vicoww
Wave breaking index	Gamdiss
Roller front slope	Betaro
Roller breaker delay	F_{lam}

Table 4.1: Notable hydrodynamic parameters

transport vector. The direction of the bed load transport is given by the current direction whereas the direction of the wave-related transport is given by the direction of the orbital velocities.

The bed evolution, as implemented in Delft3D, is computed by solving the following equation:

$$(1 - \phi) \frac{\partial h}{\partial t} + \frac{1}{\rho_s} \left[\frac{\partial S_b}{\partial x} + \frac{\partial S_b}{\partial y} \right] = \frac{1}{\rho_s} S_* \quad (4.25)$$

$$(4.26)$$

where ϕ is the sediment fraction porosity.

4.2 Delft3D Parameters

Each module of Delft3D has a set of parameters that will directly/indirectly affect the morphodynamic estimations. Due to the numerical solution of the differential equations the relevant parameters are both physical and numerical in nature. Consequently, there is a large number of parameters that influences the modeling process significantly. In the following the set of parameters relevant to this work is discussed. The set includes those parameters that control the morphodynamic evolution of the model. The selection of it was based on expert judgment.

The hydrodynamic evolution is a key component in any morphodynamic model. It provides the information about flow properties required for sediment transport and wave estimation. Table 4.1 presents the set of relevant hydrodynamic parameters. In Delft3D, the roller model parameterization is given in the flow input file (see table 4.1) and consists of the following parameters: wave breaking index, roller front slope, and roller breaker delay (flow [Deltares, 2009a](#)). The roller model is of particular interest to the work presented here because it links the morphodynamic evolution with time exposure images such as the ones coming from the Argus system (see [Holman and Stanley, 2007](#)). The minimum depth for drying and flooding defines the system's

Parameter Name	Delft3D Acronym
Wave significant height	WaveHeight
Wave peak period	Period
Wave direction of incidence	Direction
Wave directional spreading	DirSpreading

Table 4.2: Notable wave parameters

Parameter Name	Delft3D Acronym
Horizontal eddy diffusivity	Dicouv
Vertical eddy diffusivity	Dicoww
Van Rijn's reference height factor	Aksfac
Wave related roughness parameter	Rwave
Streamwise bed gradient factor (bed load)	AlfaBs
Transverse bed gradient factor (bed load)	AlfaBn
Factor for suspended sediment ref. concentration	Sus
Factor for bed-load transport vector magnitude	Bed
Wave suspended sed. transport factor	SusW
Wave bed-load sed. transport factor	BedW
Factor for erosion of adjacent dry cells	ThetSD

Table 4.3: Notable morphodynamic parameters

shoreline and prevents numerical issues arising in extremely shallow areas. As in the case of the roller model, observations of the shoreline evolution in time are a potential source of information as it may be computed from time exposure images as well.

Since the waves are the main driving force of the morphodynamic evolution in the surf zone, these parameters are expected to have a considerable impact on the model results. In fact, the rip channel's evolution and dynamic behavior depend mainly on wave properties and initial bathymetry (Smit et al., 2007, 2008). Table 4.2 shows the set of most relevant (to this research) wave parameters in Delft3D. From the morphodynamic module, on the other hand, a set of 9 parameters are considered relevant, and they are presented in table 4.3. From this set of parameters, it is worth highlighting the importance of the wave-related suspended sediment transport factor and the wave-related bed-load sediment transport factor; which are multiplicative factors that decrease the sediment transport due to the presence of waves. Notice that all of them are numerical parameters. Furthermore, both sediment transport factors are designed to reduce model biases associated to the unresolved nonlinearities of the wave breaking model. According to experts, for 3D models the estimated sediment transport values should be decreased by approximately 30% and in the case of 2D models reductions of up to 90% are expected.

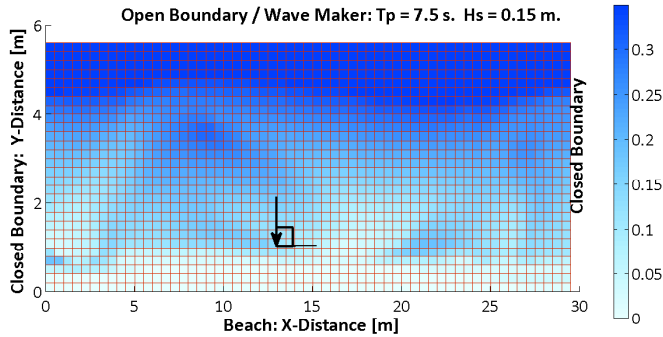


Figure 4.1: Tank study case for time step analysis.

4.3 Model Characterization

The combination of the proper orthogonal method (Cazemier et al., 1998) and the Taylor expansion, as presented in Vermeulen and Heemink (2006), requires a certain level of characterization of the model behavior. Here a brief analysis of the most relevant mathematical characteristics of the model is shown.

4.3.1 Time Steps and Temporal Evolution of the Model

Among the parameters related with the numerical solutions of the equations, the time-step size is of great importance. Different natural processes take place at different time scales. Of course, those natural processes that take place on time scales smaller than the time-step in which the equations are being solved will not be properly reconstructed by the model. In this sense, it is of great importance to guarantee that those that are relevant are properly described. Choosing a proper time-step size implies a trade-off, decreasing it will increase the reliability of the model at the cost of higher computational costs. The proper choice is that in which satisfactory results are obtained while keeping the computational expense acceptable. An analysis of the effect of different time steps on the solution of the model was carried out.

A grid of 59 (X direction) by 28 (Y direction) cells of 0.5 by 0.5 meters was used for the hydrodynamic computations. The wave module uses a grid of 59 (X direction) by 52 (Y direction) cells of the same size as the flow grid. The south, east and west boundaries are closed boundaries consisting of an erodible beach in the southern boundary and Neumann condition on the other two. The system is forced from the north boundary by beach-normal waves with a significant height of 0.15 m and a peak period of 3.5 s. The initial bathymetry consists of a set observations taken in a laboratory experiment done by Michallet et al. (2010, 2013). Figure 4.1 shows a description of the hydro-morphodynamic model used for the analysis. The bathymetry shown corresponds to the first measurements of water depth available.

The Courant condition analysis results on a maximum time step for accurate computation of wave propagation of 0.85 seconds and the maximum time step for horizontal advection of 1.16 seconds. To assess the model sensitivity to the time step size, five simulations were undertaken with different time-steps all lower than the Courant condition limits: 0.6, 0.48, 0.3, and 0.06 seconds. Each simulation consists of 10 days of coupled wave, flow and morphodynamic estimations plus a 3 hour spin up phase, at the beginning of the simulation, where no bed updates are taken into account. The main aim of the spin up phase is to reach the hydrodynamic equilibrium before the bathymetry starts to be modified. Once the morphodynamic processes start to be taken into account, the bed updates take place on every timestep. The wave estimations are updated every 20 minutes of hydrodynamic estimations (including the spin up time).

The differences between 0.6 (M06, red), 0.48 (M048, orange), 0.3 (M03, green) and 0.12 (M012, blue) seconds time step models with respect to a 0.06 (M006) seconds time-step simulation are presented in figure 4.2. The plots show a similar behavior of the deviations for all the analyzed model results up to day 5. After the sixth day the M012 model shows a lower divergence rate from the reference model (0.06 seconds) in terms of water depth and velocities. Regarding the water depths, after 10 days of simulation the M06, M048, and M03 models have deviated from the reference (M006) by twice as much as the M012 model (see upper panel of figure 4.2). The velocity estimations (central and lower panels of figure 4.2) show similar results. There is a clear difference between the M012 model and the rest of them; notice how the M06, M048, and M03 trajectories cluster and deviate from the M012 trajectory. This suggests significant differences in the morphodynamic evolution of the models due to the timestep differences.

Figure 4.3 shows how the system evolves during the 10 days simulation in terms of the root mean squared bathymetric changes at the available times, i.e. $\sqrt{E[(Z_t - Z_{t-1})'(Z_t - Z_{t-1})]}$ where $E[\cdot]$ is the expected value operator. All models (including M006) show a very similar behavior in time. The observed differences in figure 4.2 are clearly observed at the end of the simulation. Bear in mind that the only difference between these models is the time resolution in which the differential equations are resolved, and that all the timesteps are lower than the value for the Courant condition. Certainly, there are significant processes taking place at different time scales that seem to be neglected when time resolution is decreased. Notice that the trajectories start diverging as the intensity of the morphodynamic evolution decreases (6 days and after).

From a practical point of view, the observed differences due to the time step size are not significant for the analyses presented here. The reason for this is that the simulation time of all the models used here is less than 5 days. Because of this, the biggest time step that satisfies the Courant condition will be used to minimize the computational expense. Nevertheless, for analyses that involve long term simulations, the results presented here suggest that the simulation time step may have a significant

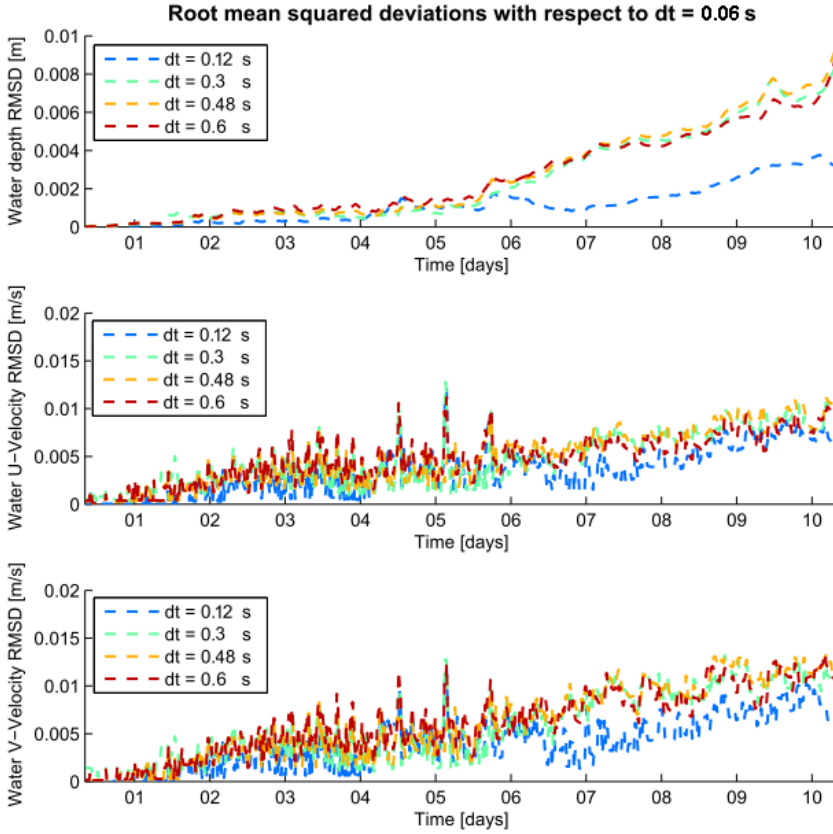


Figure 4.2: Bathymetric differences between simulations with various time steps a simulation with a 0.6 seconds time step

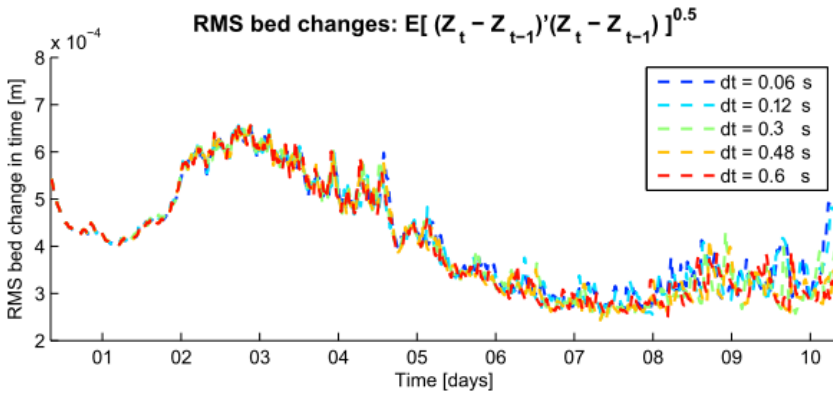


Figure 4.3: Behavior of the morphodynamic evolution of Delft3D.

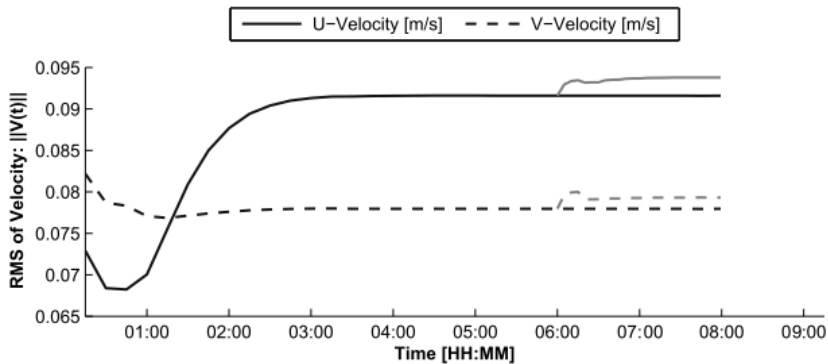


Figure 4.4: Effects in the velocity field due to restarting the model. The norm of each velocity horizontal components is shown ($\|V_t^{u,v}\|$). The non-restarted model is presented in dark gray while the restarted simulation is shown in light gray.

influence on the model results.

4.3.2 Effects of re-starting Delft3D

In the context of reduced model 4DVar as formulated by Vermeulen and Heemink (2006), a good model restart routine is a requirement; unfortunately, due to some implementation practices this capability is not always available or it generates undesirable effects. Here, the routine is tested by restarting a simulation at a certain point and comparing the subsequent model results between the non-restarted with the restarted run. The model configuration is preserved unchanged on the restarted run.

The reference model consists of 8 hours of only hydrodynamic simulation. The second model was stopped and restarted after 6 hours. Figure 4.4 shows the effects of the process on the velocity field. The *dark gray* solid- and dashed-lines show the behavior of the u-component and v-component, respectively. The *light gray* solid- and dashed-lines show the behavior of the velocity components for the restarted simulation. The restart takes place after the velocity field has already reached equilibrium. The perturbation of the simulation due to the restarting routine can be clearly observed at hour 6. The graph also shows that the restarted model reaches a different equilibrium quickly after the restarting point. From discussions with the team of developers of Delft3D (personal communication, 2009), it seems that the problem is that in the initial time step of the restart procedure, the wave forcings are not taken into account. This has serious consequences for wave driven systems (e.g. a swell dominated beach).

The consequences on the estimated water levels are shown in figure 4.5. In this figure the difference between the water levels of the restarted simulation and the water levels of the normal simulation (not restarted) is shown. A wave of considerable size moving seaward is observed during the first 10 seconds of the simulation. Once the

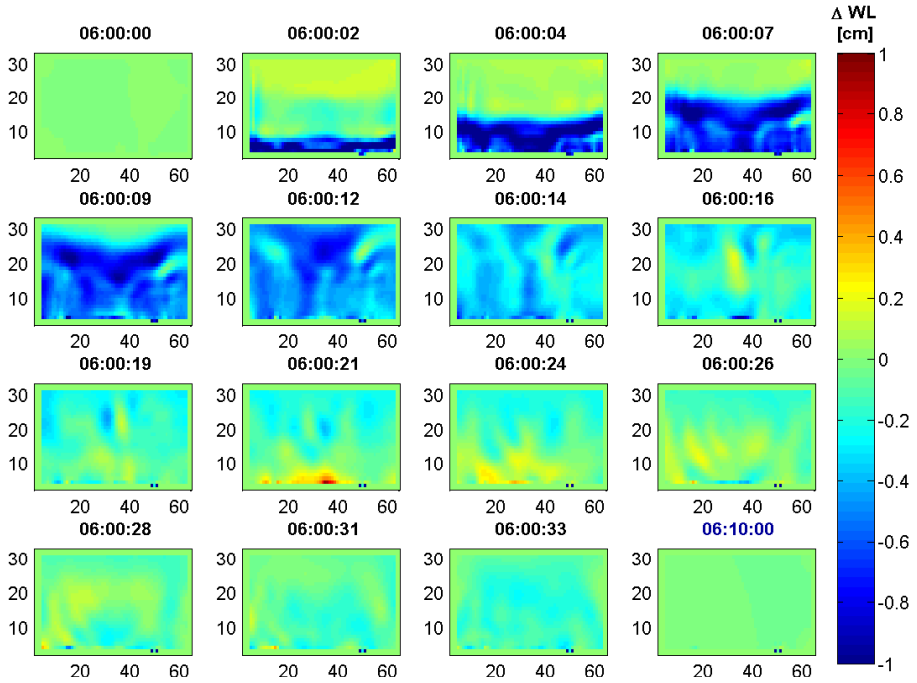


Figure 4.5: Water level changes (in cm) caused by not taking into account the wave forgings during the initial time step of the restarting procedure.

wave has left the domain, its effects remain visible for up to 30 seconds. After ten minutes of spin up of the restarted simulation, the effects are not present in all but a handful of grid cells where the effects remain permanently. The effects on the direction of the velocity field are relevant to this evaluation. Figure 4.6 shows the difference in the direction of the velocity in terms of the angle between the velocity vectors. As in the case of the water levels, permanent differences are observed after the 10 minutes spin up of the restarted simulation. Bear in mind that 0.25 radians is approximately 15 degrees. Notice that the effects on the velocity direction are not confined to the near shore area. In contrast with the water level, changes are observed in a considerably larger area after 10 minutes of the restart.

The combined effect of different velocity directions and velocity magnitudes has a significant effect on the morphodynamic evolution. Preliminary analysis (not shown here), show that the effects of restarting the model with no spin up are of the same order of magnitude as the sensitivity of the morphodynamic process to the wave parameters. In fact, the minimal sensitivity estimate depends significantly on the effects of the restarting process. Parameters with very low influence on the morphodynamic process may appear significant if its sensitivities were estimated by restarting the model

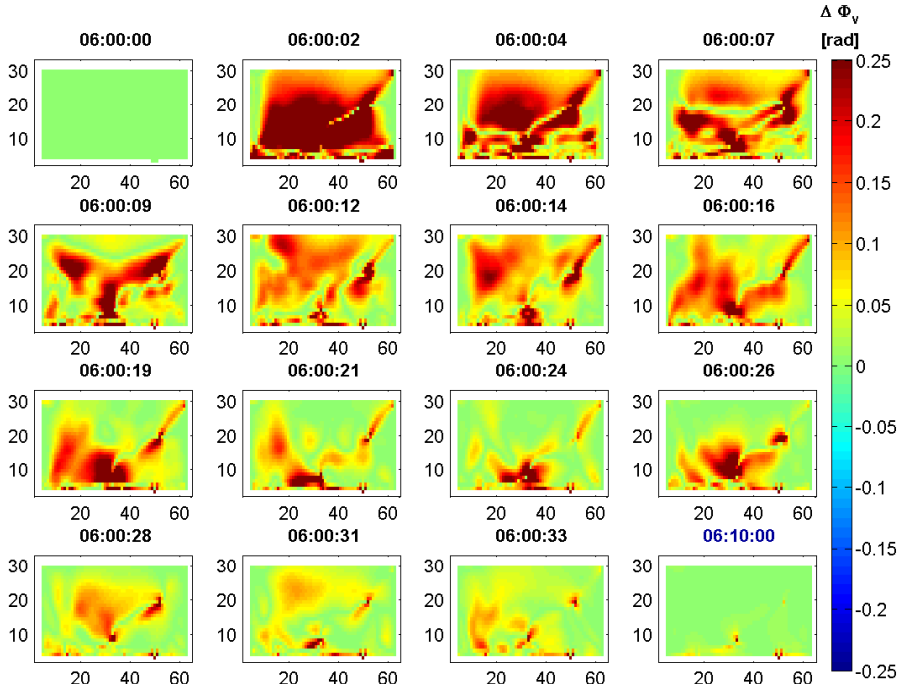


Figure 4.6: Velocity-direction changes (in radians) caused by not taking into account the wave forcings during the initial time step of the restarting procedure.

with no spin up time.

Given the effects of the restarting procedure on the evolution of the system, it is clear that a spin up time of at least 1 hour is necessary after restarting the model. Bear in mind that this will minimize the undesired effects on the model evolution but will not completely avoid them; the changes in some of the velocity directions and magnitudes will certainly have a long lasting effect on the model evolution. Alternatively, the use of the restarting procedure could be avoided by using a *coldstart* instead. The main problem with this approach is that the spin up time in this case is 3 times bigger which adds quite a big computational expense to the data assimilation implementation. Furthermore, partial analyses show that replacing the restarting procedure with a coldstart does not prevent side effects on the morphodynamic process. For this reason, it was decided to use the restarting procedure with an appropriate spin up time every time a model restart is required. For the application of EnMOR, restarting the model is not necessary and this problem is not applicable.

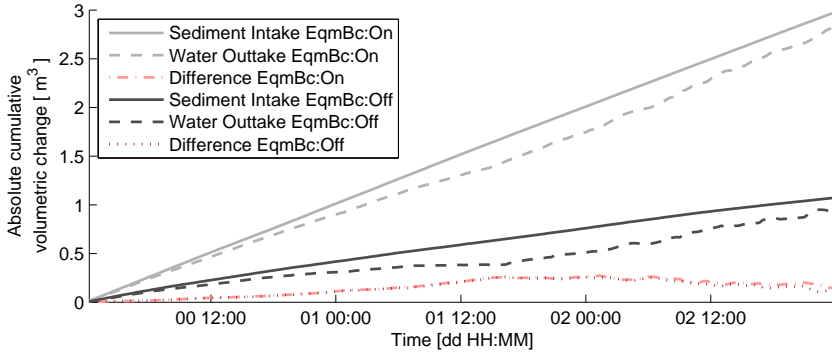


Figure 4.7: Sediment and water cumulative volumetric changes, for different assumptions of concentration of sediments at the model boundary. With *EqmBc:On* the equilibrium concentration profile at the model boundary is assumed. With *EqmBc:Off* a zero sediment concentration at the boundary was assumed.

4.3.3 Sediment and water volumetric changes

Sediment exchange at the model boundaries is an issue that demands some attention because there is usually no information about the sediment fluxes at these points and the modeling process is not straightforward. To deal with it, Delft3D offers the modeler the choice of prescribing a sediment-flux boundary condition or assuming an equilibrium sand concentration profile at the boundary. Here, the implications of these two conditions are evaluated.

The behavior of the total volume of sediments and water in the system can be seen in figure 4.7. The assumption regarding the boundary condition clearly has a significant effect. By assuming an equilibrium sand-concentration profile (*EqmBc:On*) the total volume of sediments (light gray line) in the system increases linearly with time, $\sim 1m^3 : 1day$. This phenomenon has an effect on the total volume of water (light gray dashed line) of the system; which decreases accordingly (notice that the figure shows water out-take). When a zero sand-concentration boundary is assumed (*EqmBc:Off*), the sediment volumetric increase rate (dark gray solid line) is considerably lower ($\sim 1m^3 : 3day$) and the water volume decrease behaves consequently (dark gray dashed line). Surprisingly, the sum of the sediment and water volumetric changes (red dotted lines) behaves very similar in both cases. Notice that for the first 36 hours the rate of sediment intake is higher than the rate of water outtake. This phenomenon seems to be reversed during the following 36 hours where the water outtake rate increases to account for the extra sediment (see the red dotted lines).

The decrease in the water volume agrees with the observed velocity field at the boundary shown in figure 4.8. Here, the evolution of the depth averaged velocity field at the open boundary is shown for the case of a zero sediment concentration boundary condition. It is important to mention that there is no significant difference

between these velocities and those of the model with the equilibrium concentration assumption at the boundary. Graphs showing results before 09:40, correspond to the spin up period (3 upper panels). Note that there is an effective outflow of water at all instances.

The observed phenomena could be explained by the manner in which the wave processes are coupled with Delft3D. The problem comes from solving the wave equations in a 2D context. Due to nonlinearities in the wave equations there is an import of water to the system. This additional water mass is usually compensated by an undertow. In the case of 2D simulations the resulting velocity profile is averaged. In this case this averaging results in an effective outflow of water.

It remains an open question which mechanism is responsible for the additional sediment accessing the system if the hydrodynamic results show a consistent water outflow. The only reason that the author can think of is that the additional water mass associated to the wave processes is prescribed to have some sediment concentration. Probably the concentration defined in the boundary condition. Still, in the case of a zero concentration boundary condition, what is the source of the additional sediments? Further analyses are necessary to characterize and understand this model behavior. Regarding the analysis presented in this manuscript, we will assume that these changes in the sediment mass do not change significantly the morphodynamic evolution and they will be ignored.

4.3.4 Linearization: Finite Differences

The linear approximation for the finite difference model order reduction (see section 3.1) requires the estimation of the model gradients with respect to the parameters of interest. Derivatives of two different nature need to be estimated: (1) the sensitivities are approximated using the traditional finite difference approach and (2) the projection of the model dynamics demands a gateaux derivative. Perturbed simulations are necessary in both cases but the perturbation in each case is conceptually different. In any case, the magnitude of the perturbation should be such that the gradient approximation is valid and accurate; i.e. the effect of the non-linear dynamics should be negligible. A simple test to determine if the effect of the non-linearities in the estimation of the gradient is insignificant, is to estimate the gradient with both a forward and a backward finite difference using the same perturbation. The two approximations should be equal. Since both the sensitivities and the model dynamics, change as the model evolves in time, multiple approximations of them are necessary for each phase of the model.

Finite difference estimation for sensitivities.

The upper panels of figure 4.9 show the effect of parameter perturbations of the model at different simulation times. Each plot uses three model simulations: (1)

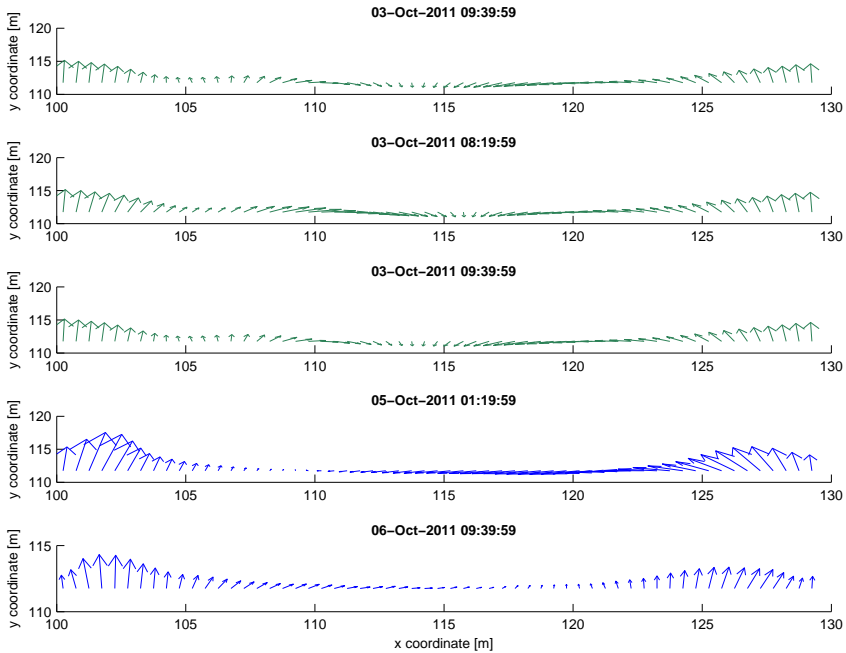


Figure 4.8: Velocity field at the open boundary.

reference, (2) a positive parameter perturbation (of the reference parameter set) and (3) a negative parameter perturbation. The magnitude of the perturbation is kept constant. A perturbation that remains within the linear *threshold* of the model will produce the same effects independent of its sign. The graphs show how the model behaves for the following parameter perturbations: wave significant height, $H_s \pm 0.01$ m (left); wave peak period, $T_p \pm 0.01$ s (center); and wave direction of incidence, $W_d \pm 0.1$ deg (right). It is surprising that even for a perturbation of 0.1 degrees in wave direction and 0.01 s in wave peak period the model behaves non-linearly (see for instance step 6 in center and right panels). For the case of W_d , observed results with perturbations of 1 and 5 degrees (not shown here) show larger changes. Despite the fact that from a physical point of view all perturbations are negligible they still have a measurable impact in the model results. For perturbations on peak period and wave direction the model seems to behave linearly during the first 24 hours (4 saving steps), contrary to what is observed in the case of wave significant height.

Finite difference estimation for Gateaux derivatives

As in the case of the parameter sensitivities estimation, it is necessary to use a proper perturbation size for the estimation of the directional derivative. The lower panels of figure 4.9 show the effect of the Gateaux perturbations at different times. Again, a

perturbation that remains within the linear *threshold* of the model will produce the same effects independently of its sign. For this analysis three modes were considered. The magnitude of the perturbation used for numerically estimating the directional derivative is 0.1. The analysis is not straightforward. The model is not perturbed homogeneously over all the morphodynamic grid. The perturbation depends on the mode used (column of the matrix P) and the size of the perturbation. Interestingly, preliminary experiments (not shown here) show no significant impact on the results of the assimilation scheme with choices of ϵ , as long as the perturbation remains within physical bounds.

From a morphodynamic perspective, the model simulations show two phases, initially there is an intense morphodynamic evolution of the system where the model bathymetry is rapidly adjusted to the prevailing hydrodynamic conditions. As the bathymetry begins to match the flow conditions, the sediment transport lowers and the bathymetric changes become significantly smaller; more generally, as *equilibrium* is reached the morphodynamic evolution slows down considerably. Figure 4.9, lower panels, suggest that the effects of the non-linearities associated to depth perturbations increase as the simulation evolves, specially for modes 2 and 3. Further analysis is necessary to assess whether the level of morphodynamic activity influences the model response to the perturbations. In general, the differences between the forward and the backward finite difference estimation are considerable, but making the perturbation smaller comes at the risk of losing too many features from the spatial pattern (in the product $\epsilon\hat{p}$) due to precision issues.

Discussion

The results presented here describe the effects of using the finite difference method to estimate the model gradient with respect to the wave input properties. A more detailed analysis (not shown here) suggests that the estimation of the gradient by using smaller perturbations does not change significantly the result of the derivative estimation. For the case of very small perturbations, numerical errors due to the precision of the algorithm start to become relevant, while bigger perturbations will trigger non-linear components of the model. Especially for the directional derivative small perturbations will cause loss of information associated to the small components of each principal mode. Nevertheless, the perturbations presented in this section provide an acceptable gradient approximation for practical purposes. The differences between the forward and the backward finite difference estimation can be minimized by using a second order accurate finite difference. Regarding the snapshot matrix generation, positive and negative perturbations should be taken into account to guarantee that the sub-space does not miss important dynamic components. For the case of the EnMOR method the considerations about the size of the perturbation for estimating finite differences is not applicable, but taking into account positive and negative perturbations in the construction of the ensemble is relevant.

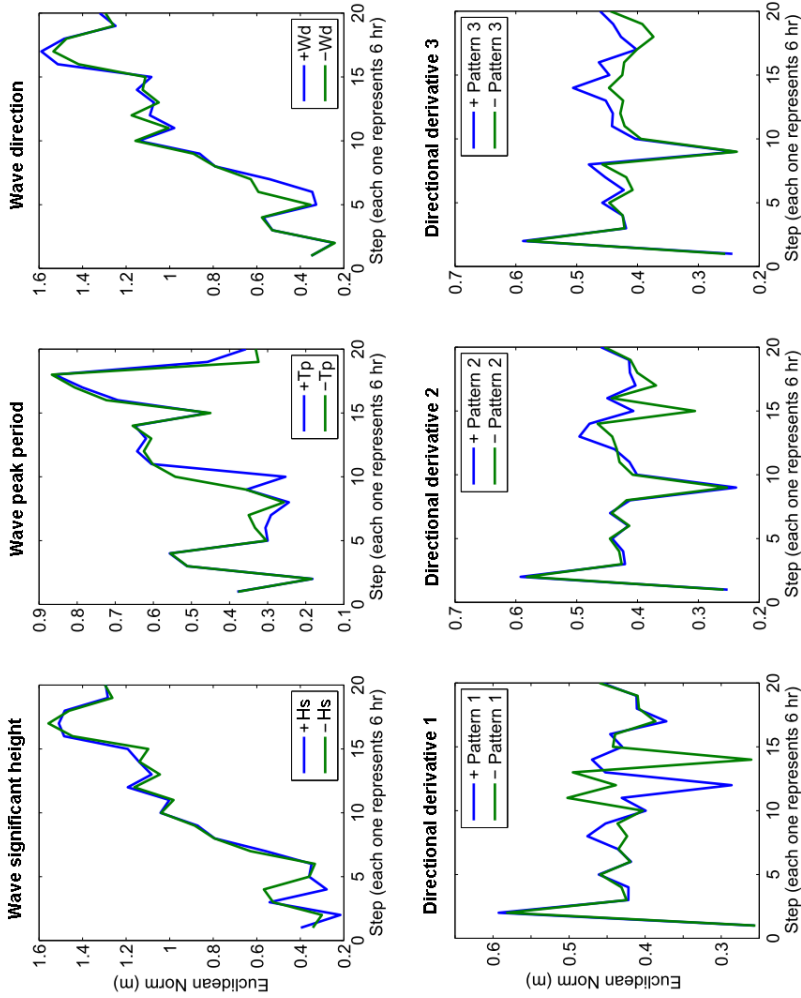


Figure 4.9: Measure (L2 norm) of the distance between the effects of positive and negative perturbations. *Upper panels:* Sensitivity analysis, parameter perturbations: $(H_s \pm 0.01m, T_p \pm 0.01s, \text{ and } W_d \pm 0.1deg)$. *Lower panels:* Directional derivatives, Gateaux perturbation: $\epsilon = 0.1$.

From a physical point of view, the finite difference analysis (sec. 4.3.4) presented here helps to characterize the evolution of the morphodynamic components as the simulation evolves. The effects of perturbing the parameter set change with the simulation time. Regarding the wave significant height, the non-linear effects seem to be present in the beginning of the simulation and not so much in the later simulation times. Wave peak period and wave direction of incidence, on the contrary, appear to trigger non-linear effects only on the later stage of the simulation. This is interesting because it suggests that the properties of the non linear behavior of the model depend on simulation time. It is difficult to assess what are the practical implication of these observations. A more detailed characterization is necessary to be able to generalize these results to other parameters of interest and to assert whether these observations are applicable to other morphodynamic models.

Chapter 5

Estimation of wave parameters

To assess the applicability of model reduced 4DVar to morphodynamic problems, we decided to focus on three of the most relevant parameters for characterizing the near-shore bathymetry (Wright and Short, 1984): wave direction of incidence (W_d), wave peak period (T_p) and wave significant height (H_s). As a background simulation, close to normal wave-weather conditions (Ranasinghe et al., 2004) were considered: $T_p = 7.8$ s, $H_s = 1.5$ m and $W_d = 84^\circ$. The set of observations was produced with the model as well (twin experiment). All the parameters other than the three of interest are the same across all Delft3D simulations including the twin experiment. Note, that the goal of the study is neither to accurately model the natural morphodynamic behavior of the beach nor to give a detailed description of the physical processes relevant for this site. Instead, the study strives to assess the potential of incorporating observations into this type of models.

Three different types of scripts were implemented: scripts that deal with the reduction of the model, scripts that communicate with the morphodynamic model and scripts that deal with the data assimilation procedure. The computational cost of these procedures is negligible in comparison to the average computation times of the morphodynamic model (more or less 4 hours each morphodynamic simulation). The necessary model simulations were undertaken in a cluster of 20 processors. The data assimilation scheme was implemented for a 5 day morphodynamic simulation. For the snapshot matrix, 20 snapshots (every 6 hours) of each perturbed run were used. Likewise, the number of linearization points along the reference trajectory was set to 20 for all the experiments shown here. This implies that the linear approximations are valid for 6 hours worth of morphological simulation.

This chapter is part of:

I. Garcia, G. Serafy, A. Heemink, and H. Schuttelaars. Towards a data assimilation system for morphodynamic modeling: bathymetric data assimilation for wave property estimation. *Ocean Dynamics*, pages 1–17, 2013.

Two different implementations of the technique are presented here. Firstly, the original model reduced 4DVar is evaluated. The idea is to assess the capabilities of the data assimilation scheme as proposed by Vermeulen and Heemink (2006). Secondly, a set of “single outer loop” implementations are undertaken to evaluate different features of the scheme. This knowledge will lead to evaluate optimization strategies for the construction of the ROM and the overall implementation of the technique. We will focus on how the initial perturbations and the size of the projection subspace influence the performance of the data assimilation process. In table 5.1 a description of each experiment is presented.

5.1 Study case and numerical model

Two grids of the study area were constructed. The wave grid extends over an area of 13800 meters along-shore by 4200 meters seaward, with a cell-size of $100 \times 100 \text{ m}^2$ (see figure 5.1). The flow grid with 149 (NS) by 88 (EW) cells of $15 \times 15 \text{ m}^2$, provides a detailed description of the bathymetry of Palm Beach (see figure 5.1). A model run encompasses 5 days of morphological updates with a flow time step of 12 seconds. Bathymetric information along with flow information is saved every 6 hours. Initializing the model (cold start) requires a *spin-up* phase, which was chosen to be of 8 hours length. During this phase, the stationary flow conditions prescribed by both the wave forcings and the bathymetry are reached. Once a stationary solution is attained, the morphological module is turned on. Every 15 minutes of flow simulation, the wave module is executed to make an update of the wave conditions. Given the nature of this work, no morphological scaling factor (Roelvink, 2006) was taken into account (see chapter 4).

A natural system, Palm Beach, was chosen for this study. This ensures that the complexity of the coupled morphodynamic model and its associated physical processes is taken into account. This beach is located in the northern area of Sydney; eastern Australia (see figure 5.1). It is a swell-dominated and micro-tidal beach of about 2 km length, with no significant seasonal variability in the wave conditions. The near shore beach slope is 0.03 and the median grain size is 0.30 mm (Ranasinghe et al., 2004). The dominant wave direction is from the SSE and wave heights averaging 1.5 m, but can reach 3 - 6 m during storm conditions (Short, 1992). The beach commonly exhibits all intermediate states and is known for the frequent occurrence of rip channels (Smit et al., 2008; Wright and Short, 1984). Observations show that beach is most commonly showing a *traverse bar and rip* (TBR, 22.8 days) state and in order of decreasing mean residence times: *rythmic bar and beach* (RBB, 11.8 days), *low tide terrace* (LTT, 9.3 days) and *longshore bar and trough* (LBT, 5.4 days) states (Ranasinghe et al., 2004). Down state changes usually take place sequentially from LBT to RBB, TBR, and, finally, LTT. Under storm conditions the beach is consistently taken to a LBT state independent of its initial state (Ranasinghe et al.,

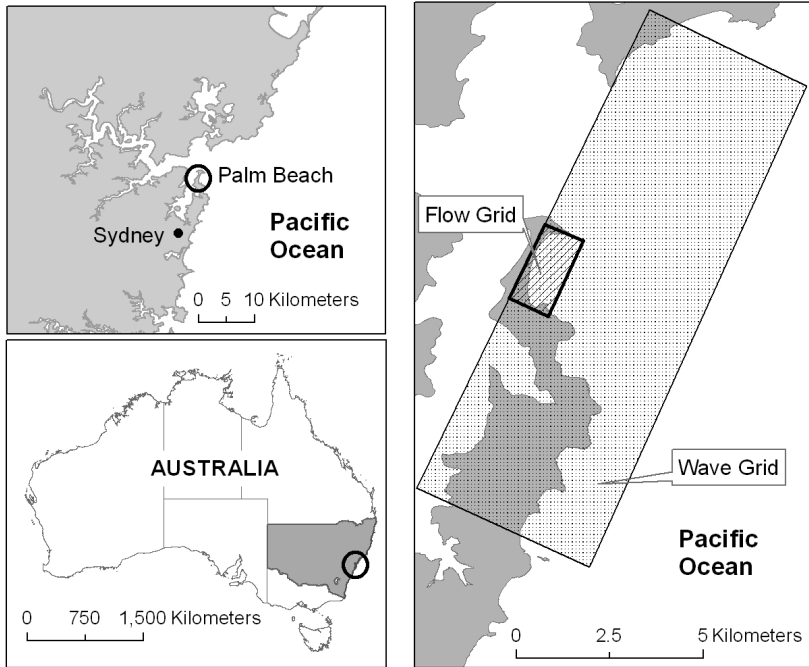


Figure 5.1: Geographic location of Palm Beach.

2004). Ranasinghe et al. (2004) show that in average the beach takes 40 days to switch from an LBT to a LTT state. A detailed description of the beach can be found in the works by Turner et al. (2006); Short (1993); Ranasinghe et al. (2004); Brander (1999). The initial bathymetry (see figure 5.2) and the description of the sediments and relevant physical processes were taken as described in Smit et al. (2008).

5.2 Observations and Weighing Matrices

One of the main advantages of an observation set coming from a twin experiment is that it allows the modeler to disregard the effect of model errors in the analyses. This is an important asset in the present study because it gives a better picture of the skills of the model reduced 4DVar.

Observations and Observation Operator. In order to analyze and characterize the performance of the scheme two sets of synthetic observations of water depths (m) were produced. The first set is an idealized condition of perfect measurements; the second set is a more realistic set of uncertain measurements. An observation is generated every 6 hours during the 5 days of simulation for all experiments.

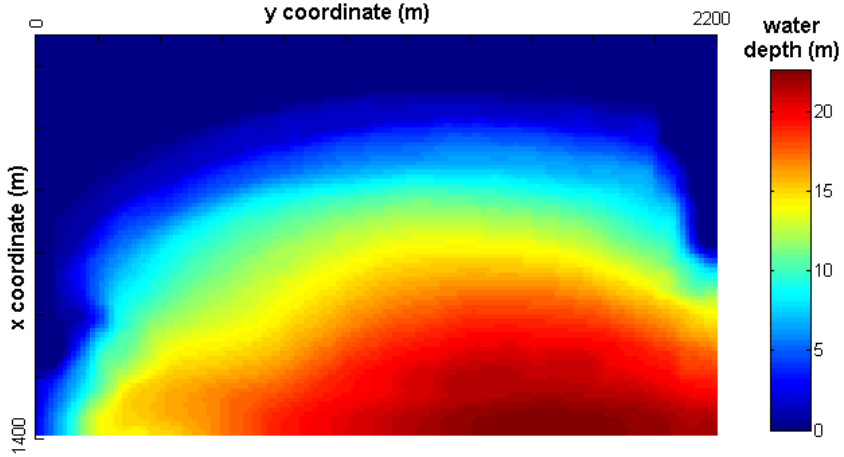


Figure 5.2: Initial bathymetry, as used in the work by Smit et al. (2008).

Observations at night time are not available in a realistic scenario. The number of observations for data assimilation is naturally relevant. From an optimization point of view, the modeler should aim to have a determined or over-determined system. This condition is usually unfeasible, and for highly undetermined operational forecasting systems the background term is very important to keep the optimization feasible. In a system like the one that is being presented here, the number of observations is determined by the size of the assimilation window and the frequency of measurements. If the amount of information coming from an observation dataset is considered to be insufficient to appropriately optimize the model, either a longer assimilation window should be taken into account (e.g. 7 days) or, if possible, the frequency of the measurements should be increased. If the frequency of observations is low and a constant parameter condition is not appropriate, time varying parameters can be taken into account by augmenting the input vector, e.g. $[H_s(t_1), H_s(t_2), \dots, W_d(t_1), W_d(t_2), \dots, T_p(t_1), T_p(t_2), \dots]$, to account for the temporal variability.

The perfect set of measurements has not been perturbed with noise and the full model domain was assumed to be observed. The parameter set used for producing these observations is: $H_s = 2.1$ m, $T_p = 7.5$ s and $W_d = 87.8$ deg; and it was assumed to be constant during the 5 days. This assumption is of course not realistic. In a real application, the choice of an assimilation window of this size would require augmenting the input vector as mentioned before. But for the purpose of this paper, this condition is acceptable.

The second set is an ensemble of 2000 observations of the same truth. The true state was taken as the set of perfect observations and was perturbed with an additive normally distributed error, $\mathcal{N}(\mu, \sigma^2)$ with $\mu = 0$ [m] and $\sigma = 0.1$ [m], to produce

the ensemble. Usually video-based observations only provide information about the bathymetry along the wave-breaking area. Therefore only grid cells that correspond to water depths between 1 and 4 meters were assumed to be observed. This error choice as well as the observed spatial domain follow estimations done by [Roelvink et al. \(2003\)](#) and [Uunk \(2008\)](#) for video-based observations of bathymetry.

Since both the state vector and observations consist of water depths in meters, the observation operator is linear and is defined as a logical (0/1) matrix that identifies the model grid cells where observations are taken.

Weighing Matrices. The common choice for the weighing matrices B and R is the error covariance matrix of the background and of the observations, respectively. The main advantage of choosing them is that the estimation process will weigh accurate measurements higher than inaccurate measurements. This is of particular importance in cases where the observations are of different nature or are coming from different sensors. For the case in which all observations have the same error, this matrix just scales the observation term to have the same order of magnitude as the background term in the objective function.

The prior covariance matrix (background covariance matrix) in all experiments was assumed to be diagonal. The standard deviation of the error was chosen to be 0.7 m for wave significant height, 1 s for wave peak period; and 10 deg for wave direction of incidence.

In the case of perfect measurements (experiment one), the identity matrix was used instead of the covariance matrix (zero matrix) for the observation weighing matrix. The choice of the identity matrix is for convenience. The zero matrix cannot be used because it is singular; making the objective function indeterminate and choosing a diagonal matrix with very small values will render the background term useless. The objective function will weigh the model deviation from the observation so highly that it will dominate the minimization process. From a practical point of view, the initial guess contains relevant information. It is usually based on expert knowledge and/or measurements (e.g. buoy measurements) and should be weighed accordingly in the estimation process. By choosing the identity matrix the estimation process will take into account information from both terms of the objective function, as happens in most operational data assimilation schemes. For the experiments with uncertain observations the observations covariance matrix: $0.01 * I_{N_{obs}} [m^2]$ (N_{obs} is the number of measurements), was used in the assimilation process.

5.3 Implementation of Model Reduced 4DVar

Here the procedure proposed by [Vermeulen and Heemink \(2006\)](#) is followed. The ROM is a linearization of the model trajectory prescribed by the initial parameter set. The parameter perturbations necessary to build the projection matrix are done by

Original	H_s [m]	T_p [s]	W_d [deg]	Cost
Loop 1: Three small parameter by parameter perturbations				
δx :	0.07	0.1	1.0	
Reference:	1.5	7.8	84.0	740.51
Initial Guess:	1.5	7.8	84.0	740.51
Loop 2: Three small parameter by parameter perturbations				
δx :	0.07	0.1	1.0	
Reference:	1.90	7.51	86.84	128.58
Loop 3: Three small parameter by parameter perturbations				
δx :	0.07	0.1	1.0	
Reference:	1.89	7.54	86.52	125.17
Single Outer-loop	H_s [m]	T_p [s]	W_d [deg]	Cost
Experiment 1: Three simultaneous perturbations.				
Initial guess:	1.50	7.80	84.00	740.51
	1.31	8.10	88.62	1336.11
	1.92	7.39	89.11	269.65
Reference:	<i>1.92</i>	<i>8.07</i>	<i>81.27</i>	<i>195.03</i>
Experiment 2: Three parameter by parameter perturbations.				
Initial guess:	1.50	7.80	84.00	740.51
	1.50	7.90	84.00	761.26
	1.50	7.80	85.00	743.05
Reference:	<i>1.57</i>	<i>7.80</i>	<i>84.00</i>	<i>586.54</i>
Experiment 3: Three parameter by parameter perturbations.				
Initial guess:	1.85	7.80	84.00	156.43
	1.78	7.80	84.00	227.89
	1.85	7.80	83.00	173.21
Reference:	<i>1.85</i>	<i>7.70</i>	<i>84.00</i>	<i>152.47</i>
Experiment 4: Six parameter by parameter perturbations.				
Initial guess:	1.50	7.80	84.00	740.51
	1.15	7.80	84.00	1605.58
	1.50	7.30	84.00	986.61
	1.50	8.30	84.00	895.62
	1.50	7.80	79.00	757.31
	1.50	7.80	89.00	787.28
Reference:	<i>1.85</i>	<i>7.80</i>	<i>84.00</i>	<i>156.43</i>
Truth H_s: 2.1 m — T_p: 7.5 s — W_d: 87.8 deg				

Table 5.1: Configuration of the experiments implemented.

varying one parameter per snapshot run. Several iterations were allowed to optimize the final estimation and to evaluate the performance of the assimilation. Each iteration requires the construction of a new ROM for the updated state vector. The initial set of parameters is presented as the *reference* run of the first iteration, namely: $W_d = 84.00$ deg, $H_s = 1.50$ m and $T_p = 7.80$ s. Subsequent *reference* trajectories correspond to the analysis (see table 5.2) of the previous iteration.

Table 5.2 shows the performance of the data assimilation scheme for three iterations. The update of the first iteration is remarkable. In the second and third loops the parameter set does not show any significant update. This behavior is explained by the form of the cost function which is shown in figure 5.3. A set of 86 model runs with different state vectors was used to approximate the cost function. A linear interpolation between the different (86) model runs (red dots) is used. The color bar represents the cost function value. Note that the value of the cost function shows little

Iteration 1			
	H_s [m]	T_p [s]	W_d [deg]
Reference	1.50	7.80	84.00
Perturbation 1	1.57	7.80	84.00
Perturbation 2	1.50	7.90	84.00
Perturbation 3	1.50	7.80	85.00
Update	1.90	7.51	86.84
Patterns (Energy)	5 (83.70%)		
Reference's Cost	740.51		
Update's Cost	128.58		
Iteration 2			
	H_s [m]	T_p [s]	W_d [deg]
Reference	1.90	7.51	86.84
Perturbation 1	1.97	7.51	86.84
Perturbation 2	1.90	7.61	86.84
Perturbation 3	1.90	7.51	87.84
Update	1.89	7.54	86.52
Patterns (Energy)	8 (84.77%)		
Reference's Cost	128.58		
Update's Cost	125.17		
Iteration 3			
	H_s [m]	T_p [s]	W_d [deg]
Reference	1.89	7.54	86.52
Perturbation 1	1.96	7.54	86.52
Perturbation 2	1.89	7.64	86.52
Perturbation 3	1.89	7.54	87.52
Update	1.90	7.62	85.38
Patterns (Energy)	8 (84.57%)		
Reference's Cost	125.17		
Update's Cost	104.04		
Truth H_s: 2.1 m — T_p: 7.5 s — W_d: 87.8 deg			

Table 5.2: Implementation of model reduced 4DVar as presented by Vermeulen and Heemink (2006).

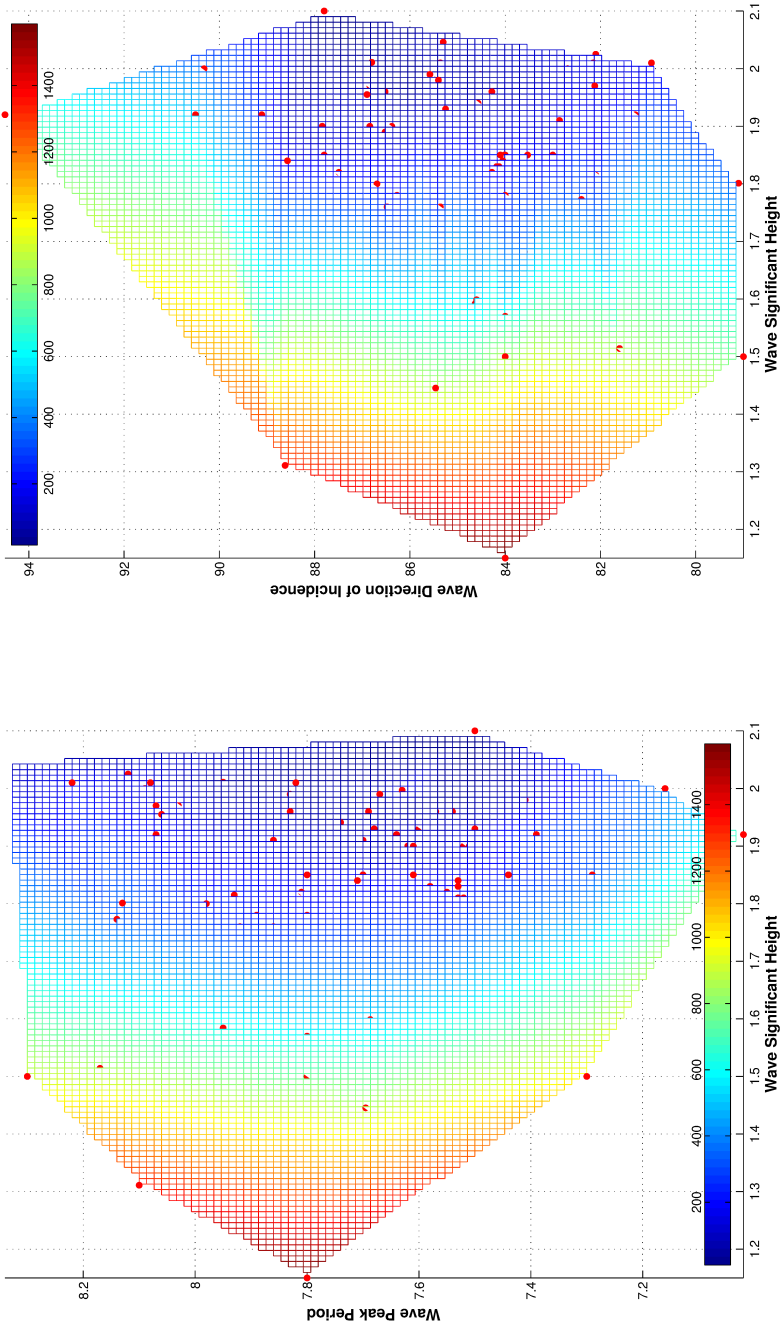


Figure 5.3: Plots of the cost function (the color represents the value of the cost function) with respect to the three parameters of interest. The surface is the result of a linear interpolation in between model runs with different state vectors. The red dots mark the places where a measurement of the cost function is available.

sensitivities to T_p and W_d (see in particular 5.3a) when the significant wave height is in the range [1.7, 2.1]. Nevertheless, the gain in terms of cost is significant as it drops from 740.5 to 128.58 only in the first loop and drops further to 104.04 in the subsequent iterations.

5.4 Single outer iteration experiments

Four different experiments were implemented in order to characterize the performance of the technique and to identify its most relevant features. One of our focuses is reducing its computational expense, which depends mainly on: (1) the number of parameters of interest and (2) the number of patterns used in the ROM. The number of parameters of interest is usually a variable that offers little flexibility. On the other hand, the number of patterns is a very flexible parameter. Two questions come to mind: (1) what are the real implications of increasing the number of patterns? And (2) Is there a way to increase the quality of the patterns? These two questions are addressed with the experiments presented here. The first question is addressed by considering the impact of the number of patterns used in the construction of the ROM. To this end, in each experiment 5 to 10 patterns were used to prescribe the reduced space. The second question was addressed by evaluating the magnitude of the perturbations used for defining the projection matrix and the way these perturbations are implemented.

The reference (or background) constitutes a key concept in this technique since the Taylor approximation is built around it. Normally, the reference trajectory corresponds to the model simulation with the initial set of parameters. Nevertheless, from the $N_\alpha + 1$ simulations necessary to span the parameter space (the initial ensemble), there is no guarantee that the initial-guess corresponds to the point with the lowest cost function. If in fact the initial-guess does not correspond to the best point at hand, why use it as the reference? Intuitively, the closer the reference run is to the real system state, the better the capabilities of the linear approximation to optimize the model. Following this hypothesis, experiments 1 through 4 do not linearize the model around the initial-guess-trajectory (initial-guess parameter set: $W_d = 84.00$ deg, $H_s = 1.50$ m and $T_p = 7.80$ s). Instead, from the $N_\alpha + 1$ simulations the one that corresponds to the lowest cost function has been chosen (see REF, in table 5.3) as the linearization trajectory.

Experiment 1. The objective of this experiment is to determine if there is any gain from simultaneously perturbing all parameters. For this, three simultaneous perturbations were used to compute the projection matrix (table 5.1). The results of the experiment for different number of patterns are shown in table 5.3. The optimization process worked better when the projection space is limited to the subspace spanned by the first 5 modes, 96% of the energy. The selection of the reference run for the

linearization process seems to have contributed significantly to the improvement of the H_s estimation. For the other two parameters, instead, this selection came at a high cost. Smaller perturbations might be useful to alleviate the cost of choosing the reference from the ensemble of simultaneous perturbations.

Experiment 2 and 3. These two experiments aim to assess the importance of the direction (sign) of the perturbation. In both cases the same three small perturbations (see table 5.1) were used. For the case of experiment 2 the perturbations are all positive while for experiment 3 the perturbations are all negative. Contrary to the previous case, the selection of a linearization point different from the initial guess does not show any negative effects on any parameter.

Results from experiment 2 show that the updates of T_p , are moving away from the truth in all but the best result. The other two parameters are updated in the right direction. It should be highlighted that in terms of the most sensitive parameters, H_s and T_p , the reference run of this experiment is the farthest away from the truth. Because of this, the validity of the ROM might be limited. Results from experiment 3 show a very poor performance for the H_s as the scheme consistently fails to update it. The parameter W_d also shows very little improvement. On the other hand the parameter T_p shows a significant improvement during the update. It appears as if the sub-space is specially tailored to highlight the dynamics associated to the latter.

Putting into perspective the results from both experiments, it looks like the direction in which the perturbation is performed has a significant effect on the overall performance. Observe that each experiment shows good performance for parameters that correspond to a perturbation done in the correct direction (i.e., the perturbed parameter is closer to the true value). In experiment 2 the parameter T_p is consistently updated away from the truth, while in experiment 3 this same parameter shows the best end result. The contrary happens in the case of the H_s and W_d ; thus reinforcing the hypothesis of the importance of the direction of the perturbation.

Experiment 4. In this case 7 ($2N_\alpha + 1$) model simulations are used to span the parameter space for the modes identification. The perturbations are presented in table 5.1. The perturbations are made in both the positive direction and the negative direction. Notice that for these perturbation magnitudes the model non-linearities take a significant role in the effects on the model behavior (see chapter 4). Therefore, the model behaves differently for a positive perturbation than for a negative perturbation. Again, the model run that corresponds to the lowest cost function is used as the reference simulation of the ROM. The contribution of the extra number of model perturbations to the optimization procedure is significant. With 10 patterns corresponding to 98.7% of the energy, the optimization shows the best estimates. All the parameters are consistently updated in the right direction.

	Initial	REF	5	6	7	8	9	10	Truth
Experiment 1									
<i>Energy</i>			96.22%	96.97%	97.63%	98.17%	98.54%	98.84%	
H_s [m]	1.50	1.92	1.91	2.00	2.01	2.01	1.97	1.97	2.10
T_p [s]	7.80	8.07	7.86	8.09	8.22	8.08	8.07	8.03	7.50
W_d [deg]	84.00	81.27	82.86	82.69	80.93	82.15	82.12	82.28	87.80
Cost function	740.51	194.42	137.27	141.07	162.33	148.92	156.96	149.15	-
Experiment 2									
<i>Energy</i>			92.01%	93.71%	94.71%	95.53%	96.24%	96.90%	
H_s [m]	1.50	1.57	1.76	1.78	1.82	1.84	1.8	1.76	2.10
T_p [s]	7.80	7.80	7.86	7.89	7.81	7.71	7.98	7.92	7.50
W_d [deg]	84.00	84.00	85.36	86.27	87.49	88.57	86.69	86.48	87.80
Cost function	740.51	586.49	255.24	224.00	161.17	150.93	204.62	254.11	-
Experiment 3									
<i>Energy</i>			75.26%	79.27%	82.01%	84.41%	86.23%	87.94%	
H_s [m]	1.85	1.85	1.83	1.82	1.81	1.83	1.84	1.85	2.10
T_p [s]	7.80	7.70	7.58	7.55	7.53	7.53	7.53	7.61	7.50
W_d [deg]	84.00	84.00	84.18	84.28	84.37	84.13	84.05	84.02	87.80
Cost function	155.93	151.98	189.57	210.77	230.74	209.83	199.81	162.2	-
Experiment 4									
<i>Energy</i>			96.66%	97.34%	97.94%	98.26%	98.50%	98.72%	
H_s [m]	1.50	1.85	1.98	1.93	1.93	1.92	1.96	1.96	2.10
T_p [s]	7.80	7.80	7.41	7.50	7.60	7.64	7.83	7.69	7.50
W_d [deg]	84.00	84.00	85.25	84.32	84.48	83.8	84.53	84.53	87.80
Cost function	740.51	155.93	130.77	113.06	90.84	88.24	85.85	60.11	-

Table 5.3: Assimilation Results

Discussion. Table 5.3 shows the performance of the scheme for the different experiments implemented here. Experiment 4 shows consistently better results than the rest suggesting that the perturbation choice has a significant effect on the optimization process. Note that the reference trajectory for experiments 3 and 4 are very similar in terms of cost function values. Nevertheless experiment 4 shows a very good update while experiment 3 shows less satisfactory results. In this case the performance of the scheme is independent of the choice of the reference set of parameters. This reinforces the argument that the direction of the perturbation plays a significant role in the performance of the scheme.

Despite the fact that in experiment 1 all parameters are perturbed in both directions, the results are less satisfying than those of experiment 4. Even though the cost function values are not drastically higher than those of experiment 4 the updates of T_p and W_d are not as satisfactory. The problem might be related to the simultaneous perturbations. The sensitivity of the cost function to the parameter H_s is significantly higher than to the rest of the parameters (compare the decrease in cost between *initial guess* and *reference* for experiments 2 and 3). The effects of changes in the W_d and T_p parameters are concealed by the effects of the changes in H_s , thus depriving the ROM of relevant information regarding the model behavior.

Analyzing the experiments in the context of the implementation presented in section 5.4 it is worth noting that only experiment 4 shows a better performance in the quality of the update. Bear in mind that even though this experiment is the most computationally expensive, it is still around one third as expensive as the three iterations of the original implementation.

Figure 5.4 shows the depth averaged velocity field for the lowest cost function in each of the experiments. The improvement in the overall estimation of the velocity field is especially clear for the analysis coming from experiment 4 (lower center graph). The figures also show the complexity of the problem at hand.

5.5 Noisy Observations.

The main aim of this chapter is to assimilate observations that resemble the characteristics of actual measurements. A set of 2000 observation ensembles was generated. Each observation ensemble is the result of perturbing the truth with a normally distributed random noise. In the operational case, this ensemble of observations is not available. In this sense, the form of the distribution of the updates provides a better insight into the performance of the model reduced 4DVar.

Figures 5.5 and 5.6 show frequency distributions and scatter plots, respectively, for the ROM presented in *experiment 4* with 3, 7 and 10 modes in the context of noisy observations. In all cases the frequency distributions appear to be symmetric and centered at the update produced for perfect observations. The scatter plots show a weak positive correlation between the T_p and the W_d . In average, there does not

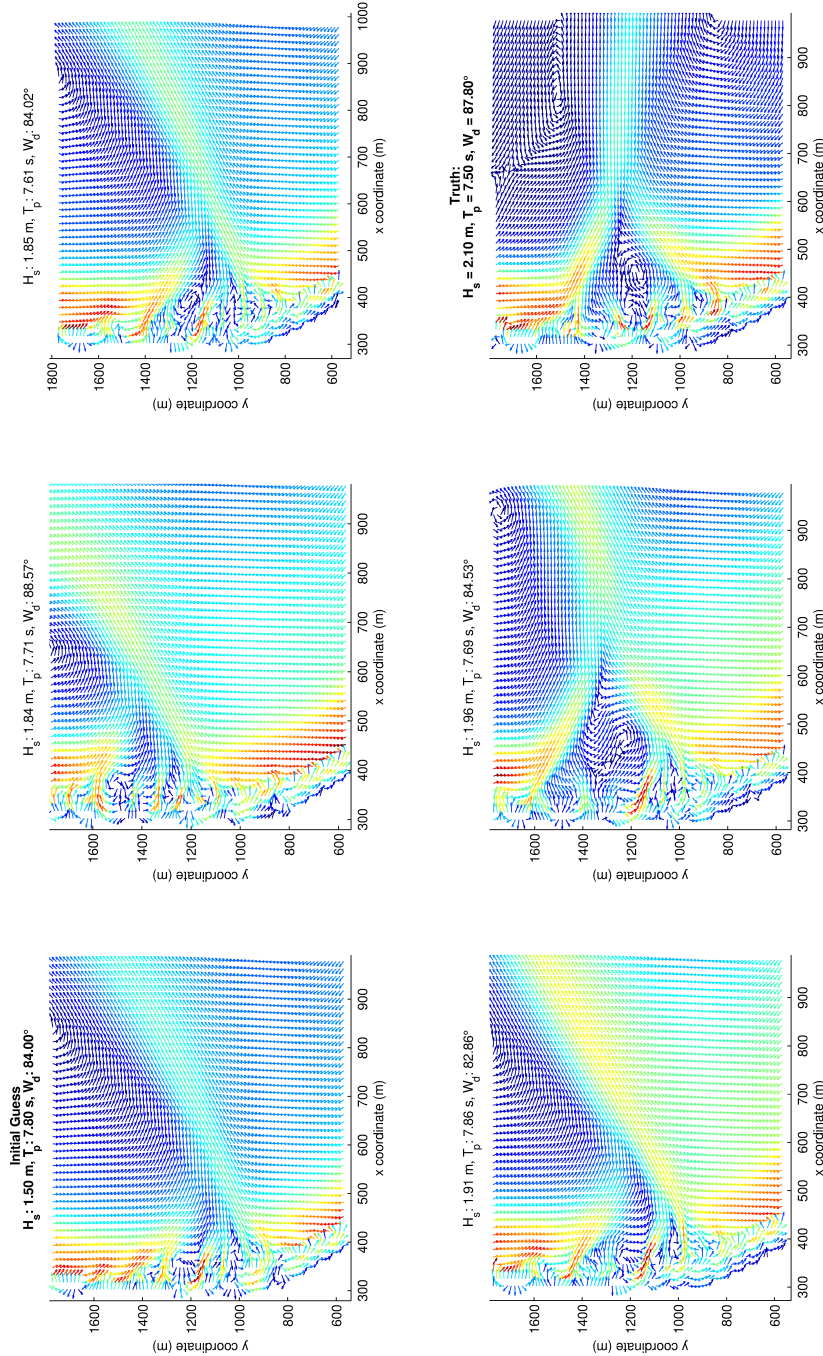


Figure 5.4: Depth averaged velocity fields of the updated model with the lowest cost function in each experiment shown in table 5.3. Experiment 1 upper center panel. Experiment 2 upper right panel. Experiment 3 lower left panel. Experiment 4 lower center panel.

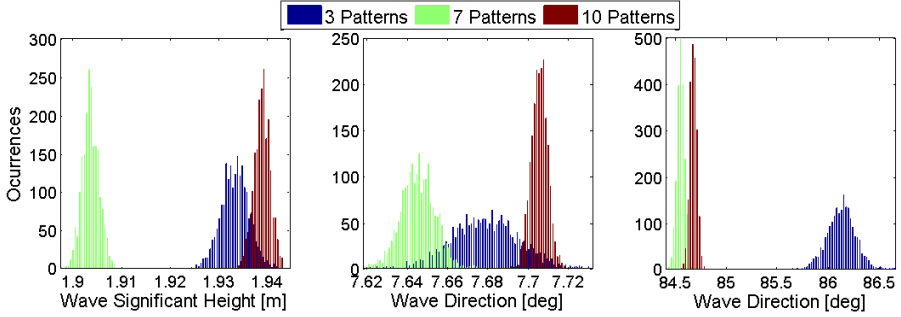


Figure 5.5: Distribution of the updates for an ensemble of 2000 members of noisy observations. Same ROM as the one used in the 4th experiment (see table 5.3) with: 3 modes (left panel), 7 modes (center panel) and 10 modes (right panel).

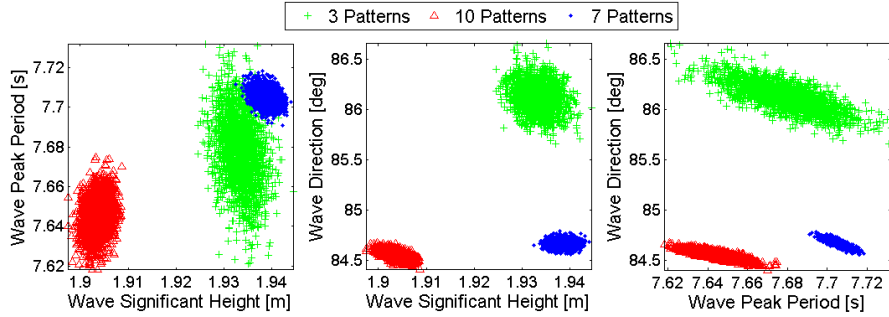


Figure 5.6: Scatter plots of the parameter updates for an ensemble of 2000 members of noisy observations. Same ROM as the one used in the 4th experiment (see table 5.3)

seem to be a significant decrease in the quality of the update with respect to the other experiments discussed here. The spread of the three parameters is small in all cases which implies that irrespective of the ensemble member that is chosen the parameter update is sensible. There is a significant decrease in the standard deviation of the distribution of analyzes by increasing the number of modes used to define the subspace. In this sense the use of a bigger subspace is justified and advised. As the number of modes used for the reduced order model is increased, the fluctuations of the update around the mean value are diminished.

5.6 Discussion

Model reduced 4DVar was implemented successfully for the morphodynamic model Delft3D. In general, the scheme shows to be robust and consistent in lowering the

prescribed cost function. Furthermore, we have been able to implement the data assimilation scheme in a model that encompasses all the processes associated with the temporal evolution of sediment transport processes.

The quality of the ROM, understood as its capacity to reconstruct the *direction* in which the system reacts to parameter changes, is of great importance for the efficiency of the data assimilation procedure. The sensitivities of the model to its different components are fundamental for the construction of the ROM. These sensitivities change in time; therefore, several ROMs valid for subsets of the full temporal domain need to be created. One of the main strengths of the scheme is that it is suitable for parallel implementation. All initial perturbations may be computed in parallel and, subsequently, all derivative computations may be done in parallel as well. From a practical point of view, there is no significant change in computational expense for state vectors of smaller sizes than the available processors.

An intelligent selection of modes in combination with an appropriate choice of perturbations for their generation, seems to have a significant impact on the effectiveness of the technique. The increase in the size of the subspace has a significant role in minimizing the spread of the updates in the case of noisy observations. Therefore, it is advisable to keep the sub-space as big as possible while maintaining it practical. The size of the perturbations necessary for computing the modes that span the projection sub-space has a significant impact on the performance of the technique. It is difficult to diagnose the most appropriate perturbation magnitude since they are: case, model and initial condition dependent. The sign (direction) of the perturbation has an effect on the overall performance of the data assimilation process as well. On this regard, perturbing in both directions is advisable because it increases significantly the performance of the scheme and may lessen the number of outer loops, which are far more costly than the additional model executions. On the other hand, smaller perturbations may also be implemented instead of perturbations in both directions; but detailed analysis of each parameter is necessary in order to assess the correct perturbation magnitude. The scheme shows no detriment in performance due to observation noises similar to those present in video-based observations. Nevertheless, the number of modes proved to be relevant to minimize the dispersion of the updates. The scheme shows to be very robust to deal with observation uncertainties. Regarding the outer loops, the information produced in each iteration is mostly ignored in subsequent iterations (projection matrix is not reused nor the snapshot matrix). Furthermore, the initial perturbation runs are discarded after the projection matrix is produced; on this issue, further research is advised to assess strategies that would make a better use of this information.

The study case implemented in the present work aims at assessing the feasibility of using model reduced 4DVar for morphodynamic modeling. The results show the potential of the technique and proof that data assimilation is achievable even for such complex models. In order to take full advantage of the potential of the model reduced

4DVar, a bigger study case with real observations and a larger number of parameters is advised. The work has produced relevant insight on the characteristics of the use of ROMs for data assimilation purposes. Most of the known assimilation techniques have shown to have difficulties dealing with high dimensional non-linear problems. An application of the technique that includes in the state vector the initial bathymetry, morphological parameters, hydraulic parameters and numerical parameters could show the full potential of the data assimilation scheme presented here.

Chapter 6

Laboratory data assimilation: 19 parameters problem

This chapter addresses two issues, an analysis of the morphodynamic evolution of a highly observed system from a modeling point of view, and the evaluation of the performance model-reduced 4DVar for parameter estimation. The information used in this section comes from a laboratory experiment undertaken at the SOGREAH LHF facility, France. The use of this type of data has the advantage that it is highly accurate and the system is measured in detail. Since the measurements come from the actual evolution of a morphodynamic system, the model errors start to play a role in the assimilation process. Consequently, the first objective of the analyses presented here is to assess the capacity of the model to reconstruct the evolution of the morphodynamic system. Aside from the model characterization, a partial implementation of the enMOR method is performed to evaluate if it is practical for large scale applications. Only the directional derivatives were estimate with the enMOR method. The model sensitivities to input parameters are estimated using the finite difference approach.

Detailed descriptions of the laboratory set up are presented in [Michallet et al. \(2013, 2010\)](#); [Castelle et al. \(2010\)](#). Accurate and detailed bathymetries were measured during the 5 weeks that the experiment took place. Three categories of shore normal wave conditions: *energetic*, *moderate with a large period*, and *moderate with shorter period*, were applied in the experiment. For the work presented in this chapter, measurements taken for the moderate-large-period wave conditions were used.

The available information reconstructs a down-state beach sequence LBT-RBB-TBR-LTT. [Michallet et al. \(2013\)](#) describes in detail the different phases that the system goes through and classifies the state at each of the bathymetric measurements. Initially, a shore parallel bar progressively migrates onshore developing into a single crescentic bar unconnected to the shore. The bar continues to move shoreward and

attaches to the beach as it develops shallow shoals and rip channels. As the shoals attach to the shore a continuous decrease in rip channel depth is observed along with the appearance of a single rip channel. At this point, the rate of morphological changes progressively decreases and the only notable evolution is the accretion of the rip channel producing an almost featureless terrace-like morphology.

The chapter is organized in 4 sections. In section 6.1, the laboratory experiment is described and the available measurements are presented and characterized. Section 6.2, gives a detailed description of the numerical model. In section 6.3 the results of the modeling and data assimilation are presented. Finally, a discussion and concluding remarks are presented in section 6.4.

6.1 Observations: laboratory set-up

The wave basin is a 30 m by 30 m tank with a 60 independently controlled piston-type wave maker. The bathymetric measurements covered an area of 15 meters ($7.84\text{ m} \geq x \geq 22.84\text{ m}$) in the cross-shore direction by 25 meters ($3.12\text{ m} \geq y \geq 28.02\text{ m}$) in the alongshore direction. A total of eleven observations of the down-state sequence, corresponding to the moderate with a large period wave conditions, are available at: 9:40, 15:40, 18:00, 21:00, 26:00, 31:20, 37:20, 40:00, 45:40, 51:40, 59:40 and 66:00 from the beginning of the experiment. Figure 6.1 shows the observed bathymetries during the accretive phase of the experiment. Since the measurements are of a higher resolution than the morphodynamic model, the information was spatially averaged to match the model resolution ($0.5 \times 0.5\text{ m}$). The measurements have a millimeter precision and were done every 10 cm in the alongshore direction and every 1 cm in the cross-shore direction. The measurements were done with a laser profiler which required the tank to be emptied for every measurement. To take into account the precision of the profiler and the possible effects of emptying the tank, a 2 millimeter error was assumed for each bathymetric measurement. The observation errors were assumed independent.

The still water level at the wave maker was $h_0 \approx 76.5\text{ cm}$ for all experiments. Fine sand with a density of 2.65 g/cm^3 and a median diameter, d_{50} , of 0.166 mm was used for the experiment. This results in a particle settling velocity, w_s , of 2 cm/s . A moderate wave condition with a large period corresponds to waves with a significant height, H_s , of 18 cm and a peak period, T_p , of 3.5 s . This produces a dimensionless fall velocity, $H_s/T_p w_s = 2.5$, in the intermediate range (Wright and Short, 1984). An irregularity on the wave conditions, for promoting the development of 3D patterns, was added by imposing a damped motion on the center wave paddles. The effects of this irregularity in the morphodynamic evolution is not clear.

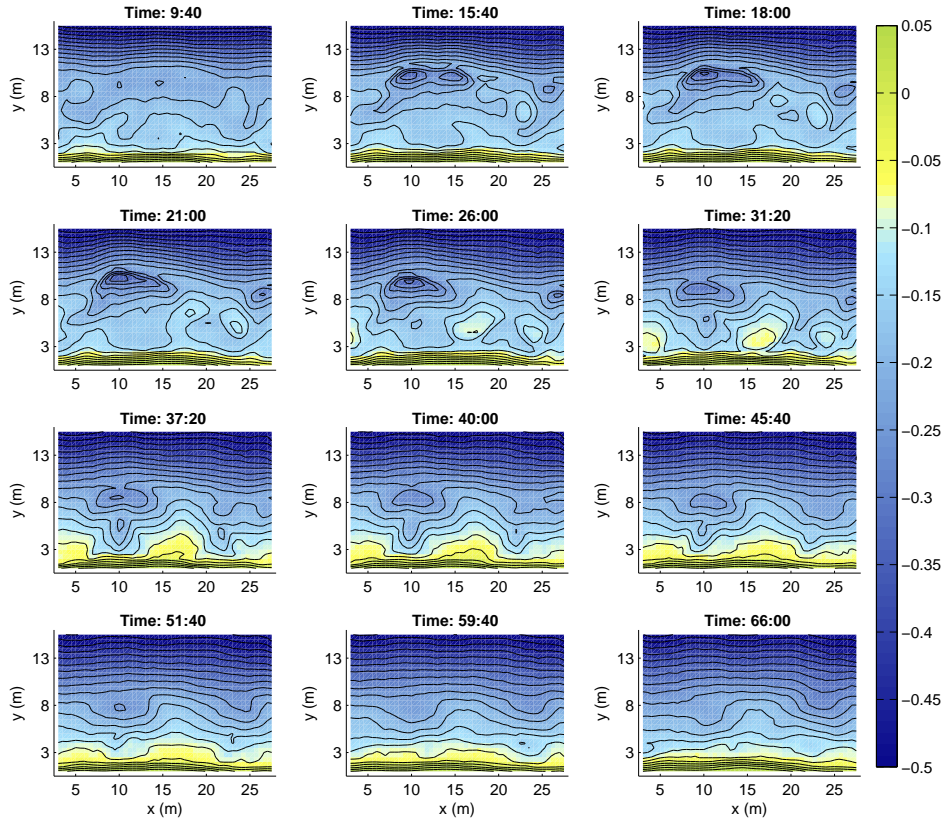


Figure 6.1: Bathymetries during the accretive sequence. Time since the initiation of the experiment.

6.2 Morphodynamic model

For the hydrodynamic estimations a grid of 59 (X direction) by 28 (Y direction) cells of 0.5 by 0.5 meters each was built. The wave module used a bigger grid of 59 (X direction) by 52 (Y direction) cells of the same size as the flow grid. The extra grid cells in the y direction are just to locate the wavemaker at the same distance from the shoreline as in the physical model (see Michallet et al., 2010). The south, east and west boundaries are closed boundaries. The beach is located in the south while the east and west boundaries were taken as Neumann boundaries. The observation at 9:40 was taken as the initial bathymetry. The system is forced from the north boundary by beach-normal waves with a peak period of 3.5 s. Though the wavemaker was configured to generate waves with significant height of 0.18 m, wave measurements south to the wavemaker show that the actual wave height is closer to 0.15 m. The latter was used in the model. The surf zone bathymetry at initial time (9:40) is shown

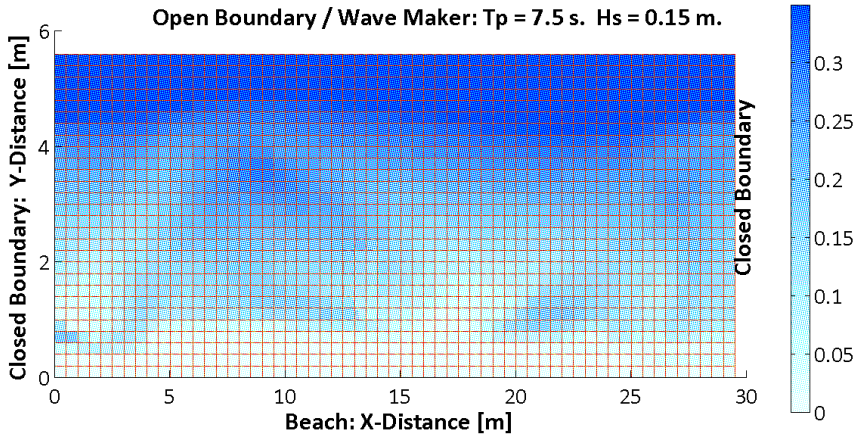


Figure 6.2: Morphodynamic Model. Bathymetry of the *surf zone* (0 - 6 m. cross shore from the beach).

in figure 6.2, deeper areas show a along-shore homogeneous bathymetry.

A convergence analysis showed that the maximum time step for accurate computation of waves is 0.84 seconds. Therefore, a time step of 0.6 seconds was used for all simulations presented here. The wave conditions are recalculated every 20 min of simulation. As in the laboratory experiment, no tides were considered in the model. The system state is saved every 20 minutes of simulation. The median sediment diameter (d_{50}) was set to $164 \mu m$ as described in Michallet et al. (2013). The rest of the sediment characteristics have their default values.

Before starting the morphodynamic updates a hydrodynamic spin up is necessary, to ensure that the hydrodynamic condition is in equilibrium with the prescribed initial bathymetry and the wave forcing. The spin up time for cold-start model simulations is 180 min. For sensitivity runs where the model is restarted from a previously estimated state, the spin up time is chosen to be 100 min. Regarding the model configuration, there is no morphodynamic scaling taken into account (Roelvink and Broker, 1993).

The estimation parameter set consists of 19 wave and hydrodynamic parameters. Table 6.1 shows the selected parameters and a brief description of them. From the list of parameters presented in the table, the first five parameters are part of the hydrodynamic module and, with the exception of *COMWriteInterval*, they play an important role in the pick-up and dispersion of sediment. The following 4 parameters are used in the wave module (SWAN), controlling the forcings of the system. Finally, the last 9 parameters are part of the morphodynamic module. These parameters characterize the pick-up, transport and deposition of sediments.

Nonphysical values are particularly problematic for the automation of the assimilation scheme. A parameter like viscosity, for example, takes values between

Acronym	Units	Description
Ccofl:	$[m^{0.5}/s]$	Roughness coefficient in U-velocity direction
Ccofv:	$[m^{0.5}/s]$	Roughness coefficient in V-velocity direction
Vicouv:	$[m^2/s]$	Horizontal eddy viscosity
Dicouv:	$[m^2/s]$	Horizontal eddy diffusivity
Dryflc:	[m]	Threshold depth for drying and flooding
ComWritel*	[min]	Frequency of wave updates
WaveHeight	[m]	Wave significant height
Period	[s]	Wave peak period
Direction	[deg]	Wave direction of incidence
DirSpreading	[deg]	Wave directional spreading
ThetSD:	-	Factor for erosion of adjacent dry cells
SusW:	-	Wave-related suspended sediment transport factor
BedW:	-	Wave-related bed-load sediment transport factor
Sus:	-	Multiplication factor for suspended sediment reference concentration
Bed:	-	Multiplication factor for bed-load transport vector magnitude
AksFac:	-	van Rijn's reference height = AKSFAC * KS
RWave:	-	Wave related roughness = RWAVE * estimated ripple height.
AlfaBs:	-	Streamwise bed gradient factor for bed load transport
AlfaBn:	-	Transverse bed gradient factor for bed load transport

Table 6.1: Set of estimation parameters.

0 and $10m^2/s$ (see pg 76 Deltares, 2009a); but the background value is $0.001m^2/s$. With this initial value it is common to get negative values during the minimization process which would produce numerical problems. To avoid this from happening, the maximum and minimum values of each parameter are enforced in the estimation process. This is done by projecting each parameter value (valid for the whole real line) to an interval of the real line delimited by its minimum and maximum value. The projection and its derivative is given by,

$$\theta = \min + (\max - \min)\exp[-\exp(z)]$$

$$\partial\theta/\partial z = -(\max - \min)\exp[-\exp(z) + z],$$

where z is a scalar in the real line, θ is a scalar in the interval $[\min, \max]$ and \min and \max are the minimum and maximum values, respectively, of z . The projection and its derivative are used in the ROM and the reduced adjoint, respectively, to enforce each parameter interval.

Table 6.2 shows the minimum and maximum acceptable values for each parameter. These values were chosen following the user-manual's suggestions or were based on expert knowledge. The table also shows the standard deviation of their prior estimate. This standard deviation is used to produce the background covariance matrix which, for all experiments, is assumed to be diagonal. The standard deviation of each parameter was kept big enough to avoid biasing the estimation procedure.

6.3 Implementation and results

To analyze the morphodynamic evolution of the system four parameter estimation processes were undertaken; one for each morphodynamic transition; namely, (1) LBT-RBB, (2) RBB-TBR, (3) TBR-LTT and (4) LTT settling. The first estimation (from now on *experiment LBT*) covers the initial 12 hours of the experiment which includes the change from a LBT state to a RBB state. For this transition there are three bathymetric observations available at 15:40, 18:00 and 21:00. For the transition from a RBB state to a TBR state, a second estimation procedure (referred to as *experiment RBB*) that covers 10 hours of morphodynamic evolution was implemented. The modeling covers the time between 18:00 and 28:00. There are two bathymetries available for this transition: 21:00 and 26:00. The third parameter estimation process (referred to as *experiment TBR*) considers the next 16 hours of the experiment; from 26:00 until 42:00. This time comprehends the transition from a TBR to a LTT beach state. For this time span there are 3 observations available at: 31:20, 37:20 and 40:00. The last estimation (from now on *experiment LTT*) covers the stabilization process of the beach in the low energetic state (LTT). The model considers the final 22:00 hours of the down state sequence; from 45:40 to 67:40. There are three observations during this period of time: 51:40, 59:40 and 66:00.

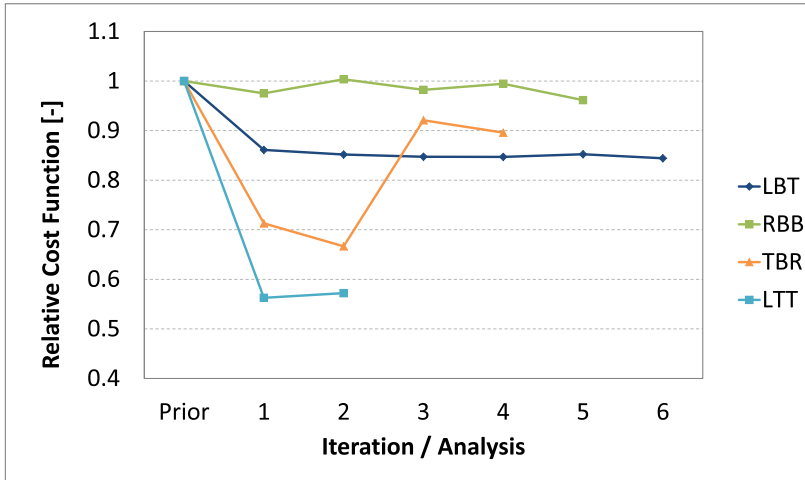


Figure 6.3: Normalized cost function for each experiment and for each iteration. Each cost function value has been divided by the initial cost. Values less than 1 stand for an improvement of the model behavior with respect to the observations.

The method requires the construction of a ROM valid in the vicinity of the background model trajectory. For the identification of the background model an expert was asked to calibrate the model to reconstruct the observed dynamics appropriately. The outcome of the calibration process is presented in table 6.2 (see table column *background*). The calibration was done manually and based on visual comparison. This parameter set was used as the background run for all experiments shown here. The background errors were considered independent and the standard deviation of each parameter was taken from ranges suggested in [Deltares \(2009a\)](#) or as suggested by experts. The values are shown in table 6.2.

The ROM is a piecewise linearization of Delft3D where each piece approximates 20 min of the morphodynamic simulation. The sensitivities (S_k in equation 3.4) were estimated by using a central finite difference scheme. The projection space was estimated from 50 perturbed runs with snapshots taken every 20 min, and the number of modes/patterns (rank of the subspace) is 40 in all experiments. The dynamic component of the ROM (D_k in equation 3.4) was estimated as shown in section 3.2.

6.3.1 Performance of the parameter estimation

The ratio of the cost over the initial cost of each experiment and each iteration is shown in figure 6.3. The difference in the number of iterations is due to the execution time of each experiment: 12 hours of simulation for experiment LBT, 10 hours for experiment RBB, 16 hours for experiment TBR and 22 hours and experiment

LTT. Figure 6.3 shows that the scheme was particularly efficient at estimating the parameters for experiments LBT and LTT. Regarding experiment RBB the scheme seems to be having a hard time improving the performance of Delft3D. In fact, the parameter set corresponding to the lowest objective function is very similar to the prior parameter set (further discussion later, see figure 6.10). This suggests that the initial calibration was particularly suited for this morphodynamic phase. Regarding experiment TBR the scheme performs very good during the first two iterations after which the performance drops significantly. A diagnosis of this behavior is presented in section 6.3.2. The lowest cost function happens at: analysis 5 for LBT, analysis 5 for RBB, analysis 2 for TBR and analysis 1 for LTT. Among the optimal parameter sets, the roughness coefficient in the U-velocity direction, viscosity, diffusivity and wave significant height and period change in the order of 1 standard deviation. This is shown in table 6.2 where the parameter set corresponding to the lowest objective function value of each experiment are given. Figure 6.4 shows the corresponding morphodynamic simulation for each experiment (one experiment per row). All the parameter changes are within two standard deviations, see table 6.2, which suggests that the optimal parameter set is within prior uncertainty bounds.

During the transition from LBT to RBB (first row of figure 6.4) the model is neither able to reconstruct the observed trough at $(x, y) \approx (10, 12)$ nor the pit observed at $(x, y) \approx (16, 4)$ (see second row panels of figure 6.1). The shallow area at $(x, y) \approx (24, 7)$ is reconstructed with the proper size and location. Despite not being able to reconstruct the trough and pit configuration, once it is provided as the initial condition in experiment RBB, the model is capable of reconstructing their evolution satisfactorily (see second line of figure 6.4). This is also true for experiment TBR, where not only the trough is diffused at the proper rate but also the formation of shoals is properly reconstructed. Finally, the evolution towards of the LTT state shows a very similar trajectory to the one observed. Nevertheless, the shoreline at time 66:00 is less uniform, suggesting a different shoreline evolution after 20 hours of simulation.

The root mean square error (RMSE) of each experiment for each observed bathymetry and for each iteration is shown in figure 6.5. For RMSEs under 0.015 m the optimization process fails to improve the model performance, this may be explained by the assumed observation uncertainty, 0.02 m. In these cases, the model results are within observed uncertainties and are therefore correct predictions. For experiment LBT, the model is improved at all observation points in a very similar way. The model is still improved after this first iteration although the increment in performance is marginal. For experiment RBB, observation 3 (RBB Obs 3, green line with crosses) is only 3 hours after the starting time. At this point the model sensitivity to the parameter set is still very limited and improving the model can only be achieved by estimation of the initial condition as part of the data assimilation process. This will be discussed more extensively in section 6.3.3. Regarding experiment TBR, the fact that observations 6 and 7 are only 3 hours away from each other biases the scheme toward improving the

Acronym	Units	Min	Max	σ	BG	LBT	RBB	TBR	LTT
Ccofu:	$[m^{0.5}/s]$	5	80	7	30	25.298	30.459	34.301	24.793
Ccofv:	$[m^{0.5}/s]$	5	80	7	30	28.947	29.611	27.742	26.525
Vicouv:	$[m^2/s]$	0.001	10	0.04	0.01	0.0754	0.0178	0.0076	0.04197
Dicouv:	$[m^2/s]$	0.001	10	0.04	0.01	0.026	0.0161	0.0622	0.0206
Dryflc:	[m]	0.001	0.07	0.01	0.05	0.0485	0.0507	0.0456	0.0585
COMWriteInterval	[min]	5	120	10	20	19.0	20.0	21.0	20.0
WaveHeight	[m]	0.09	0.21	0.02	0.15	0.1375	0.1592	0.1408	0.1016
Period	[s]	2.8	4.2	0.1	3.5	3.4451	3.5059	3.4199	3.4513
Direction	[deg]	-30	30	5	0	-5.6521	1.6416	5.9072	-1.2647
DirSpreading	[deg]	0	10	1	5	4.9502	5.0876	5.0455	4.7352
ThetSD:	[-]	0	1	0.1	0.6	0.6001	0.5999	0.6015	0.6
SusW:	[-]	0	1	0.1	0.1	0.0608	0.1011	0.1216	0.0486
BedW:	[-]	0	1	0.1	0.1	0.0767	0.0924	0.1205	0.0842
Sus:	[-]	0	1	0.12	0.35	0.3352	0.3456	0.2963	0.1591
Bed:	[-]	0	1	0.12	0.35	0.35	0.35	0.3497	0.3505
AksFac:	[-]	0	0.1	0.1	0.05	0.05	0.05	0.05	0.05
RWave:	[-]	1	3	0.2	2	1.9868	1.9971	1.9797	1.8827
AlfaBs:	[-]	0	10	0.2	1	1.0006	0.9961	1.0011	0.9976
AlfaBn:	[-]	0	10	0.2	1.5	1.4999	1.4999	1.5012	1.5003

Table 6.2: Background parameter set and estimated sets for the different assimilation procedures. *BG stands for background. **CWI stands for COMWriteInterval. *Min*, *Max* and σ stand for minimum allowed value, maximum allowed value and standard deviation, respectively.

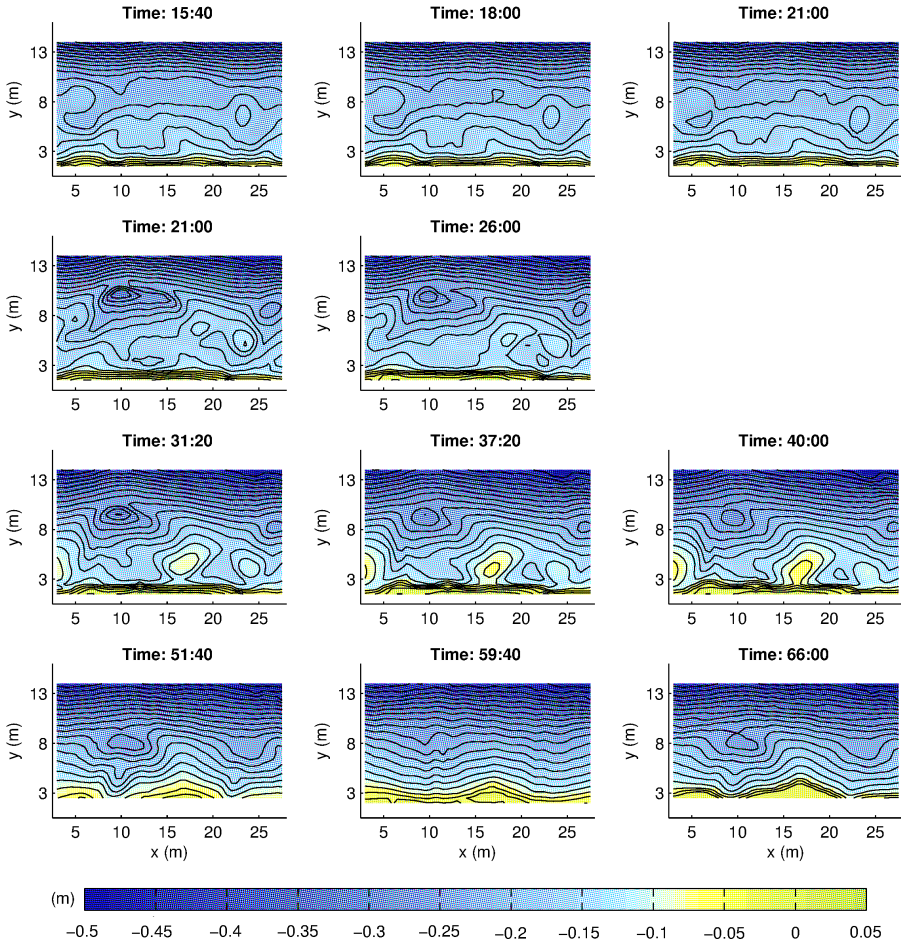


Figure 6.4: Results of the morphodynamic simulation corresponding to the model with lowest objective function of each experiment. Each line corresponds to an experiment. LBT: analysis 5. RBB: analysis 5. TBR: analysis 2. LTT: analysis 1.

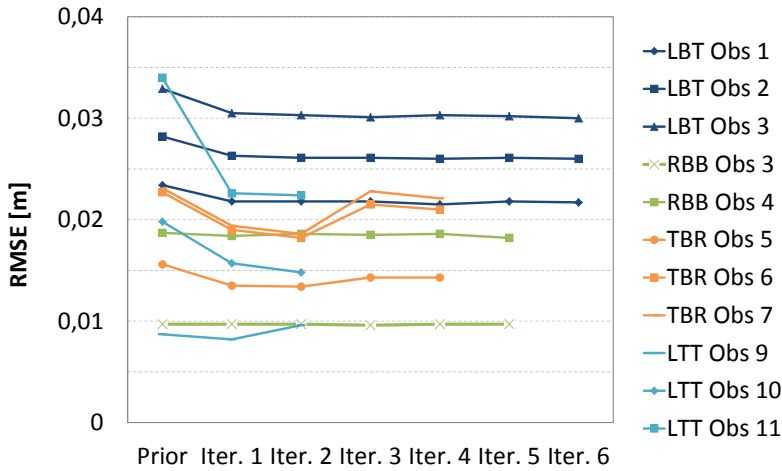


Figure 6.5: RMSE between the model and the observations for each experiment.

model results during this period of time. This explains why the RMSEs of these two observations behave so similarly. For experiment LTT, despite the 6 hours between the initial time and observation 9 (51:40) the model results compare well with the measured values (very low RMSE, see figure 6.5), i.e. the model predicts the measurement successfully. At observation time 11, approximately 20 hours after the simulation initial time, a significantly higher RMSE is observed and a significant improvement takes place. Notice that the changes in iteration 1 and 2 have comparatively little impact on the RMSEs at observation times 9 and 10. This suggests that the model is able to reconstruct accurately the evolution of the system for the prescribed hydrodynamic conditions.

In figures 6.6, 6.7, 6.8 and 6.9 the results of the optimization procedure are illustrated by showing the difference between the morphodynamic model and the observations ($model - observations$) for the first four iterations of the minimization process. Positive values (green to red) in the plots represent areas where the model predicts larger depths than is observed, negative values indicate an under-prediction of the water depth. Each line of plots corresponds to an iteration and the color limits are the same for all figures to make the comparison easier.

For experiment LBT the difference shows the inability of the model to reconstruct the trough (see figure 6.6). This is in agreement with the discussion regarding the capabilities of 2D models for trough generation given in [Ranasinghe et al. \(2004\)](#). Instead of generating a trough at the correct position, a deepening to the north and east of the trough location is observed. However these deeper areas diminish in size and depth as the optimization develops. In fact, careful analysis shows that the difference in the trough area decreases during the parameter estimation process. Near

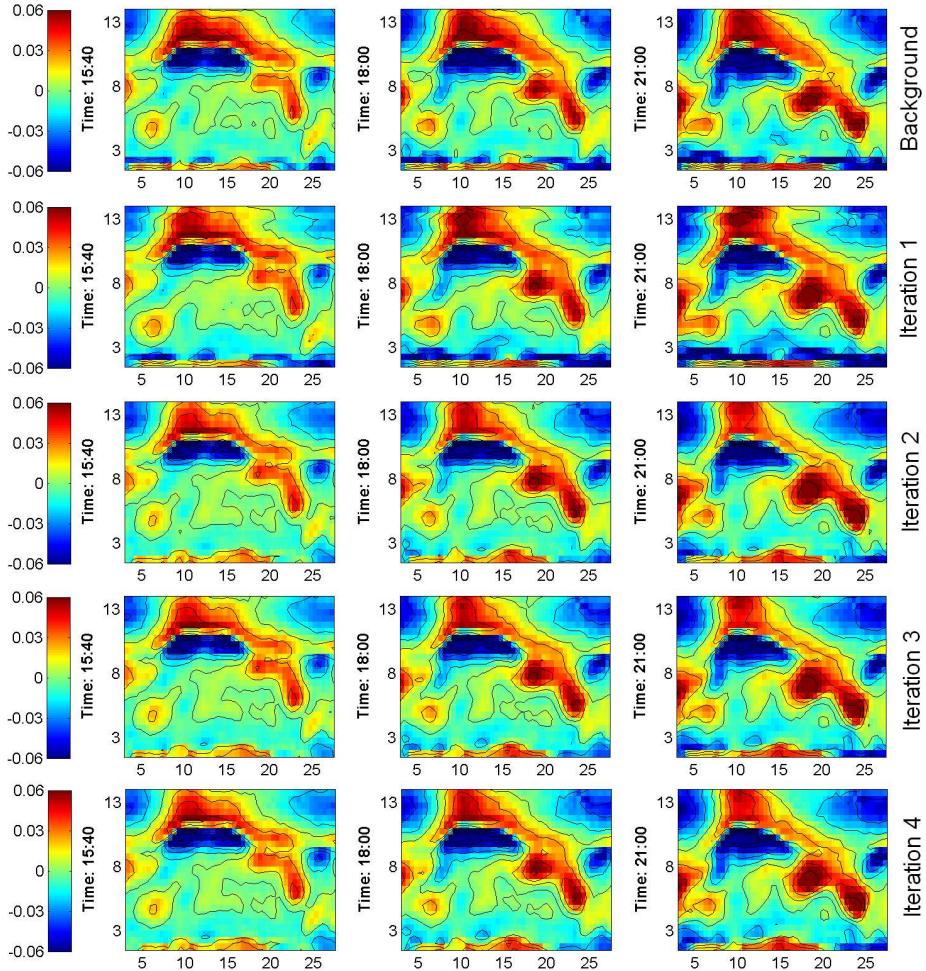


Figure 6.6: **Experiment LBT**: Difference between the morphodynamic model and the observations ($model - observations$) for the first four updates. Positive values (green to red) represent areas where the model predicts larger depths than measured, negative values indicate an under-prediction of the water depth.

the shoreline, the optimization process manages to reconstruct the shoreline behavior accurately, resulting in errors that are consistently decreasing with each iteration step.

The estimation process for the *RBB to TBR state transition* (figure 6.7) shows improvements in the surf zone area estimations at 21:00 (see the evolution at $(x, y) \approx (16, 7)$ and $(x, y) \approx (24, 4)$). In the deeper areas the modeled deposition rate seems to be higher than the ones observed in the trough area. This contrasts with the case of the surf zone where the model deposition rates are lower. Aside from this local changes, the initial low RMSEs values suggest that the initial parameter set is able to reproduce the morphodynamic evolution accurately, which explains the limited effects of the optimization. Furthermore, during the beginning of the simulation the model sensitivity to the control parameters is usually low, hindering the capacity to improve the model performance at initial simulation times.

The transition from a TBR to a LTT beach state (see figure 6.8) is particularly interesting due to the behavior of experiment TBR during the estimation process. During the first two iterations a considerable improvement at the last two observation times takes place. For the first observation time a significant improvement of the near shore area is observed, but the rest of the spatial domain is hardly improved. For the other two observation times improvements in the near shore area take place in the subsequent iterations. Most of the improvements on the near shore area are reversed in the last iteration. Notice the error drop that takes place in the deeper area ($y > 8$) in the last iteration. As the error in the deeper area is decreased the errors in the near shore area are considerably increased; this suggests the necessity of considering some parameters as space dependent. This behavior is in agreement with what Serafy et al. (2011); Altaf et al. (2010) report in their estimation process for a North Sea Delft3D model of particulate matter and tidal behavior, respectively. The fact that the last two observations are so close together, biases the estimation process because changes that produce an improvement in the initial observation at the cost of a marginal deterioration in the other two observations are likely to be discarded. Despite a slight increase in the RMSE in iteration 3 (31:20), figure 6.8 shows an increase in the error in highly dynamic areas and an overall low and smooth error map in the rest of the domain. This smoothness is lost again in iteration 4. For the first three iterations, the morphodynamic model is eroding the deep areas excessively as can be seen at coordinate (17,9) for the three observations.

Experiment LTT (settling of the LTT state, figure 6.9) shows a consistent improvement of the model performance during the optimization process. The overall decrease of the errors suggests that the model is capable of reproducing the relevant dynamics during this phase of the morphodynamic evolution. Bear in mind that the simulation spans a considerably longer time than that of the other 3 cases. The model results shown in figure 6.4 suggest some difficulties to reconstruct the shoreline behavior, but figure 6.9 shows that this is more likely due to a poor prior parameter set. The improvement of the model in the shallow areas is very significant for times 59:40 and

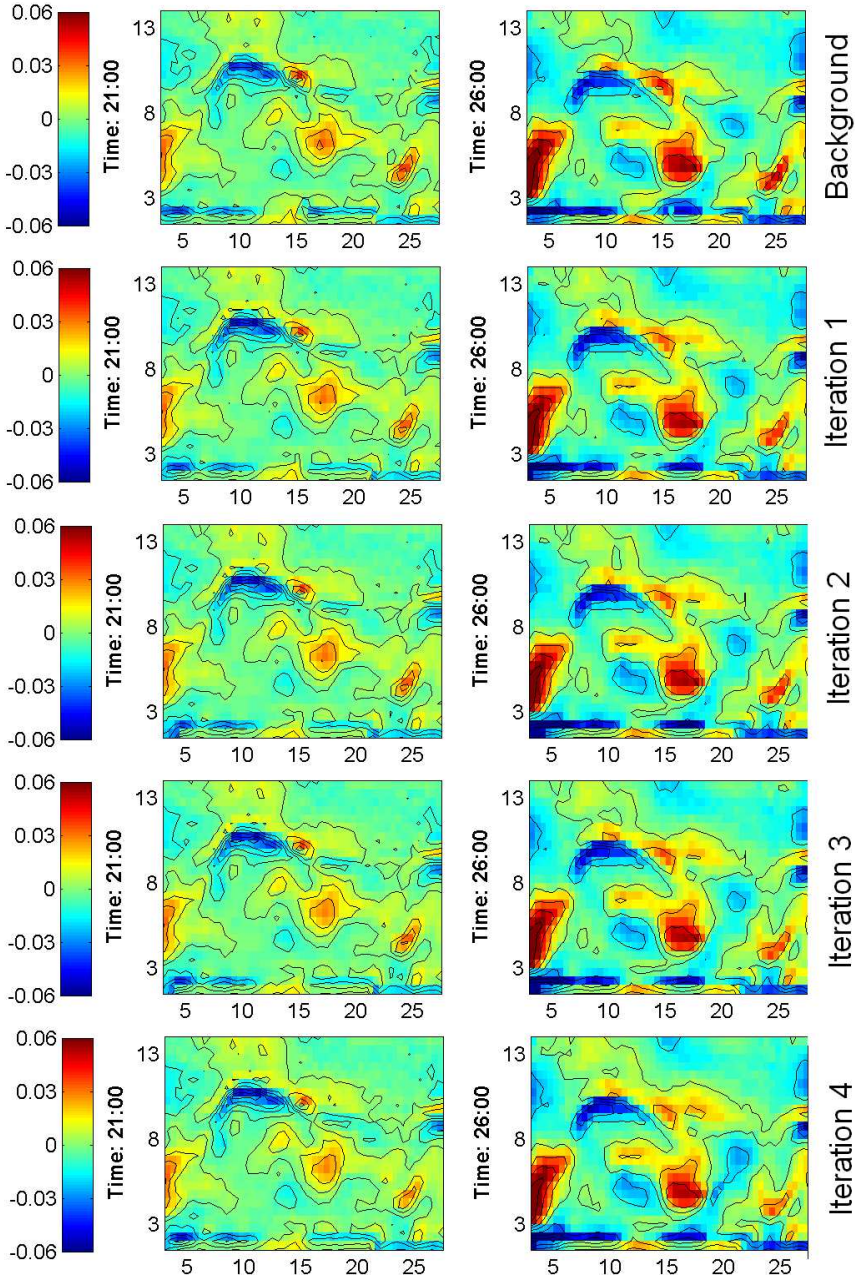


Figure 6.7: **Experiment RBB**: Difference between the morphodynamic model and the observations ($model - observations$) for the four updates. Positive values (green to red) represent areas where the model predicts larger depths than measured, negative values indicate an under-prediction of the water depth.

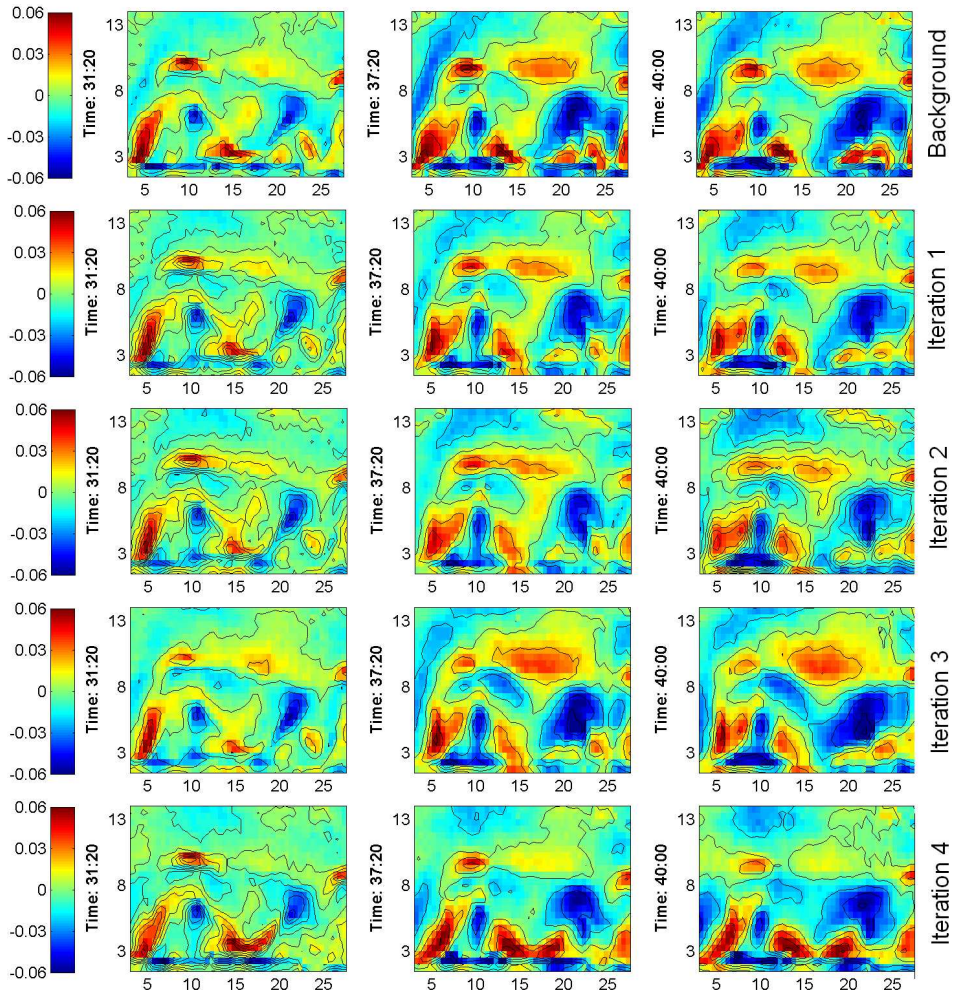


Figure 6.8: **Experiment TBR**: Difference between the morphodynamic model and the observations ($model - observations$) for the first four updates. Positive values (green to red) represent areas where the model predicts larger depths than measured, negative values indicate an under-prediction of the water depth.

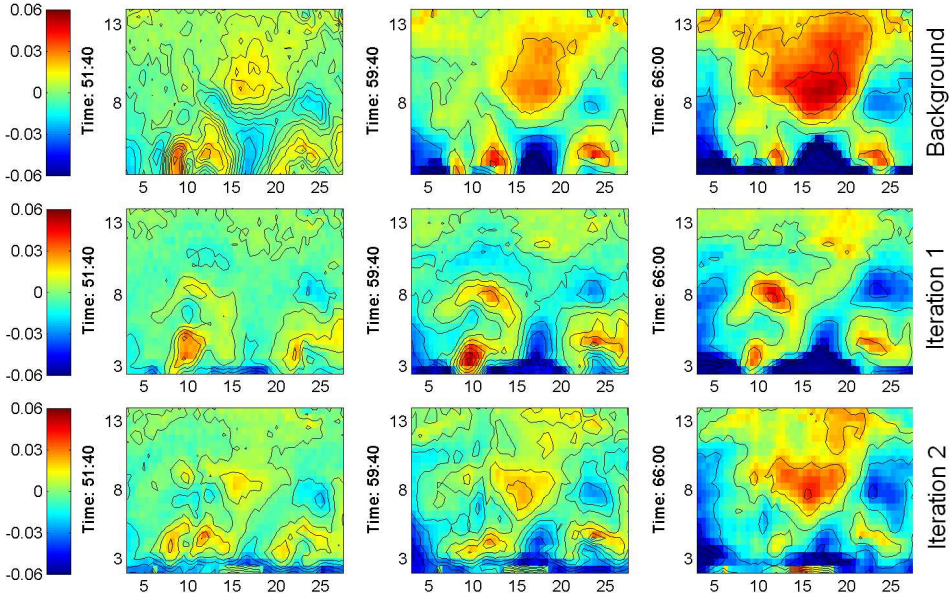


Figure 6.9: **Experiment LTT**: Difference between the morphodynamic model and the observations ($model - observations$) for each update. Positive values (green to red) represent areas where the model predicts larger depths than measured, negative values indicate an under-prediction of the water depth.

66:00; at time 51:40, on the other hand, the model shows an increase in the error. Again the trade-off between performance in the shallow areas and in the deeper areas is observed by comparing the performance of the model at time 66:00 for iterations 1 and 2. Nevertheless the rmse actually had a small increase in the process.

6.3.2 Parameter sets

Figure 6.10 shows the parameter changes relative to the standard deviation for each experiment. The changes have been normalized (see the standard deviation in table 6.2) to avoid scaling issues.

The estimation process for the transition between LBT and RBB beach states show considerable changes in viscosity, diffusivity, drying and flooding factor and the wave properties. The wave direction, in particular, is changed in the order of two standard deviations, suggesting that the model has trouble reconstructing the proper alongshore current for perpendicular wave incidence. The decrease of the roughness coefficient in the u-direction should lower the bed shear stresses close to the shore where the alongshore current is dominating. These two changes explain the improvement of the model performance in the shallow area just in front of the shoreline. In general, the parameter changes result in a reduced sediment transport. A significant decrease

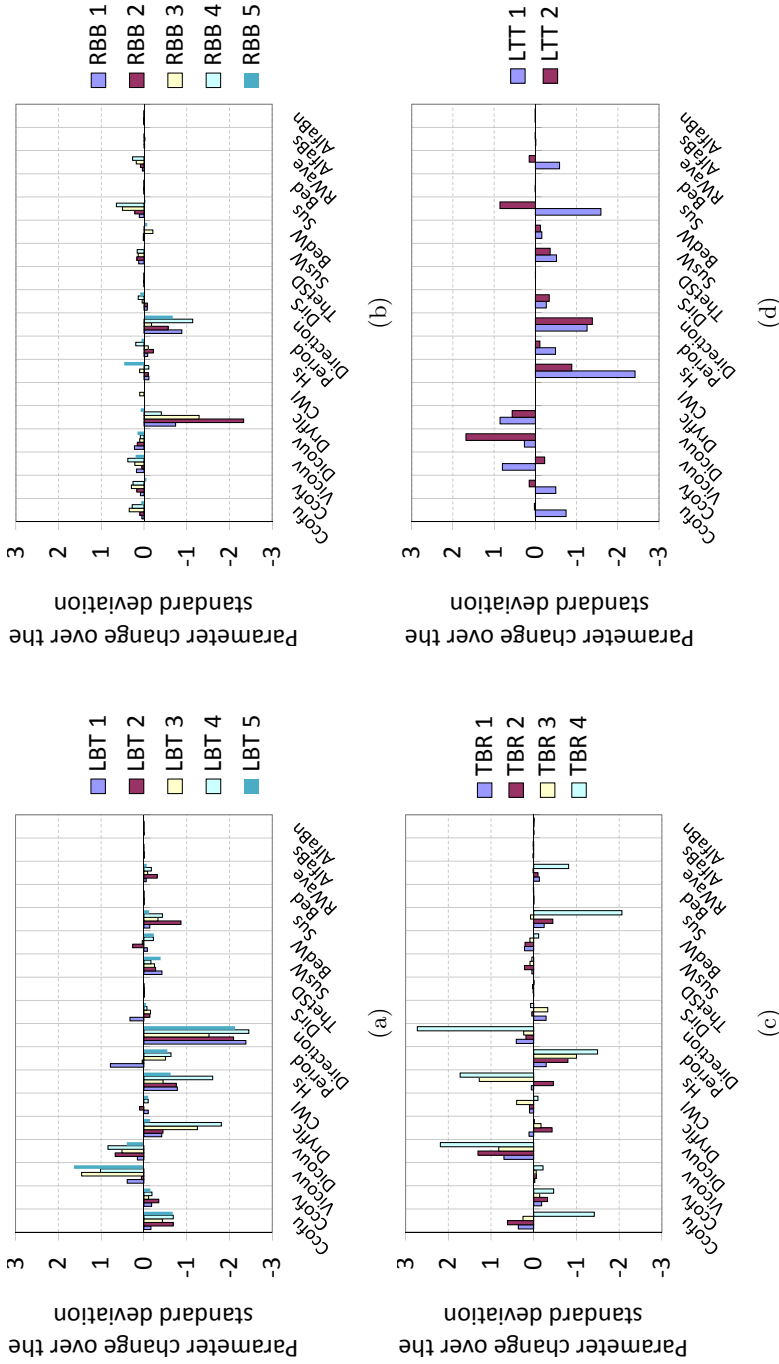


Figure 6.10: Parameter changes for each optimization iteration: (a) Experiment LBT, (b) Experiment RBB, (c) experiment TBR and (d) Experiment LTT

of the significant wave height and peak period considerably lowers the wave energy flux in the system, lowering the pickup and transport of sediments due to waves. Furthermore, the current related energy is dissipated faster by means of a higher viscosity. Finally, the decrease of the factors for suspended sediment transport ($SusW$ and Sus) considerably lowers the model dynamics. Consequently, the erosion rates in the deep area are considerably diminished and the deposition rates in the shoreline area are increased. The sign of the changes is consistent in all the iterations for most of the parameters. The evolution shows significant changes in the parameter set from iteration to iteration. Despite these changes, the morphodynamic behavior is not showing important variations (stable rmse and objective function).

For the transition from RBB to TBR states, the changes are significantly smaller than those observed in the rest of experiments. Nonetheless, the threshold for drying and flooding and the wave direction are changed in the order of one standard deviation as the estimation process takes place. Notice that after the second iteration the absolute change of the drying and flooding parameter is progressively decreased. The roughness coefficients follow a very similar behavior. A considerable increase in the wave significant height is observed in the fifth iteration. The increase in the wave height may explain why the suspended sediment transport factors (SUS and $SUSW$) are no longer increased in the fifth iteration. An increase in the sediment transport process is necessary, and it is achieved either by increasing the suspended sediment transport factors (as seen in the first four updates) or by increasing the wave significant height (as seen in the fifth update). The last update is interesting in the sense that it achieves the lowest cost function by only significantly modifying the wave direction of incidence and the wave height.

The first two iterations of the estimation of the transition from TBR to LTT states, show a significant increase of the eddy diffusivity coefficient and a decrease in the wave peak period. Less substantial changes are observed in the roughness coefficients, the threshold for cell drying and flooding, the factor for suspended sediment reference concentration and the wave significant height. In the third iteration there is a significant increase in the objective function which is probably explained by an unexpected increase of the wave significant height. Interestingly, this change is not reversed in the next iteration. In fact, it gets intensified and triggers drastic changes in other parameters. To compensate for the increased wave height, the wave period is lowered considerably along with the factor for suspended sediment reference concentration, the roughness coefficients and the wave related roughness ($RWAVE$). These changes show a very positive impact in the deep zone area but produces difficulties in the breaking zone where the excess energy intensifies the model errors. Notice that analysis 3 appears to have a positive effect in the deep area at time 31:20 and that analysis 4 considerably enhances the simulation in the same zone at all observation times. Curiously, the morphodynamic behavior in the deeper area appears to be considerably better parameterized with analysis 4 than with analysis 2. The evolution of

the changes also shows the correlation between the morphodynamic parameters. Also surprising is that the factors for wave related sediment transport (*SusW* and *BedW*) are hardly changed in analysis 3 and 4; this suggests that they have an undesirable effect in the deep area where the gain is taking place.

Experiment LTT shows significant changes in the viscosity and the diffusivity. Notice that the wave characteristics are consistently decreased. This, along with the considerable decrease of the factor for suspended sediment transport (*Sus*) and the increase of the viscosity, suggests that the estimation process is lowering the energy available in the system. As in the case of experiment LBT, there is a negative change in the wave direction (this is also observed in experiment RBB) as well as in the roughness coefficient in the *u*-velocity direction. It is worth noting that for analysis 1 the changes in the wave related roughness is observed (*RWAVE*) as well in the factor for suspended reference concentration (*Sus*) are very similar to those observed in analysis 4 of experiment TBR. The effects of these two changes seem to produce (as in experiment TBR) a considerable improvement in the deep areas of the morphodynamic model (see figure 6.4).

6.3.3 Model sensitivity to parameters

The model sensitivity measures the magnitude of the changes in the model output caused by a change in an input parameter. High model sensitivity to a parameter indicates that small perturbations in the parameter value result in significant changes in the model output. On the contrary, low model sensitivities indicate that the model output is changed only when input values are modified considerably. Mathematically, the model sensitivity to input parameters is estimated as the model derivative with respect to the parameter of interest. Figure 6.11 shows the model sensitivities to the parameter set. To take into account the difference in orders of magnitude of the different parameters, the model sensitivities have been multiplied by the standard deviation of each input parameter. In this way, the results may be compared in a straightforward manner. The columns in the figure correspond to the four experiments and each row presents the model sensitivity to one of the input parameters. The vertical axis of each graph shows the mode number (1 to 40), being 1 the most important and 40 the least important in terms of energy. The horizontal axis of each graph shows the simulation time.

For the first three experiments (LBT, RBB and TBR) similar parameter sensitivities are observed. The horizontal eddy diffusivity, wave-related suspended sediment transport factor, horizontal eddy viscosity and suspended sediment reference concentration appear to be the most relevant parameters, followed by the wave characteristics and the roughness coefficients. For experiment LTT (LTT state development) the importance of the hydrodynamic parameters is significantly lower. At this stage, the wave-related suspended sediment transport factor has the highest sensitivity, followed by the horizontal eddy diffusivity, the threshold depth for drying and flooding,

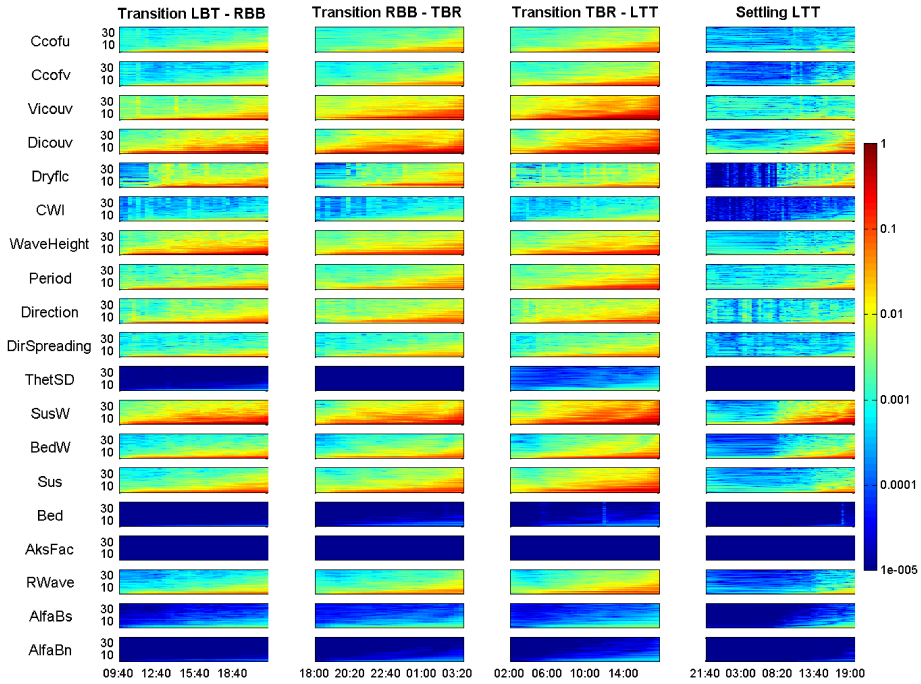


Figure 6.11: Model sensitivities to the parameter set. Each line of graphs shows the model sensitivity to the parameter specified on the left hand side of the line. The vertical axis of each graph shows the mode number (1 to 40), being 1 the most important and 40 the least important in terms of energy. The sensitivity value has been rescaled with the standard deviation of each parameter to take into account its order of magnitude.

the suspended sediment reference concentration factor and the wave-related bed-load sediment transport factor.

The temporal change of the model sensitivities is clearly observed for each transition phase and parameter. As in most mathematical models, parameter sensitivities show a gradual buildup in time. The sensitivity is equal to zero in all experiments for the parameter *Aksfac*; which relates to Van Rijn's reference height. This is not surprising as the model only takes into account this parameter depending on the value of the water depth, the estimated ripple factor and the current-related effective roughness height (see [Deltares, 2009a](#), 348-349). Notice how the factor for erosion in adjacent dry cells (*ThetSD*) increases in importance over experiment TBR. At this stage the evolution of the rip channels takes place and the shallow shoals attach to the beach [Michallet et al. \(2013\)](#). Naturally the beach erosion parameter plays an important role at this stage.

The graphs show the influence that each parameter has on each projection mode. The importance of each mode decreases as the mode number increases. The *transmission* of the sensitivities from mode to mode takes place sequentially. The most important mode is the first to be affected by parameter changes, then the second most important and so on until the complete subspace is sensitive to changes in the parameters. For the TBR to LTT transition the increase and *transmission* of the model sensitivities take place at a higher rate. By the end of the model simulation, the complete subspace is being affected by the horizontal eddy diffusivity and viscosity, and the wave-related suspended sediment transport factor. This clearly shows how the morphodynamic evolution increases in complexity.

The results suggest a complex interaction between the hydrodynamic and the morphodynamic components of the system. The low sensitivity at initial simulation times suggests that the morphodynamic system is more sensitive to the initial bathymetry at this point. Nevertheless, a detailed analysis is necessary to evaluate the extent and significance of the model sensitivity to the initial bathymetry.

6.4 Discussion

A model reduced 4DVar assimilation scheme has been successfully implemented. The results presented here suggest that the evolution of the morphodynamic system cannot be easily captured by parameters that are constant in time, it is necessary to consider some of the parameters as time dependent. Also, further analysis is necessary to evaluate the effects of using a 2D depth averaged morphodynamic system. Furthermore, the gradual buildup of sensitivities in time for the different projection modes suggests that for the case of parameter estimation the rank of the problem gradually increases as the simulation time increases.

The morphodynamic model seems to lack the necessary physics to reproduce some of the features observed in laboratory experiment. The observed trough ($(x, y) \approx (10, 8.5)$ and $t = (15 : 40 - 31 : 20)$), in particular, is not being generated by the model despite it being incipient in the first observation (9:40). A possible explanation of this model limitation is given by [Ranasinghe et al. \(2004\)](#). According to them, for the generation of such features a 3D morphodynamic model that takes into account the vertical components of the velocity field. The model also fails to produce accurate deposition and erosion rates to match the observations in both deep and shallow areas simultaneously. Without the trough, the subsequent morphodynamic evolution diverges considerably from the observations. This behavior might be solved by implementing a full 3 dimensional model or by including a state estimation along with the parameter estimation scheme. Aside from that, the increase in the wave direction of incidence causes an increase in the along shore current, which is controlled by a considerable increase of the bed roughness (in terms of a decrease of the Chezy coefficient) in the U direction. The increase of the eddy diffusivity and of the wave

significant height causes an increase in the sediment transport. Consequently the factor for suspended sediment transport factor is lowered considerably to account for the additional wave-energy.

The results suggest that the morphodynamic model performs differently in shallow areas than in deep areas. As the performance of the shallow areas is improved, the errors in the deeper areas increase. Other attempts to optimize morphodynamic model performance (Serafy et al., 2011) have reached the same conclusion. Further research is necessary to assess the causes of this phenomenon. A possible explanation could be the difference in process scales if deep and shallow physical processes.

Chapter 7

Estimation with time exposure (Argus) images

In this chapter the *ensemble model order reduction* (enMOR) is implemented for a morphodynamic model of Egmond aan Zee, The Netherlands. As described in 3 enMOR constructs a reduced order model via an optimization process instead of the more conventional finite difference approach (see chapter 3). In chapter 6, a partial implementation of the enMOR was shown where only the directional derivatives were estimated with the alternative method. Here the enMOR as presented in chapter 3 is implemented and tested. The objective is two fold. The first objective is to assess the performance of the proposed method for data assimilation purposes. The second objective is to evaluate the feasibility of using time exposure images for assimilating data into a morphodynamic model.

The implementation of an operational data assimilation scheme for a real study case is challenging in various ways. Time exposure images measure roller dissipation in an indirect manner. For a detailed explanation on how the roller energy dissipation is computed from time exposure images, the reader is referred to the work of [van Dongeren et al. \(2008\)](#). The estimation process assumes that the wave energy is completely dissipated in the breaking zone, and that pixel intensity is a measure of the amount of dissipation that is taking place in the corresponding area. By knowing the wave dominant conditions the total roller energy can be estimated and the way in which it is dissipated in the breaking zone is given by the observed pixel intensity changes. In connection to measurement errors, the implications of these assumptions are difficult to quantify. Bear in mind that the image used in the process is a composition of several time exposure images. This involves several geometric transformations in which error estimation is not easily accessible. Posterior error estimation is also difficult because energy dissipation cannot be measured directly. To the author's knowledge there is

no work that addresses this issue. Uunk et al. (2010) make an attempt to estimate the bathymetric uncertainties for values derived from time exposure images and van Dongeren et al. (2008) use ad-hoc error definitions for their data assimilation method (Beachwizard), but a detailed analysis on how the measurement errors propagate as the dissipation is estimated is missing.

7.1 Study area

Egmond aan Zee is a wave dominated system located in the dutch province of North Holland. It is part of a long continuous system of sandy beaches and multiple barred coastal areas (Short, 1992; Wijnberg et al., 2004). Its morphology is characterized by a shore parallel double/triple sandbar system with a beach slope of about 1:30 (Kroon, 1991; Short, 1992). Its sediments are well sorted medium to fine sands ($d_{50} \approx [200, 300] \mu m$). The average offshore wave climate consists of waves with a mean annual height of 1.3 m and a peak period of 5.7 s. The tide is semi-diurnal and has a mean tidal range of 1.2 m (neap tide) to 2.1 m (spring tide). A more detailed description of the system can be found in the works by Short (1992); Aagaard et al. (2005).

7.2 Numerical model

A three dimensional morphodynamic Delft3D model was used to simulate the study site. As in previous sections, the SWAN wave simulator was used to reconstruct the wave conditions and the Delft3D suite was used to reconstruct the hydraulic and morphodynamic processes of the study area. The model characteristics are similar to the ones used in Briere et al. (2011) for the estimation of roller parameters. The hydrodynamic model uses a grid of 66 cells across-shore by 141 along-shore by 12 layers vertically. The grid covers a 1300 m (cross shore) by 5600 m (along shore) area. The wave model is using a coarser grid with 81 by 134 gridcells covering an area 7000 m (along shore) long by 1500 m (cross shore) wide.

The model configuration used by Briere et al. (2011) was used in the background simulation of the data assimilation scheme. A 10.5 hours simulation was implemented to reconstruct the system's evolution between 00:00 and 10:30 of the 7th of August of 2013. The wave and flow modules are coupled on-line and they communicate every 30 min of hydrodynamic simulation to keep the wave conditions updated according to the hydrodynamic and morphodynamic evolution. The hydrodynamic simulations start at 00:00, and include a 4 hour spin up time where no morphodynamic updates take place. From 4:00AM until 11:00AM a full hydro-morphodynamic simulation takes place.

The available wave properties are adjusted time dependent observations from the close-by Ijmuiden buoy. The adjustment was done with a coarser Delft3D flow model

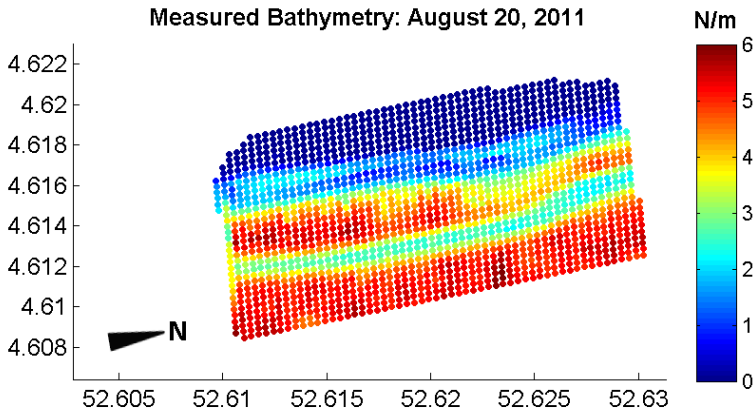


Figure 7.1: Measured bathymetry at Egmond aan Zee on the 20th of August of 2011

to take into account the changes due to the distance between the station and the study site. Measurements of wave direction of incidence, significant height and peak period are available every hour.

A set of water depths measurements is available from the 20th of August of 2012, just two weeks after the time exposure images were taken. The water depth observations cover most of the modeled domain with a high non-homogeneous spatial resolution. The measured water depths were interpolated to the model grid and were used as the initial bathymetry for the hydrodynamic simulations. In figure 7.1 the observed bathymetry (20th of August) is shown. The bed consists of a homogeneous layer of sand with a median diameter of $280 \mu\text{m}$ and a specific gravity of 2650 kg/m^3 . Two Neumann type boundary conditions were prescribed for the north and south model boundaries. On the open sea boundary the water levels are specified according to the tidal conditions of the study site. The wave forcing has only been prescribed at the open sea boundary. A time step of 12 seconds is used for the hydrodynamic estimation.

7.3 Observations and Observation Operator

The Egmond aan Zee Argus system is composed of 5 high resolution cameras located on the J.C.J van Speijk lighthouse. It was first installed in 1999 for coastal zone management. Lately, efforts have been made to enhance the quality of the image composition and post-processing techniques within the development of the CoSMoS prediction system (van Dongeren et al., 2013). A set of time exposure images taken during August 2011 with variable temporal coverage is available. August 7th is the day with most observations with 10 images available at, 6:00AM, 7:00AM, 7:30AM, 9:30AM, 10:00AM, 10:30AM, 11:00AM, 11:30AM, 12:00M, and 12:30AM. Based on

these time exposure images, roller energy dissipation maps have been produced (van Dongeren et al., 2013). The analysis shown in this chapter uses part of this data, namely the observations at: 7:30AM, 9:30AM, 10:00AM, and 10:30AM.

The spatial domain of the observations covers a 2800 m along shore by 1300 m cross shore area. The spatial resolution is significantly higher than the one of the model, with a dissipation measurement every 20 m in the along shore direction and every 5 m in the cross shore direction. To match the model estimations and the observations, a linear observation operator that estimates a weighed average of the six nearest observations to each model result is used. The weights are given by the distance between the measurement and the model result. The error of the dissipation estimations is assumed constant and equal to $20N/m$, this estimation was provided by experts.

7.4 Roller energy dissipation in Delft3D

Since the observations used for the analyzes presented here are of roller energy dissipation, a brief explanation on the computation of this quantity will be presented. Roller energy dissipation data is not an output of Delft3D; nevertheless, all the necessary information to compute it can be read from the wave and flow output files. The operator to calculate the roller energy dissipation, D_r , is given by,

$$D_r = (2g\beta_r)E_r/C_w, \quad (7.1)$$

$$(7.2)$$

with $C_w = W_L/T_p$. The wave front slope (roller slope) is given by β_r , E_r is the roller energy, and C_w , W_L and T_p stand for wave celerity, wave length and wave peak period, respectively. All these variables can be found in the output files for each model grid cell at each saving time.

The roller energy in Delft3D is computed by solving the stationary balance equation given by,

$$\frac{\partial}{\partial x} (2E_r C_w \cos\theta) + \frac{\partial}{\partial y} (2E_r C_w \sin\theta) = D_w - D_r, \quad \text{with} \quad (7.3)$$

$$D_w = 0.25\alpha_r \rho_w g f_p \exp\left(-\frac{H_{max}}{H_{rms}^2}\right) (H_{max}^2 + H_{rms}^2), \quad \text{and}$$

$$H_{max} = \frac{0.88}{k} \tanh\left(\frac{\gamma_w}{0.88} kh_{ref}\right).$$

Here the short wave dissipation is represented by D_w , x and y stand for horizontal coordinates, θ is the wave direction of incidence, α_r is a user defined factor that controls the wave height along the cross-shore profile (high values of α_r imply lower values of wave height), ρ_w is the water density, g is the gravitational acceleration, f_p is the spectral peak frequency, H_{rms} and H_{max} are the root mean square wave height

and the maximum wave height respectively, k is the wave number, h_{ref} is water depth, and, lastly, γ_w is a user defined parameter that controls the wave height in the surf zone by imposing a maximum wave height in terms of the water depth.

7.5 Implementation and Results

The analysis of the results focuses on the performance of the proposed method for data assimilation and the feasibility of using time exposure images for assimilating data into Delft3D. From the available observations, only the 7:30AM roller dissipation map was assimilated into the model, the rest of the observations were used to assess its prediction skills. The idea is to assess to which extent the scheme and the model are able to find a reasonable parameter set capable of reconstructing the observation at 7:30AM. Regarding the prediction skills of the model, they are assessed by evaluating the cost function at later observation times (9:30AM - 10:30AM).

The estimation parameter set consists of 13 model parameters out of which 2, the wave significant height and the wave peak period, are time dependent. These two parameters are in fact vectors consisting of 4 elements each; one every hour between 4:00AM and 7:00AM. The parameters and their background (prior) values are presented in table 7.1 (See *Parameters* and *Background*). Notice that the bathymetry is not part of the state and therefore is not directly estimated in the estimation process. Instead, it is updated indirectly by changing the parameters shown in table 7.1.

As in the case of model reduced 4D-Var the implementation of the data assimilation scheme consists of three main steps: (1) principal component analysis, (2) model order reduction and (3) assimilation of observations. An ensemble of 45 model executions was used for the principal component analysis and the model order reduction. The ensemble includes a *background simulation* with the initial parameter set (see *Background* in table 7.1), and 44 perturbed simulations where a normally distributed ($N(0, \sigma^2)$) random noise has been added to each parameter. The standard deviations, σ , used for the additive noises are presented in table 7.1 (see *Standard Deviation*). From these 44 model simulations 4 crashed due to various reasons; thus, the available ensemble size is 40. All (40) ensemble members were used for the estimation of the ROM. To focus the efforts on the highly dynamic areas, observed dissipation values lower than 3 N/m were not taken into account in the data assimilation process. Given the number and order of magnitude of the innovations, the background term (first term in the right hand side of equation 2.8) has a very small contribution in the calculation of the cost function. For this reason, in the minimization process the background value was multiplied by a factor equal to $1e-5$ times the sum of squares errors between the model (without update) and the observations. The main objective of this rescaling is to keep the minimization from accepting nonphysical values.

A rank-20 ROM was used for the data assimilation process. The subspace of the ROM preserves 47.2% of the total energy. For higher energy thresholds, the size of the

1. Estimation parameters and data assimilation results				
Parameters	Background	Standard Deviation	Analysis	Analysis
Chezy roughness coefficient (U direction) [$\sqrt{m/s}$]	55.0	10	71.136	71.136
Horizontal eddy viscosity [m^2/s]	1.0	2.0	7.626	7.626
Horizontal eddy diffusivity [m^2/s]	1.0	2.0	7.581	7.581
Vertical viscosity [m^2/s]	1.0e-005	0.0001	1.0e-005	1.0e-005
Vertical diffusivity [m^2/s]	1.0e-005	0.001	1.0e-005	1.0e-005
Wave breaking index [-]	0.7	0.02	0.735	0.735
Roller slope [-]	0.05	0.05	0.0513	0.0513
Breaker delay* [m or m/s]	0	0.5	4.496	4.496
Wave significant height (4:00) [m]	1.37	0.02	1.278	1.278
(5:00) [m]	1.51	0.02	1.691	1.691
(6:00) [m]	1.47	0.02	1.467	1.467
(7:00) [m]	1.49	0.02	1.463	1.463
Wave peak period (4:00) [s]	4.5	0.2	4.491	4.491
(5:00) [s]	4.6	0.2	4.576	4.576
(6:00) [s]	4.4	0.2	4.399	4.399
(7:00) [s]	4.2	0.2	4.202	4.202
Wave suspended sediment transport factor [-]	0.5	0.2	0.748	0.748
Suspended sediment reference concentration factor [-]	1.0	0.3	1.0	1.0
Wave related roughness [m]	2.0	0.5	3.709	3.709
2. Objective Function Values				
7:30AM	11643.57	-	10799.59	10799.59
9:30AM	21240.75	-	19681.99	19681.99
10:00AM	22291.44	-	19567.89	19567.89
10:30AM	16851.53	-	13596.80	13596.80

Table 7.1: Initial state, standard errors and data assimilation results.

* The units depend on the value of the parameter. If it is negative, the parameter represents a weighted depth and is therefore in meters. If it is positive, the parameter represents a weighted stokes drift and is therefore in m/s

Wave conditions for prediction			
	<i>8:00</i>	<i>9:00</i>	<i>10:00</i>
Hs [m]	1.31	1.53	1.80
Tp [s]	4.00	4.10	4.40

Table 7.2: Wave conditions used for predicting roller energy dissipation from 8:00 until 13:30.

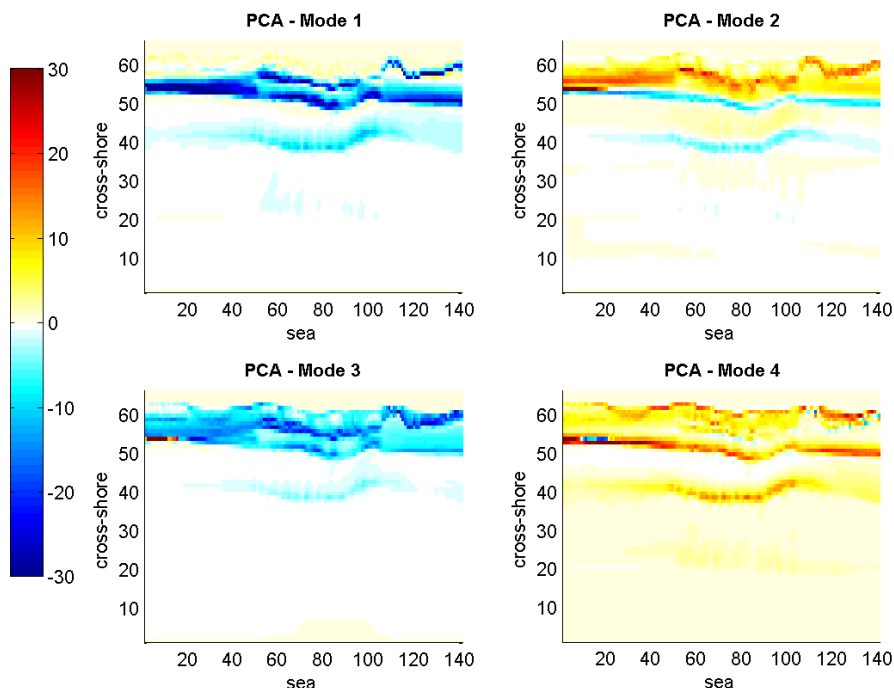


Figure 7.2: Results of the principal components analysis: projection sub-space used for the reduced order model.

reduced order model becomes too high. With 99.9% of the energy, for example, the rank of the subspace is equal to 754, making the model order reduction too onerous. The first four modes (12.3%, 6.3%, 4.3%, and 2.9%) of the principal components analysis are presented in figure 7.2. All four modes show three high dynamic bands (high absolute values in the map) consisting of the two bars and the shoreline area. The higher intensities along the inner bar and the shoreline suggest that the model is considerably more sensitive to parameter changes in these areas than along the outer bar.

Figure 7.3 shows the cost function of the background (red with triangle) and of the analysis (blue with square) at all observation times. The values of the cost

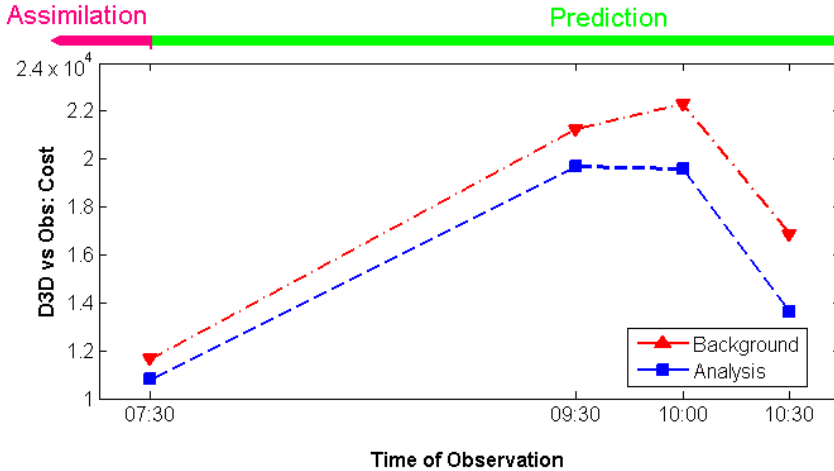


Figure 7.3: Objective function for predictions.

function are also presented in section 2 of table 7.1 (see under *Objective function values*). The difference in the cost function at 7:30AM is the result of the optimization procedure, whereas the values at: 9:30AM, 10:00AM and 10:30AM, correspond to the performance of the background and analysis for predicting the roller energy dissipation. A significant improvement is observed in all cases. A reduction of 7.2% with respect to the initial cost function is obtained at the assimilation time (7:30AM) and improved predictions are obtained at later times: 7.3%, 12.2%, and 19.3% (see section 2 in table 7.1) at 9:30AM, 10:00AM, and 10:30AM, respectively.

Significant changes in the parameter values are observed, see table 7.1. In particular, the wave breaker delay is increased significantly (almost 9 times its standard deviation). The breaker delay parameter controls the position in which the wave breaking process starts and stops. It has been observed that there is a delay in the order of a wave length before the waves actually start or stop breaking. When the breaker delay is positive the delay is implemented by replacing the mean Stokes drift at the position of interest with a Stokes drift weighted over a certain distance seaward. The change of this parameter translates into a significant displacement of the breaking zone shoreward. Additionally, the horizontal eddy diffusivity and viscosity are also considerably increased in the analysis. These changes along with the increase of the wave related roughness and the wave suspended sediment transport factor make the system more energy dissipative and considerably enhance the material transport. This translates into a different morphodynamic evolution. Figure 7.4 shows the bathymetric differences between the background and the analysis simulations at observation times. Most of the differences in the morphodynamic evolution of the system take place over the bars and in the surf zone. The blue tones represent areas where the bathymetry

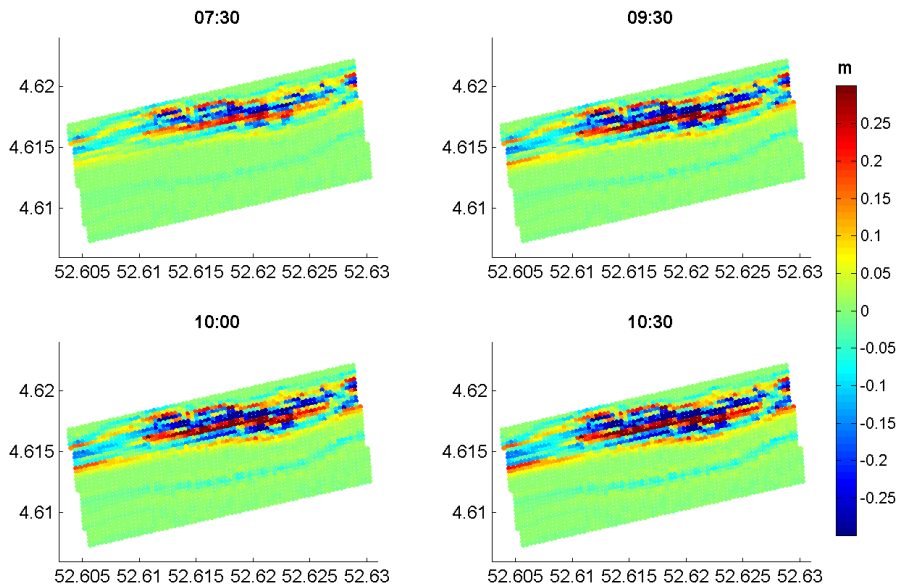


Figure 7.4: Bathymetric differences between the background and the analysis model simulations at the observation times. Negative values represent areas where the analysis is deeper than the background.

is deeper in the analysis than in the background, while the red tones represent the converse. Both the outer and the inner bars are being flattened in the analysis while considerable deposition is observed in the surf zone; specially shoreward from the inner bar. The spatial pattern in which the bathymetric changes are taking place seem to be constant in time, i.e. only the intensity of the changes is varying in time. The constant improvement in the cost function in the prediction phase might be closely related to this change in the morphodynamic evolution but the influence of each of the parameters is difficult to asses. More analysis is necessary to assess the implications of the changes in the parameter set.

The effects of the data assimilation at 7:30AM is shown in figures 7.5 and 7.6 (upper-left panel). The upper panel of figure 7.5 shows the dissipation map coming from the time exposure image, while the central and lower panels show the reconstructed dissipation from the background and the analysis simulations, respectively. The measurements show considerably higher roller energy dissipation values over the outer bar than the model. In the surf zone, the background simulation shows a very localized and intense energy dissipation over the inner bar and close to the shoreline (see central panel), while the observations show a lower dissipation intensity on these two areas. This difference could be partly explained by the model's underestimation

of the energy dissipation over the outer bar area. Nevertheless, the differences observed at the southern part of the beach (between 52.6° and 52.61°), where the effect of the outer bar is negligible, suggest that either the model is overestimating the total amount of roller energy, or the dissipation maps coming from the time exposure images are underestimating it.

The data assimilation effects on the simulation is mainly observed as a decrease of the dissipation values over the inner bar and the shoreline (compare the central and the lower panels of figure 7.5). Notice that the spatial distribution of the map is not significantly changed. The effects of the inner bar between 52.61° and 52.62° are largely underestimated in the model simulations which causes the dissipation to take place at the shoreline. This suggests that the bathymetry used in this area differs considerably from the real one. Between 52.62° and 52.63° the observed features are better reconstructed by the model and the effects of the data assimilation in reducing the dissipation values are significant.

The upper left panel of figure 7.6 shows the histogram (empirical distribution) of model deviations with respect to observations at 7:30AM. The background simulation underestimation of energy dissipation in the outer bar and in the surf zone is observed as a bias in the distribution. On the other hand, the background overestimation (negative deviations) at the inner bar and shoreline area is observed as the fat negative tail of the distribution. A significant decrease of the background bias (represented by the shift in the mode) is observed in the analysis. The over estimation is also improved but the asymmetry of the deviation's distribution is still observed in the analysis.

Figure 7.7 shows the energy dissipation maps at the prediction times. Notice that in all cases the background simulation shows high dissipation values concentrated along two narrow bands over the inner bar and the near shoreline areas. These two bands can also be identified in the observations but in this case the overall dissipation takes place over most of the surf zone rather than at the inner bar and the shoreline. Regarding the outer bar both the background and the analysis simulations are able to reconstruct the observed temporal variations and the changes in magnitude. Interestingly, the total dissipation presented in these observations is considerably higher than that observed at 7:30AM; to the point that the model seems to be underestimating the total roller energy in the system. This drastic increase of roller energy dissipation is not observed in the simulation results suggesting that it is not caused by changes of the prevailing wave conditions. The differences could be related to the quality of the time exposure images (e.g. low contrast) or the estimation of the dissipation maps.

Regarding the data assimilation process, its main observed contribution consists of increasing the area over which the dissipation is taking place. This has the double effect of lowering the values over the narrow bands where the background simulation overestimates the dissipation and increasing them in the rest of the surf zone where they were being underestimated. These changes are more clearly observed in figure 7.6 (upper-right and lower panels). The overall distribution of the deviations is very

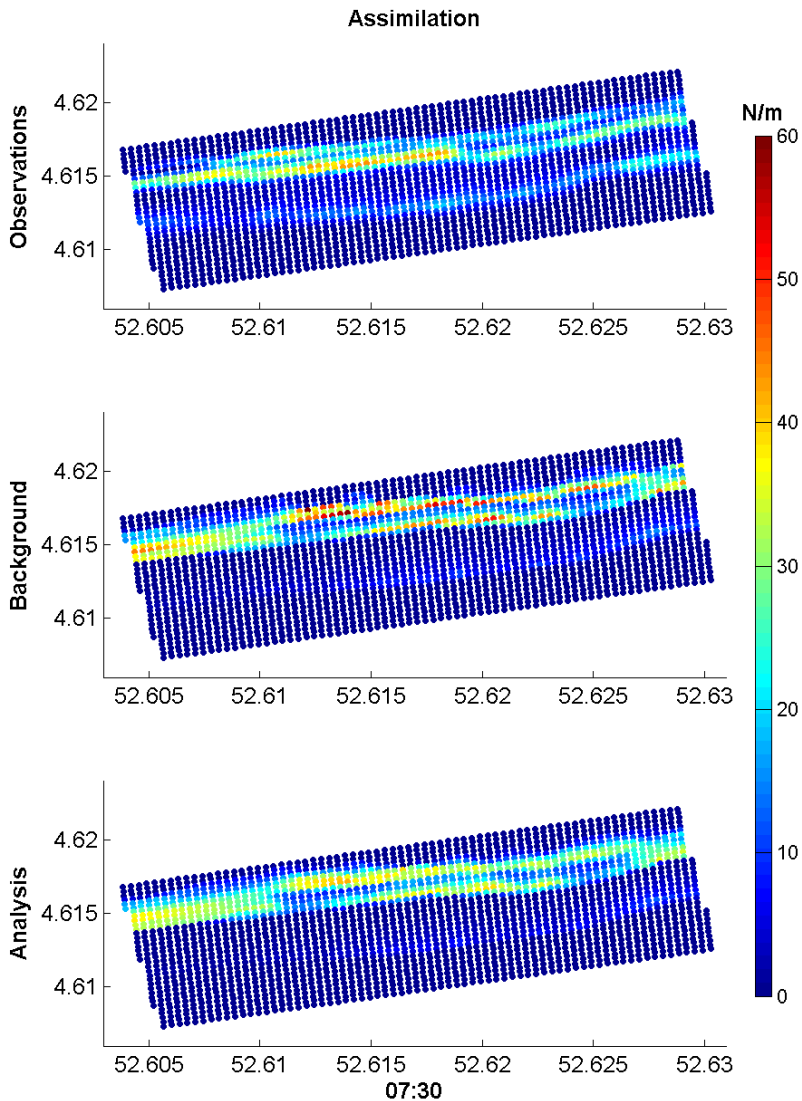


Figure 7.5: Observed and simulated dissipation maps at 7:30AM. Upper panel: Roller energy dissipation measurements derived from time exposure images. Central panel: Roller energy dissipation map estimated with the background model. Lower Panel: Roller energy dissipation map estimated with the analysis model.

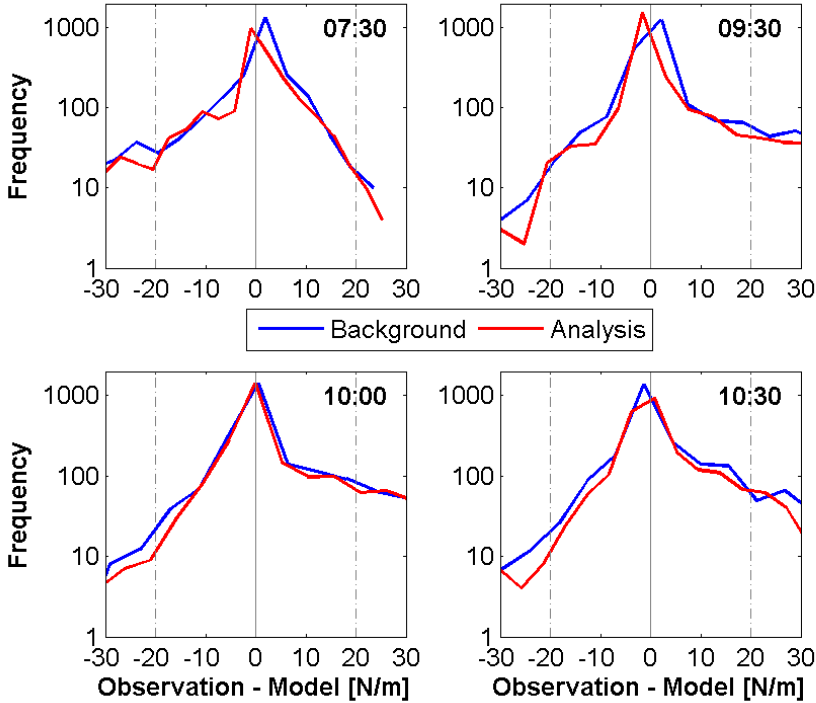


Figure 7.6: Histogram of model deviations from observed values (observed minus modeled). The *frequency* refers to the number of deviations at each threshold. The gray dashed lines mark the observations standard error. Negative deviations represent model overestimation.

similar in all prediction times. In contrast with the distribution at 7:30AM, the rest of the histograms show a significant positive tail suggesting that the models are underestimating high dissipation values. This is explained by the change in total roller energy observed in the measured dissipation maps at 9:30AM and later. Notice that the high negative deviations (< -20) quickly drop below 10.

At 9:30AM, the improvements due to the data assimilation are similar to the ones at 7:30AM. While the background deviation distribution has a slight positive bias (underestimation) the analysis shows a slight negative bias. The analysis' tails on the other hand show a significant improvement over the background. At 10:00AM the models seem to be unbiased and the main gain of the data assimilation consists of decreasing the number of negative deviations while very little is achieved regarding the positive ones. At 10:30AM the background deviations show a slight negative bias which is corrected in the data assimilation. Additionally, significant improvements in

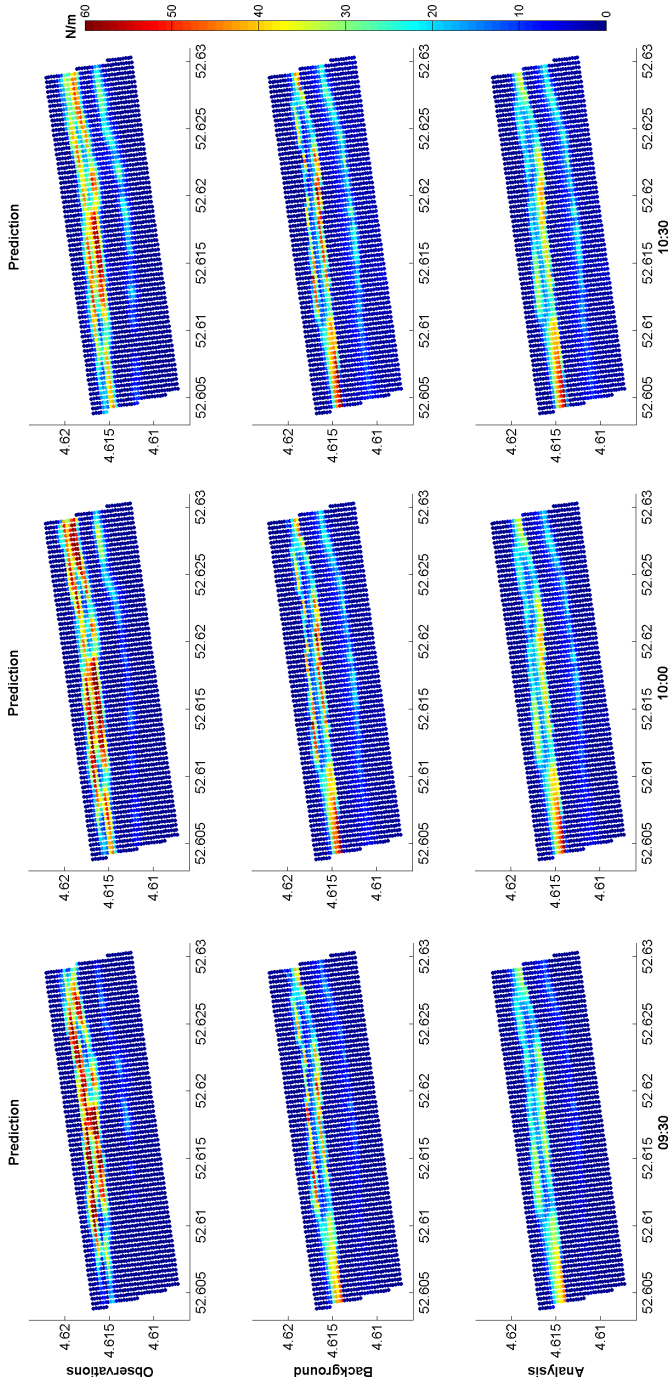


Figure 7.7: Dissipation maps before and after assimilating roller dissipation maps coming from the Argus system into delft3D. In this assimilation, the unfiltered time exposure image was used. A ROM of 5 modes, estimated from 40 ensemble members was used.

both the negative and the positive tails are observed.

In general, the analysis seems to be able to correct the biases observed in the background simulation and significant improvements are achieved in the tails of the distributions of the deviations. This is especially observed in the surf zone between 52.61° and 52.625° , where the analysis results in a considerably smoother dissipation map (compare, for instance, the analysis and the background at time 9:30AM). Despite the notable differences in the surf zone between the background simulation and the analysis, the dissipation over the outer bar is very similar.

7.6 Discussion

The ensemble model order reduction and 4DVar proposed in chapter 3 was successfully implemented for the Egmond aan Zee morphodynamic model. For the Delft3D modeling suite, the implementation of the method proved to be more practical than the common finite difference approach. The experiment presented here aimed to test the efficiency and potential of using data assimilation to estimate a set of 13 input parameters from roller dissipation maps produced by the Argus system. The results show that the technique is able to find a parameter set that considerably improves the modeling accuracy. The ensemble model order reduction and 4DVar can be successfully used as part of operational forecasting systems of morphodynamic processes.

The model order reduction, as presented by Vermeulen and Heemink (2006), would have required additional model executions; for estimating the dynamic components (D_k) and the model sensitivity to parameter changes (S_k). These model runs should be executed in short partial simulations to produce the desired piece-wise linear approximation. These partial executions proved to be cumbersome in previous implementations. First, minimizing the effects of restarting the model requires at least 2 hours spin-up time. This implies a 2.5 hours simulation for every 0.5 hours partial execution. This means that each of the additional simulations required for the finite difference estimation is three and a half times more expensive. Additionally, model crashes/errors (such as the 4 model crashes reported previously) due to numerical issues and other events (e.g. pc errors) occur at varying rates between 2% and up to 15% depending on the model parameter or the characteristics of the mode. Aside from the numerical issues of the model execution, determining the size of the finite difference perturbation for each parameter/mode requires additional test simulations. In the case of the directional derivative for the ROM dynamic component, D_k , the perturbation size choice is particularly difficult because these perturbations are not mass conservative and often produce model instabilities. Taking all of these factors into account, the model simulations required by the Vermeulen's method usually take considerably more time than the minimization process took. From a practical point of view, the implementation presented here is considerably more efficient than the finite difference based estimation.

The morphodynamic evolution of the system is considerably changed by the changes in the hydro-morphodynamic parameter values: horizontal eddy viscosity, horizontal eddy diffusivity, wave suspended sediment transport factor, and wave related roughness. The increase of the Chezy coefficient, lowering the bed roughness, has an impact on the bed shear stress limiting the sediment entrainment. This lowers the amount of available sediment in the water column. The increase of the horizontal eddy diffusion and the wave suspended sediment transport factor increases the transport of suspended sediment, while the increase of eddy viscosity and wave relate roughness makes the system more energy dissipative. It is difficult to assess what are the practical implications of these changes in the model; a detailed sensitivity analysis is necessary to assess to which extent each parameter change is affecting the morphodynamic evolution of the system. Nevertheless, the data assimilation resulted in a more homogeneous dissipation map that is in agreement with the observed dissipation pattern. The constant cost function decrease observed in the predictions suggests that the morphodynamic evolution of the analysis has been improved. Unfortunately, there is no bathymetric data available to corroborate this. Longer simulations, where more observations are assimilated into the model and more predictions are compared with measurements, can provide more conclusive evidence about the performance of the water depth evolution of the updated model.

The model order reduction method as implemented here constitutes a significant step toward the development of a morphodynamic forecasting system. The next step should be to implement the methodology in a sequential prediction - assimilation work flow. Bear in mind, that the updated parameter vector presented here is set to modify the bathymetry to match the observation; it is not necessarily the optimal parameter combination for forecasting purposes. Several other developments and implementations that might prove useful in this and other applications. The most straightforward might be the use of the model ensemble to assess model uncertainty in a similar fashion as in ensemble Kalman filtering. This model uncertainty could be use to implement a weak constraint 4DVar with the reduced order model. Similarly, the same ensemble could be used for a second outer loop if the parameter changes are within the ensemble perturbations. Finally, an estimation of the reduced order model error with respect to the full model should be easy to estimate by comparing the capacity of the ROM to reconstruct the ensemble members. This information would be useful to implement a weak constraint 4DVar.

Chapter 8

Conclusions

The development of adjoint-free variational methods has the potential to make their implementation more practical while preserving some of the desired properties. This thesis is concerned with the combined use of model order reduction methods and variational data assimilation methods. The main objective of the work presented here consists of assessing the potential use of *model reduced 4DVar* to estimate input parameters in the field of morphodynamic modeling. Despite some implementation issues, the method has been used in a number of other fields of study and shows to be robust and consistent for parameter and state estimation. Here, its evaluation has been done through three different applications. Some model characterization analyses were done prior to the implementation of these applications. The analyses mainly consisted of testing the restart-process in Delft3D, and studying the effects of parameter perturbations in the model evolution. The results show that the restarting process produces undesirable effects on the model's evolution. Also, non-linear effects are observed even for very small parameter perturbations. With these results in mind the first application of model reduced 4DVar was implemented and consisted of a small study case with synthetic observations. The main objective of this application was to identify the implications of the model limitations (e.g. restarting process) on the implementation of the data assimilation method. The results show that the use of finite differences for the estimation of the reduced order model components constitutes a methodological weakness. In response to this problem a novel *finite-difference-free* methodology for model order reduction was proposed: *ensemble model order reduction* (EnMOR). A partial implementation of EnMOR was attempted for a set of results coming from a laboratory experiment. This second application aimed at evaluating the performance of the new method and its limitations. The outcomes of this second application show that the use of EnMOR for building the required linear approximation effectively avoid the problems associated with the finite difference approach without any detriment of the data assimilation process. Finally, EnMOR-4DVar was used

to estimate input parameters for a morphodynamic model of Egmond aan Zee by assimilating roller energy dissipation results coming from time exposure images. The results show that the methodology successfully improves the model predictions for short forecasting horizons, and its implementation offers significant advantages in computational expense and robustness over the initial finite difference approach.

Despite the advance state of development of the Delft3D suite, the characterization tests undertaken at the beginning of the research led to the identification of some challenges in the implementation of the data assimilation method. The main problem is related to the restarting procedure; as it generates undesired effects on the model results and therefore lower the accuracy of the finite differences. The problem is linked to the coupling of the wave and flow modules. At the beginning of each model restart, one timestep of the flow model is integrated without wave forcings. For models of swell beaches, the lack of forcings during one timestep generates an undesired wave, which induces significant changes in the morphodynamic evolution. Aside from this bug in the restarting procedure, the choice of the parameter perturbation for finite differences is not straightforward. Most importantly, the relevance of the nonlinear effects triggered by perturbing the parameter set is time dependent. Regarding the wave significant height, the non-linear effects seem to be present in the beginning of the simulation and not so much in the later simulation times. In this regard, an intelligent selection of modes in combination with an appropriate choice of perturbations for their generation, seems to have a significant impact on the cost-effectiveness of the technique. It is difficult to diagnose the most appropriate perturbation magnitude since they are: case, model and initial condition dependent. The sign (direction) of the perturbation has effects on the overall performance of the data assimilation process. This is a difficulty that may be overcome by making extra perturbations in both directions, since this increases significantly the performance of the scheme. Although this implies more computations, the perturbations come at a lower expense than an extra outer loop. On the other hand, smaller perturbations might also solve the problem. By keeping the perturbations within the linear threshold of the model, the effects of the perturbations should be independent of the sign. The number of modes proved to be relevant to minimize the dispersion of the analyzes.

The use of finite differences in the estimation of the reduced order model components offers several advantages and disadvantages. On the one hand, the estimation of finite differences requires a detailed characterization of the model and a properly functioning restarting procedure. A detail characterization of the model is not always available and its development is computationally expensive. A working re-starting procedure on the other hand, is mostly available although its use may trigger undesired errors in the modeling process. On the other hand, finite differences produce an estimate of model the model sensitivities to various elements which provides significant data about the model behavior. Accurate and detailed information about the model sensitivities is useful for a number of other analyses including physical characterization

of processes and observation networks optimization. In short, the finite difference approach is not robust but its results are highly useful. To solve some of the weaknesses observed in the construction of the reduced order model, *Ensemble model order reduction* (EnMOR) is a method for building low rank linear approximations of complex non-linear models that does not use finite difference estimations in the process. The method uses concepts from data assimilation to estimate the components of the reduced order model. In short, in ensemble model order reduction the coefficients of the linear approximation are estimated using a 4DVar method that assimilates model results into the reduced order model. To keep computational costs low, the snapshots required to compute the subspace basis (projection basis) is also used in the estimation process. Just as in *model reduced 4DVar*, EnMOR can be combined with 4DVar (EnMOR-4DVar) for data assimilation purposes.

EnMOR-4DVAR was successfully implemented for a laboratory experiment and for the Egmond aan Zee using the Delft3D modeling suite. Its implementation proved to be more practical than the common finite difference approach. In fact, the computational expense of EnMOR-4DVar is comparable to commonly used ensemble based data assimilation schemes such as ensemble Kalman filter. Also, the scheme shows to be very robust to deal with observation uncertainties. The results show that the combination of linear low rank approximations of complex models and 4D variational methods, can be used effectively in the context of data assimilation. The results presented here show that the technique is able to find sets of parameters that considerably improve the model performance. Furthermore, it is able to reconstruct the observed system's bathymetry by changing the model input parameters suggesting that the EnMOR-4DVar can be successfully used as part of an operational forecasting systems of morphodynamic processes.

Regarding the physical processes, results from the laboratory experiment suggest a complex interaction between the hydrodynamic and the morphodynamic components of the system. The observed results show that the morphodynamic model is limited in its capacity to reconstruct some of the processes observed in the laboratory. Nevertheless, the results obtained from the use of time exposure images show that the assimilation of roller energy dissipation data may be used to recover the system's bathymetry. The low sensitivity at initial simulation times suggests that the morphodynamic system is more sensitive to the initial bathymetry at this point. Nevertheless, a detailed analysis is necessary to evaluate the extent and significance of the model sensitivity to the initial bathymetry. The model is not able to reconstruct the observed troughs and pits appearing under extreme wave conditions. On the other hand, the model is capable of reconstructing the down-state transitions satisfactorily. The results suggest a morphodynamic system that behaves differently in shallow areas and deep areas. Other attempts to optimize morphodynamic model performance (Serafy et al., 2011) have reached the same conclusion. Further research is necessary to assess the causes of this phenomenon. A possible explanation could be the physical scale

differences between deep and shallow morphodynamic processes. Aside from this, the bathymetry evolution seems to be insensible to the parameter set used in chapter 7, at least within the 4 hours morphodynamic simulation time. Further research regarding its dependence to the initial bathymetry is necessary. Aside from that, the estimation shows that an accurate reconstruction of bathymetric states from unknown initial conditions is feasible.

8.1 Insights into future work

In order to assess the real potential of EnMOR - 4DVar, a bigger study case with real observations and a larger number of parameters is advised. An application of the technique that includes in the state vector the initial bathymetry, morphological parameters, hydraulic parameters and numerical parameters could show the full potential of the data assimilation scheme presented here. An important asset of the EnMOR 4DVar is that it provides information about the adjoint of the model. This information is useful for many additional analyzes. [Daescu and Carmichael \(2010\)](#), for example, used this information for observation network optimization. Further analysis is necessary to determine if the information about the adjoint produced with this technique could be used in such applications.

State estimation is probably the best manner for bathymetry estimation. From the results acquired in the experiments implemented here, the only way to work around Delft3D's limitations to generate bar-trough systems is to include bathymetry estimation in the data assimilation process. The implementation of such a data assimilation process with the model reduced 4DVar demands some additional considerations not discussed in this manuscript. The main issue is related to the considerable increase in state size. An efficient and flexible re-parameterization of the bathymetry is necessary for solving the problem. This re-parameterization could be attained by the implementation of a singular value decomposition on a series of possible initial bathymetries.

Further characterization of the reduced order model is necessary to enhance the scheme's potential. An estimation of its expected error with respect to Delft3D by means of Monte Carlo methods is feasible. This information could be valuable to identify weaknesses in the reduced order model and therefore in the assimilation process.

Bibliography

- T. Aagaard, A. Kroon, S. Andersen, R. Sorensen, S. Quartel, and N. Vinther. Intertidal beach change during storm conditions; egmond, the netherlands. *Marine Geology*, 218(1-4):65 – 80, 2005. [cited at p. 90]
- M. Altaf, A. Heemink, and M. Verlaan. Inverse shallow-water flow modeling using model reduction. *International journal for multiscale computational engineering*, 7(6):577–594, 2009. [cited at p. 7]
- M. Altaf, M. Verlaan, and A. Heemink. Efficient identification of uncertain parameters in a large-scale tidal model of the european continental shelf by proper orthogonal decomposition. *International Journal for Numerical Methods in Fluids*, 2010. [cited at p. 79]
- W. Baur and V. Strassen. The complexity of partial derivatives. *Theoretical Computer Science*, 22:317–330, 1983. [cited at p. 15]
- F. Birrien, B. Castelle, V. Mariou, and H. Michallet. Application of a data-model assimilation method to a 3D surf zone sandbar physical experiment. *Journal of Coastal Research*, 64(Special Issue), 2011. [cited at p. 6]
- L. Boltzmann. *Model*, pages 213–220. Dordrecht Reidel Publishing company, 1974. [cited at p. 31]
- R. Brander. Field observations on the morphodynamic evolution of a low-energy rip current system. *Marine Geology*, 157(3):199–217, 1999. [cited at p. 52]
- C. Briere, A. Giardino, and J. Werf. Morphological modeling of bar dynamics with delft3d: The quest for optimal free parameter settings using an automatic calibration technique. *Coastal Engineering Proceedings*, 1(32), 2011. [cited at p. 6, 90]
- R. Bucy. Optimum finite time filters for a special non-stationary class of inputs. Technical report, Johns Hopkins university silver spring MD applied physics lab., 1959. [cited at p. 12]

- G. Burgers, P. van Leeuwen, and G. Evensen. Analysis scheme in the ensemble kalman filter. *Monthly Weather Review*, 126:1719–1724, 1998. [cited at p. 18]
- D. Cacuci. Sensitivity theory for nonlinear systems. i. nonlinear functional analysis approach. *Journal of Mathematical Physics*, 22(12):2794–2802, 1981a. [cited at p. 14]
- D. Cacuci. Sensitivity theory for nonlinear systems. ii. extensions to additional classes of responses. *J-J-MATH-PHYS*, 22(12):2803–2812, 1981b. [cited at p. 14]
- D. Cacuci, C. Weber, E. Oblow, and J. Marable. Sensitivity theory for general systems of nonlinear equations. *Nucl. Sci. Eng.*, 75:88–110, 1980. [cited at p. 14]
- S. Carniel, M. Sclavo, and R. Archetti. Towards validating a last generation, integrated wave-current-sediment numerical model in coastal regions using video measurements. *Oceanological and Hydrobiological Studies*, 40(4):11–20, 2011. [cited at p. 6]
- B. Castelle, H. Michallet, V. Marieu, F. Leckler, B. Dubardier, A. Lambert, C. Berni, P. Bonneton, E. Bartholemy, and F. Bouchette. Laboratory experiment on rip current circulations over a moveable bed: Drifter measurements. *J. Geophys. Res.*, 115, 2010. [cited at p. 8, 67]
- W. Cazemier, R. Verstappen, and A. Veldman. Proper orthogonal decomposition and low-dimensional models for driven cavity flows. *Physics of Fluids*, 10(7), 1998. [cited at p. 38]
- P. Courtier. Experiments in data assimilation using the adjoint model technique. In *Workshop on High-Resolution Analysis*, 1985. [cited at p. 14]
- P. Courtier. Dual formulation of four-dimensional variational assimilation. *Quarterly Journal of the Royal Meteorological Society*, 123(544):2449–2461, 1997. [cited at p. 15]
- P. Courtier, J. Thepaut, and A. Hollingsworth. A strategy for operational implementation of 4D-Var, using an incremental approach. *Quarterly Journal of the Royal Meteorological Society*, 120(519):1367–1387, 1994. [cited at p. 2, 15]
- D. Daescu and G. Carmichael. An adjoint sensitivity method for the adaptive location of the observations in air quality modeling. Technical report, Institute for Mathematics and its Applications - University of Minnesota, 2010. [cited at p. 7, 15, 108]
- M. Davidson, K. Splinter, and I. Turner. A simple equilibrium model for predicting shoreline change. *Coastal Engineering*, 73:191–202, 2013. [cited at p. 6]
- H. de Vriend, M. Capobianco, T. Chesher, H. de Swart, B. Latteux, and M. Stive. Approaches to long-term modelling of coastal morphology: A review. *Coastal Engineering*, 21(1-3):225 – 269, 1993. Special Issue Coastal Morphodynamics: Processes and Modelling. [cited at p. 3]

- Deltares. *Delft3D-FLOW User's Manual*. Deltares, Rotterdamseweg 185 Delft The Netherlands, ver 3.14 edition, July 2009a. [cited at p. 32, 33, 36, 72, 73, 86]
- Deltares. *Delft3D-Wave User's Manual*. Deltares, Rotterdamseweg 185 Delft The Netherlands, ver 3.14 edition, July 2009b. URL <http://delftsoftware.wldelft.nl>. [cited at p. 32]
- A. Eliassen. Provisional report on calculation of spatial covariance and autocorrelation of the pressure field. Technical Report 5, Institute for Weather and Climate Research. Norwegian Academy of Science and Letters, 1954. [cited at p. 12]
- R. Errico. What is an adjoint model? *Bulletin of the American Meteorological Society*, 78(11):2577–2591, 1997. [cited at p. 15]
- G. Evensen. Sequential data assimilation with nonlinear quasi-geostrophic model using monte carlo methods to forecast error statistics. *Journal of Geophysical Research*, 99(05):10,143–10,162, may 1994. [cited at p. 18]
- M. Fisher, M. Leutbecher, and G. A. Kelly. On the equivalence between kalman smoothing and weak-constraint four-dimensional variational data assimilation. *Quarterly Journal of the Royal Meteorological Society*, 131(613):3235–3246, 2005. [cited at p. 15]
- J. Frazier, P. Jimack, and R. Kirby. On the use of adjoint-based sensitivity estimates to control local mesh refinement. *Communications in Computational Physics*, 2009. [cited at p. 15]
- L. Gandin. *Objective Analysis of Meteorological Fields: GIMIZ, Gidrometeorologicheskoe Izdatelstvo, Leningrad 1963 : Transl. from the Russian*. Israel Program for scientific Translations, 1963. [cited at p. 12]
- R. Giering and T. Kaminski. Recipes for adjoint code construction. *ACM Transactions on Mathematical Software (TOMS)*, 24(4):437–474, 1998. [cited at p. 15]
- N. Gordon, D. Salmond, and A. Smith. Novel approach to nonlinear/non-gaussian bayesian state estimation. In *IEE-Proceedings-F*, volume 140, pages 107–113, 1993. [cited at p. 16]
- A. Griewank. On automatic differentiation. In *Mathematical Programming: Recent Developments and Applications*, pages 83–108. Kluwer Academic Publishers, m. iri, k. tanabe edition, 1989. [cited at p. 15]
- R. Holman and J. Stanley. The history and technical capabilities of argus. *Coastal Engineering*, 54(6-7):477–491, 2007. [cited at p. 36]

- R. Holman, N. Plant, and T. Holland. cbathy: A robust algorithm for estimating nearshore bathymetry. *Journal of Geophysical Research: Oceans*, 118(5):2595–2609, 2013. [cited at p. 3, 6]
- P. Houtekamer and H. Mitchell. Data assimilation using an ensemble kalman filter technique. *Monthly Weather Review*, 126(3):796–811, 1998. [cited at p. 18]
- R. Kalman. A new approach to linear filtering and prediction problems. *Journal of basic Engineering*, 82(1):35–45, 1960. [cited at p. 12]
- R. Kalman and R. Bucy. New results in linear filtering and prediction theory. *Transactions of the ASME. Series D, Journal of Basic Engineering*, 83:95–107, 1961. [cited at p. 12]
- A. Kroon. Three dimensional morphological changes of a near bar system along dutch coast near egmond aan zee. *Journal of Coastal Research*, pages 430 – 451, 1991. Special Issue No. 9. [cited at p. 90]
- A. Laub. *Matrix analysis for scientists and engineers*. SIAM, 2005. [cited at p. 27]
- F. Le Dimet. A general formalism of variational analysis. Report 22, CIMMS, Norman, Okla., 1982a. [cited at p. 14]
- F. Le Dimet. Dynamic initialization with filtering of gravity waves. Report 40, CIMMS, Norman, Okla., 1982b. [cited at p. 14]
- F. Le Dimet and O. Talagrand. Variational algorithms for analysis and assimilation of meteorological observations: theoretical aspects. *Tellus A*, 38(2):97–110, 1986. [cited at p. 14]
- G. Lesser, J. Roelvink, J. Van Kester, and G. Stelling. Development and validation of a three-dimensional morphological model. *Coastal Engineering*, 51(8-9):883–915, 2004. [cited at p. 32, 33, 35]
- J. Lewis and J. Derber. The use of adjoint equations to solve a variational adjustment problem with advective constraints. *Tellus A*, 37A(4):309–322, 1985. [cited at p. 14]
- Peter S. Maybeck. Solutions to the kalman filter wordlength problem: Square root and u-d covariance factorizations. Technical report, Air force institute of technology Wright-Patterson, Ohio, 1977. [cited at p. 18]
- B. McElhoe. An assessment of the navigation and course corrections for a manned flyby of mars or venus. *IEEE Transactions on Aerospace and Electronic Systems*, AES-2(4):613 –623, 1966. [cited at p. 13]
- L. McGee, S. Schmidt, and G. Smith. Application of statistical filter theory to the optimal estimation of position and velocity on board a circumlunar vehicle. Technical Report R-135, NASA - Ames Research Center, 1962. [cited at p. 13]

- H Michallet, B Castelle, F Bouchette, A Lambert, C Berni, P Bonneton, and S Damien. Modélisation physique de la morphodynamique d'une plage barre tridimensionnelle. In *Proceedings des XIèmes Journées Nationales Gnier Ctier*, pages 379–386, Les Sables d'Olonne, 2010. Paralia CFL. [cited at p. 8, 38, 67, 69]
- H. Michallet, B. Castelle, Barthlemy E., and P. Berni C., Bonneton. Physical modeling of three-dimensional intermediate beach morphodynamics. *Journal of Geophysical Research*, 2013. [cited at p. 8, 38, 67, 70, 86]
- Hans E. Ngodock, Gregg A. Jacobs, and Mingshi Chen. The representer method, the ensemble kalman filter and the ensemble kalman smoother: A comparison study using a nonlinear reduced gravity ocean model. *Ocean Modelling*, 12(3-4):378–400, 2006. [cited at p. 19]
- J. Pelc, E. Simon, L. Bertino, G. Serafy, and A. Heemink. Application of model reduced 4D-Var to a 1D ecosystem model. *Ocean Modelling*, 2012. [cited at p. 7]
- D. Pham. Stochastic methods for sequential data assimilation in strongly nonlinear systems. *Monthly Weather Review*, 129(5):1194–1207, 2001. [cited at p. 18]
- R. Ranasinghe, G. Symonds, K. Black, and R. Holman. Morphodynamics of intermediate beaches: a video imaging and numerical modelling study. *Coastal Engineering*, 51(7):629–655, 2004. [cited at p. 6, 51, 52, 77, 87]
- D. Roelvink, A. Reniers, A Dongeren, J. Thiel de Vries, R. McCall, and J. Lescinski. Modelling storm impacts on beaches, dunes and barrier islands. *Coastal Engineering*, 56(1112):1133 – 1152, 2009. [cited at p. 3]
- J. Roelvink. Coastal morphodynamic evolution techniques. *Coastal Engineering*, 53(2-3):277–287, 2006. [cited at p. 52]
- J. Roelvink, S. Aarninkhof, K. Wijnberg, and A. Reniers. Quantification of 2D subtidal bathymetry from video. *Rijkswaterstaat, RIKZ, Z*, 3536, 2003. [cited at p. 54]
- J. A. Roelvink and I. Broker. Cross-shore profile models. *Coastal Engineering*, 21(1-3): 163–191, 1993. [cited at p. 70]
- B. G. Ruessink and Y. Kuriyama. Numerical predictability experiments of cross-shore sandbar migration. *Geophysical Research Letters*, 35(1), 2008. [cited at p. 1]
- T. Scott and D. Mason. Data assimilation for a coastal area morphodynamic model: Morecambe bay. *Coastal engineering*, 54(2):91–109, 2007. [cited at p. 6]
- G. Serafy, M. Eleveld, M. Blaas, T. Kessel, S. Gaytan, and H. Woerd. Improving the description of the suspended particulate matter concentrations in the southern north sea through assimilating remotely sensed data. *Ocean Science Journal*, 46(3):179–204, Oct 2011. [cited at p. 79, 88, 107]

- A. Short. Beach systems of the central netherlands coast: Processes, morphology and structural impacts in a storm driven multibar system. *Marine Geology*, 107(1-2): 103–132, 1992. [cited at p. 52, 90]
- A. Short. Beaches of the new south wales coast; a guide to their nature, characteristics, surf and safety. Technical report, Australian Beach Safety and Management Program, Sydney, 1993. [cited at p. 52]
- M. Smit, A. Reniers, B. Ruessink, and D. Roelvink. The morphological response of a nearshore double sandbar system to constant wave forcing. *Coastal Engineering*, 55(10):761–770, 2008. [cited at p. 37, 52, 53, 54]
- M. W. J. Smit, S. G. J. Aarninkhof, K. M. Wijnberg, M. Gonzalez, K. S. Kingston, H. N. Southgate, B. G. Ruessink, R. A. Holman, E. Siegle, M. Davidson, et al. The role of video imagery in predicting daily to monthly coastal evolution. *Coastal engineering*, 54(6-7):539–553, 2007. [cited at p. 37]
- P. Smith, G. Thornhill, S. Dance, A. Lawless, D. Mason, and N. Nichols. Data assimilation for state and parameter estimation: application to morphodynamic modelling. *Quarterly Journal of the Royal Meteorological Society*, 2012. [cited at p. 6]
- G Thornhill, D. Mason, S. Dance, A. Lawless, N. Nichols, and H. Forbes. Integration of a 3D variational data assimilation scheme with a coastal area morphodynamic model of morecambe bay. *Coastal Engineering*, 69:82–96, 2012. [cited at p. 6]
- I. Turner, S. Aarninkhof, and R. Holman. Coastal imaging applications and research in australia. *Journal of Coastal Research*, 221:37–48, 2006. ISSN 0749-0208. doi: 10.2112/05A-0004.1. URL <http://www.bioone.org/doi/abs/10.2112/05A-0004.1>. [cited at p. 52]
- L. Uunk. *Automated collection of intertidal beach bathymetries from Argus video images*. Msc thesis, University of Twente, Twente, 2008. [cited at p. 54]
- L. Uunk, K. Wijnberg, and R. Morelissen. Automated mapping of the intertidal beach bathymetry from videos images. *Coastal Engineering*, 57:461–469, 2010. [cited at p. 3, 90]
- A. van Dongeren, N. Plant, A. Cohen, D. Roelvink, D. Haller, and P. Catalan. Beach wizard: Nearshore bathymetry estimation through assimilation of model computations and remote observations. *Coastal Engineering*, 55(12):1016–1027, 2008. ISSN 0378-3839. [cited at p. 2, 3, 6, 89, 90]
- A. van Dongeren, M. van Ormondt, L. Sembiring, R. Sasso, M. Austin, C. Briere, C. Swinkels, D. Roelvink, and van Thiel de Vries J. Rip current predictions through model-data assimilation on two distinct beaches. *Coastal Dynamics*, 2013. [cited at p. 91]

- M. van Ledden. *Sand-mud segregation in estuaries and tidal basins*. PhD thesis, Technische Universiteit Delft, 2003. [cited at p. 31]
- L. van Rijn. *Principles of sediment transport in rivers estuaries and coasts seas*. Aqua Publications, 1006 AN Amsterdam, The Netherlands, 1993. [cited at p. 35]
- L. van Rijn. Unified view of sediment transport by currents and waves. i: Initiation of motion, bed roughness, and bed-load transport. *Journal of hydraulic engineering*, 133(6):649–667, 2007a. [cited at p. 2, 31]
- L. van Rijn. Unified view of sediment transport by currents and waves. II: suspended transport. *Journal of hydraulic engineering*, 133(7):668–689, 2007b. [cited at p. 2, 31, 35]
- L. van Rijn. Unified view of sediment transport by currents and waves. III: graded beds. *Journal of hydraulic engineering*, 133(7):761–775, 2007c. [cited at p. 2, 31]
- L. van Rijn, D. Walstra, and M. van Ormondt. Unified view of sediment transport by currents and waves. iv: Application of morphodynamic model. *Journal of hydraulic engineering*, 133(7):776–793, 2007. [cited at p. 31]
- P. Vermeulen and A. Heemink. Model-reduced variational data assimilation. *Monthly weather review*, 134(10):2888–2899, 2006. [cited at p. 2, 4, 7, 38, 41, 52, 55, 57, 102]
- R. Vos, P. ten Brummelhuis, and H. Gerritsen. Integrated data-modelling approach for suspended sediment transport on a regional scale. *Coastal Engineering*, 41:177–200, 2000. [cited at p. 4]
- B. Waeles, P. Hir, P. Lesueur, and N. Delsinne. Modelling sand/mud transport and morphodynamics in the seine river mouth (France): an attempt using a process-based approach. *Hydrobiologia*, 588(1):69–82, September 2007. ISSN 0018-8158, 1573-5117. doi: 10.1007/s10750-007-0653-2. URL <http://www.springerlink.com/index/10.1007/s10750-007-0653-2>. [cited at p. 31]
- D.J.R. Walstra, A.J.H.M. Reniers, R. Ranasinghe, J.A. Roelvink, and B.G. Ruessink. On bar growth and decay during interannual net offshore migration. *Coastal Engineering*, 60(0):190 – 200, 2012. [cited at p. 1]
- Jeffrey S. Whitaker and Thomas M. Hamill. Ensemble data assimilation without perturbed observations. *Monthly Weather Review*, 130(7):1913–1924, 2002. [cited at p. 18]
- E. Wigner. Effect of small perturbations on pile period. In *Manhattan Project Report, CP-G3048*, 1945. [cited at p. 14]

- K. Wijnberg, J. Roelvink, and S. Aarninkhof. Bed variability in the surf zone at the storm- and seasonal time scale, mapped by argus-video techniques, 2004. [cited at p. 90]
- G. W. Wilson, H. T. Azkan-Haller, and R. A. Holman. Data assimilation and bathymetric inversion in a two-dimensional horizontal surf zone model. *Journal of Geophysical Research: Oceans*, 115(C12), 2010. [cited at p. 6]
- L. Wright and A. Short. Morphodynamic variability of surf zones and beaches: A synthesis. *Marine geology*, 56:93–118, 1984. [cited at p. 51, 52, 68]
- C. Wu, J. Chen, P. Lin, and K. Chou. Targeted observations of tropical cyclone movement based on the adjoint-derived sensitivity steering vector. *Journal of the Atmospheric Sciences*, 64(7):2611, 2007. [cited at p. 15]
- C. Wunsch. Ocean observations and the climate forecast problem. In *Meteorology at the Millenium*, pages 233 – 245. Massachusetts Institute of Technology, Cambridge MA, USA., Academic Press, 2002. URL <http://ocean.mit.edu/~cwunsch/papersonline/rmsbookpaper.pdf>. [cited at p. 11]